# UNIVERSIDAD AUTÓNOMA DE NUEVO LEÓN
# FACULTY OF CHEMICAL SCIENCES

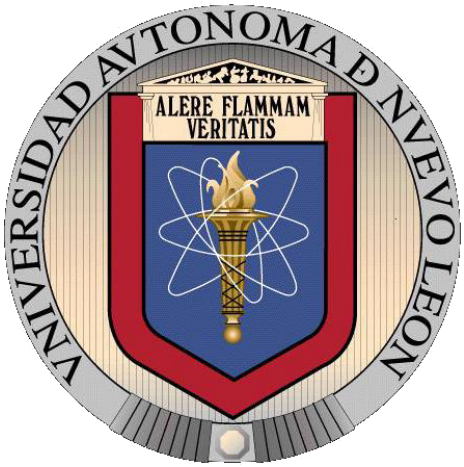


## MODELING OF THE PHOTOCATALYTIC REACTOR FOR BLUE WASTEWATER DEGRADATION BY A COMPOSITE BASED ON ZINC OXIDE, GREEN PIGMENTS, AND PHENOLIC RESINS

**BY**

**DANIEL SIMÓN OLIVO ALANÍS**

**AS A PARTIAL REQUIREMENT TO OBTAIN THE DEGREE OF DOCTOR OF SCIENCE WITH ORIENTATION IN SUSTAINABLE PROCESSES**

**MAY, 2019**

**UNIVERSIDAD AUTÓNOMA DE NUEVO LEÓN**
**HIGHER SCHOOL OF CHEMICAL SCIENCES**

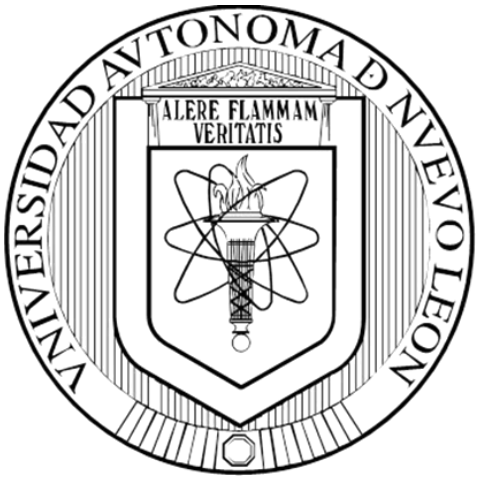


# MODELING OF THE PHOTOCATALYTIC REACTOR FOR BLUE WASTEWATER DEGRADATION BY A COMPOSITE BASED ON ZINC OXIDE, GREEN PIGMENTS, AND PHENOLIC RESINS

**BY**

**DANIEL SIMÓN OLIVO ALANÍS**

**AS A PARTIAL REQUIREMENT TO OBTAIN THE DEGREE OF DOCTOR OF SCIENCE WITH ORIENTATION IN SUSTAINABLE PROCESSES**

**MAY, 2019**

# UNIVERSIDAD AUTÓNOMA DE NUEVO LEÓN

# FACULTY OF CHEMICAL SCIENCES

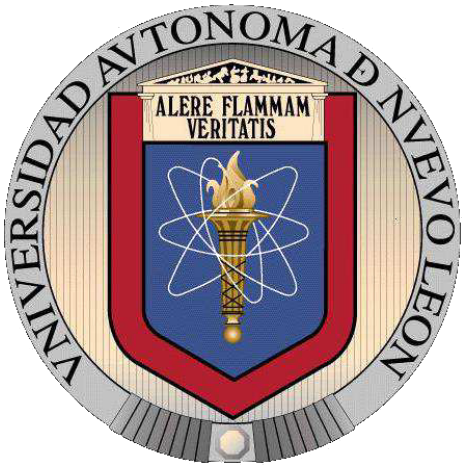


## MODELING OF THE PHOTOCATALYTIC REACTOR FOR BLUE WASTEWATER DEGRADATION BY A COMPOSITE BASED ON ZINC OXIDE, GREEN PIGMENTS, AND PHENOLIC RESINS

**BY**

**DANIEL SIMÓN OLIVO ALANÍS**

**AS A PARTIAL REQUIREMENT TO OBTAIN THE DEGREE OF DOCTOR OF SCIENCE WITH ORIENTATION IN SUSTAINABLE PROCESSES**

| | |
|---|---|
| **M.Sc. Daniel Simón Olivo Alanís** | **Dr. Refugio Bernardo García Reyes** |

**May 9th, 2019 Division of Graduate Studies, Monterrey, Nuevo León, México**

Modeling of the photocatalytic reactor for blue wastewater degradation by a composite based on zinc oxide, green pigments, and phenolic resins

Dissertation Review committee:

---

Dr. Refugio Bernardo García Reyes

Advisor

---

Dr. Aracely Hernández Ramírez

Reviewer

---

Dr. Eduardo Soto Regalado

Reviewer

---

Dr. Gerardo Flores Escamilla

Reviewer

## Acknowledgments

Daniel Simón Olivo Alanís would like to thank to the Consejo Nacional de Ciencia y Tecnología (CONACYT) for the scholarship (429428) received during his doctoral studies. All authors also thank to the Facultad de Ciencias Químicas of the Universidad Autónoma de Nuevo León for funding the approved research project (02-100309-PST-16/136). The vast majority of the experimental section was conducted in the Laboratorio de tratamiento de aguas II, the characterization of the synthesized materials was carried out on the Laboratorio de materiales II, Laboratorio de instrumentación analítica and Laboratorio para la sustentabilidad de los procesos del petróleo. All these facilities belong to the Facultad de Ciencias Químicas of the Universidad Autónoma de Nuevo León.

**TABLE OF CONTENTS**

# LIST OF TABLES

# LIST OF FIGURES

**Figure 16**. The absorption coefficient of phenolic resin and sensitized phenolic resin structures.

**Figure 17.** Current-potential measurement for phenolic resin and chlorophyll-sensitized phenolic resin.

**Figure 18**. Energy gap determination for phenolic resin and chlorophyll-sensitized phenolic resin. Inset shows the photon energy region of the observed peak.

**Figure 19.** Point of zero charges of the studied semiconductors: phenolic resin (R), ZnO-incorporated phenolic resin (R-ZnO), chlorophyll-sensitized phenolic resin (R-C) and zinc oxide (ZnO).

**Figure 20.** Adsorption isotherms of methylene blue onto ZnO and phenolic resins on (A) acidified tap water, (B) deionized water, (C) tap water and (D) alkaline water.

**Figure 21.** Pseudo-first orders kinetic constant of methylene blue decolorization under different water matrices with (A) 5 mg/L, (B) 10 mg/L and (C) 15 mg/L of initial concentration. (D) speciation diagram of carbonate, bicarbonate and carbonic acid species.

**Figure 22.** a) Chemical oxygen demand and b) Total organic carbon removal of methylene blue under different water matrices, with polymeric photocatalysts based on phenolic resins, ZnO photocatalyst and photolysis control.

**Figure 23.** Effective photocatalytic mechanism of phenolic resin structures under different water matrices. A) phenolic resin, B) ZnO-incorporated phenolic resin and C) chlorophyll-sensitized phenolic resin.

**Figure 24.** LVRPA distribution in a tubular reactor for ZnO and the phenolic resin structures with asymmetry factor, $g = 0$ and catalyst load, $C_{cat}$ = 1 g/L.

**Figure 25.** Effect of the catalyst loading on the overall volumetric rate of photon absorption ($E_{\lambda}^{a}$) for ZnO and the phenolic resin structures.

**Figure 26.** LED lamp emission spectral power distribution vs photon energy (colors were arbitrarily chosen to point out the four segments).

**Figure 27.** Quantum yield estimation for chlorophyll-sensitized phenolic resin on visible-LED irradiation as a function of the catalyst load.

**Figure 28.** The rate of electron-hole pair generation for chlorophyll-sensitized phenolic resin on a tubular reactor under visible-LED irradiation, as a function of the catalyst load.

**Figure 29.** Experimental data of the kinetic decolorization of methylene blue in deionized water over time (red filled triangles), and the kinetic model prediction of electron attack (black line) with A) phenolic resin and B) ZnO-incorporated phenolic resin.

**Figure 30.** Kinetic degradation of methylene blue over time at pH 5.8 (black filled triangles), pH 6.5 (black filled circles) and pH 7.2 (black filled diamonds), as well as the kinetic model adjustment of carbonate anion radical attack at pH 5.8 (black line) and kinetic prediction at pH 6.5 and 5.8 (red and blue line, respectively) with phenolic resin as a semiconductor.

**Figure 31.** Decolorization kinetics of blue wastewater following the methylene blue concentration in tap water conditions with chlorophyll-sensitized phenolic resin dosages of 1 g/L (green filled triangles), 2 g/L (orange filled circles) and 3 g/L (black filled diamonds).

**Figure 32.** Decolorization kinetics of blue wastewater following the methylene blue concentration in acidified tap water conditions with chlorophyll-sensitized phenolic resin dosages of 1 g/L (green filled triangles), 2 g/L (orange filled circles) and 3 g/L (black filled diamonds). Continuous lines represent the kinetic model prediction for superoxide anion radical attack for photocatalyst dosages of 1 g/L (black line), 2 g/L (blue line) and 3 g/L (red line).

**Figure 33.** Decolorization kinetics of synthetic blue wastewater following the methylene blue concentration in acidified tap water conditions with chlorophyll-sensitized phenolic resin dosages of 1 g/L (orange filled circles) on a visible-LED irradiated tubular reactor with one pump array. Continuous lines represent the kinetic model prediction for superoxide anion radical attack for photocatalyst dosages of 1 g/L (black line), 2 g/L (blue line) and 3 g/L (red line).

**Figure 34.** Decolorization kinetics of synthetic blue wastewater following the methylene blue concentration in acidified tap water conditions with chlorophyll-sensitized phenolic resin dosages of 1 g/L (orange filled circles) with one pump

array and 3 g/L (blue filled triangles) with two pumps in series array on a visible-LED irradiated tubular reactor. Continuous lines represent the kinetic model prediction for superoxide anion radical attack for photocatalyst dosages of 3 g/L (black line), 2 g/L (blue line) and 1 g/L (red line).

**Figure 35.** Photocatalytic treatment of synthetic blue wastewater with 3 g/L of chlorophyll-sensitized phenolic resin as a semiconductor on a visible-LED irradiated tubular reactor. Decolorization of methylene blue (black filled diamonds) and TOC removal (red filled triangles).

# NOMENCLATURE

| | |
|---|---|
| $PD_{index}$ | Polydispersity index |
| $M_w$ | Molecular weight |
| EPM | Effective photocatalytic mechanism |
| $h_v$ | Irradiated photon energy |
| LED | Light-emitting diodes |
| PVA | Poly-vinyl alcohol |
| HMTA | Hexamethyl-n-tetraamine |
| GPC | Gel permeation chromatography |
| CVA | Cyclic voltammetry |
| HPLC | High-performance liquid chromatography |
| DRUV-vis | Diffuse reflectance ultraviolet-visible |
| NHE | Normal hydrogen electrode |
| R | Phenolic resins at a defined molar ratio |
| DW | Deionized water |
| TW | Tap water |
| ATW | Acidify tap water |
| MB | Methylene blue |
| MO | Methyl orange |
| AQS | Anthraquinone-2-sulfonate |
| R-ZnO | ZnO-incorporated phenolic resin |
| R-C | Chlorophyll-sensitized phenolic resin |
| EAC | Electron acceptor compound |
| EDC | Electron donor compound |
| LED | Light emitting diodes |
| ROS | Reactive oxygen species |
| LVRPA | Local volumetric rate of photon absorption |
| OVRPA | Overall volumetric rate of photon absorption |
| CB | Conduction band |
| VB | Valence band |

*Special symbols*

| | |
|---|---|
| $h_r^+$ | Reactive surface hole |
| $e_r^-$ | Reactive surface electron |
| $h_s^+$ | Surface hole |
| $e_s^-$ | Surface electron |
| $h_f^+$ | Free hole |
| $e_f^-$ | Free electron |
| $D$ | Electron donor specie |
| $D^+$ | Oxidized electron donor specie |
| $A$ | Electron acceptor specie |
| $A^-$ | Reduced electron acceptor specie |
| $E_{Ag/AgCl}$ | Reduction or oxidation potential referenced to $Ag/AgCl$ electrode |
| $E^{\circ}_{Ag/AgCl}$ | Standard reduction potential referenced to $Ag/AgCl$ electrode |
| $E_{RHE}$ | Reduction or oxidation potential referenced to the reversible hydrogen electrode |
| $\mathrm{k}_{app}$ | Pseudo first order apparent rate constant in $h^{-1}$ |
| $C_{i,0}$ | Initial concentration of methylene blue in mg/L |
| $C_i$ | Concentration of methylene blue at time t in mg/L |
| $t$ | Illumination time |
| $\chi^-$ | Ionic species ($HCO_3^-$, $SO_4^{2-}$, etc) |
| $\chi\bullet$ | Radical ionic species ($CO_3^{-\cdot}$, $SO_4^{-\cdot}$, $NO_3^{\cdot}$, etc) |
| $k_{i,app,atm}^{scavenger}$ | Pseudo first order apparent reaction rate constant for the control experiment with scavenger on aerobic or anaerobic conditions |
| $k_{app,atm}^{control}$ | Pseudo first order apparent reaction rate constant for the control experiment without scavenger on aerobic or anaerobic conditions |
| $\varphi_i$ | Effective fraction contribution of $i^{th}$ mechanism |
| $\mathcal{M}_{eff}$ | Photocatalytic mechanism effectiveness |
| $\omega$ | Scattering albedo |
| $\sigma$ | Scattering coefficient |
| $\kappa$ | Absorption coefficient |
| $\beta$ | Extinction coefficient |

| | |
|---|---|
| $a$ , $b$ , $\gamma$ | Six flux model parameters |
| $p_f$ | Probability of forward scattering |
| $p_b$ | Probability of backward scattering |
| $p_s$ | Probability of sideward scattering |
| $\omega_{corr}$ | Corrected scattering albedo value |
| $\lambda_{\omega_{corr}}$ | Corrected reactor path length value |
| $\tau$ | Optical thickness |
| $\tau_{app}$ | Corrected optical thickness |
| $P_{\varphi}^{a}$ | Probability of absorption of light |
| $\phi_g^{id}$ | Ideal quantum yield |
| $\phi_{g,\max}^{Eff}$ | Maximum effective quantum yield |
| $\psi_E$ | Energy function |
| $\hat{E}^{a}_{g(\lambda-\lambda')}$ | Overall volumetric rate of photon absorption along the studied wavelength |
| $\hat{E}^{a}_{g(\lambda-\lambda'),0}$ | Overall volumetric rate of photon absorption along the studied wavelength at the outer reactor volume |
| $\theta_i$ | Langmuir-Hinshelwood adsorption parameter |
| $\kappa_P$ | Surface properties of the catalyst |
| $S_g$ | Specific surface area |
| $C_{Cat}$ | Catalyst load |
| $\alpha_{h^+-e^-}$ | Kinetic constant of the electron-hole attack mechanism model |
| $k_i$ | Kinetic constant of the reactive oxygen species mechanisms model |
| $\mathrm{K}_{IT}(T)$ | Equilibrium constant of interfacial charge transfer |
| $R_g$ | The rate of electron-hole pair generation |

# ABSTRACT

Daniel Simón Olivo Alanís
Universidad Autónoma de Nuevo León
Facultad de Ciencias Químicas

Dissertation title: Modeling of the photocatalytic reactor for blue wastewater degradation by a composite based on zinc oxide, green pigments, and phenolic resins

Number of pages: 132 Candidate for the Doctoral degree of Sciences with orientation on Sustainable Processes
Study area: Sustainable Processes

**Purpose and method of the study:** In this research, an extension of the kinetic and quantum yield model, as well as the evaluation of the radiation absorption phenomena on a visible-LED reactor for the photocatalytic blue wastewater degradation employing a novel polymeric material as a photocatalyst was proposed. Three novel materials based on phenolic resins were developed, and further characterized by electronic and optical techniques. The polymeric semiconductors were evaluated for the photocatalytic degradation of methylene blue, as well as for the synthetic blue wastewater treatment. The proposed kinetic model, for further reactor design, takes into account the generation of electron-hole pair and the reactive oxygen species via redox reactions, as well as the attack of the reactive species to the pollutant. Also, the mechanistic contribution of the different operational conditions was studied with the novel proposed effective photocatalytic mechanism model. The proposed models were validated under several operation conditions to evaluate its robustness.

**Contribution and Conclusions:** Findings exhibited that the phenolic resin structures show a well performance in the presence of the alkalinity. In addition, the modified phenolic resin shows a selective attack via carbonate and superoxide anion radical species at different operational conditions. Moreover, the evaluation of distribution of light revealed that chlorophyll-sensitized phenolic resin reaches the highest rate of photon absorption, as well as presents the highest photocatalytic activity. Furthermore, the quantum yield calculation allows the determination of the rate of electron-hole pair of any type of semiconductor and source of irradiation. The rate of activation, as well as the physical interaction of the semiconductor with the reactive media, allows to evaluate the proposed generalized kinetic model under several operational conditions, validating its robustness for photocatalytic reaction engineering. The chlorophyll-sensitized phenolic resins showed the highest photocatalytic activity for the degradation of methylene blue, as well as for the synthetic blue wastewater treatment. Finally, the generalized kinetic model arises as the key for the design of light-assisted reactors, but further implementation of other geometries and sources of irradiation needs to be studied in order to trustworthy the application of photocatalytic degradation process at scaled up systems.

# 1 Introduction

Because of the chemical and petrochemical industrial development, several new xenobiotic molecules are discharged deteriorating the quality of the water streams. Wastewater from the above-mentioned industries carries a high load of organic and inorganic pollutants. For instance, the chemical industry discharge pollutants at high concentrations and wide diversity such as aromatics, aliphatic, aldehydes, cyanides, glycols, sulphides, and organic acids, among others [1]. For this reason, the selection of the best wastewater treatment process for pollutants removal of industrial effluents has become a difficult task due to its complex nature.

It is well known that conventional biological treatment efficiency (*e.g.* activated sludge or anaerobic digestion) tends to decay under the presence of some xenobiotic pollutants [2]. Consequently, its application becomes unavailable for complex wastewater treatment. Nonetheless, further research for innovation and application of water treatment process has been growing up in the last years. Recently, a highly complex wastewater composed primarily of ammonia, aromatics, and salts, was treated on *airlift* aerobic reactor, achieving simultaneous nitration and degradation of aromatics [3]. Nevertheless, the acclimation period must be carried out during months. Furthermore, anaerobic process research has implemented redox mediators to decrease inhibition and accelerate electron transport with satisfactory results [4,5]. This technology was employed for colour removal of textile effluents, however wastewater decolorization produced aromatic amines, that cannot be consumed by anaerobic bacteria [6]. For these reasons, other treatments (before or after) must be applied to increase the rate of degradation and to achieve complete oxidation of complex wastewater pollutants.

Advanced oxidation processes (AOP) have been gaining territory on wastewater treatment because of its high capability for the decomposition of xenobiotic pollutants. These processes are based on the production and utilization of reactive oxygen species (ROS) that quickly and selectively, oxidize or reduce a broad variety of organic compounds [7]. Among the AOPs, heterogeneous photocatalysis has been attracting more attention because its potential to solve the increasing

energy shortage (hydrogen production) and environmental pollution problems (wastewater treatment) [8]. It has been proved well functionality in organic systems under 1500 mg/L of total organic carbon (TOC) concentration, for degradation of specific pollutants like drugs, pesticides, cyanides, dyes, phenolic compounds, etc [9–12]. Even more, photocatalytic hydrogen production has been studied employing high TOC concentration of alcohols, low-chain carbon acids, tertiary amines, and carbohydrates, demonstrating the high capacity for energy generation [13–17]. In general terms, four fundamental aspects must be considered for the application of this technology; (i) reactive system, (ii) semiconductor photocatalyst, (iii) the irradiation sources and (iv) the reactor geometry. In the following section, all these important features are discussed more in detail.

# 2. Background

## *2.1. Theoretical framework*

### 2.1.1. Reactive System

Some characteristics of the reactive system can enhance or inhibit the photocatalytic processes. Those characteristics are closely related to the photon transport from the source of irradiation to the active site of the semiconductor. To understand this phenomenon, we need to relate some characteristics of light. First, Planck's equation can define the photon energy as follows:

$$E = h\upsilon = \frac{hc}{\lambda} \ldots(1)$$

where $c$ is the speed of light (approximately 299,792,458 m/s), $\lambda$ is the wavelength and $h$ is the Planck's constant (approximately 6.62607004 × $10^{-34}$ $m^2$ kg/s). Since the speed of light and Planck's constant remains unchanged, photon energy inversely depends on the wavelength. In other words, the lower energy of the incident photons is obtained at a higher wavelength on the electromagnetic spectrum. In contrast, UV irradiation (*i.e.* high energy of photons) can easily activate the semiconductor materials with high activity for ROS generation, contrary to the activation under visible irradiation.

Likewise, there are some optical characteristics of the reactive media that have great influence of the photon transport. For instance, the turbidity can act as an interference to the photon transport produced by dissolved and suspended solids causing the called "*shielding effect*". Moreover, the catalyst particles may have high optical density, that will increase the turbidity of water (depending on the catalyst dosage) generating a photon hindrance. It is well known that the photocatalytic activity decreases considerably at high $TiO_2$ dosages ($C_{cat} > 1\ g/L$), and it is mainly caused by poor photon transport on the reactive media [18]. Equally, polychromic characteristics of the wastewater could be due to a different variety of dyes. However, many dyes have been also explored as sensitization agents for semiconductor materials on solar cells and heterogeneous photocatalysis,

observing in some cases, autocatalytic behaviour [19]. This can be reasonably explained due to absorption characteristics of the dye, that could act as an electron injector into the conduction band or to produce reactive transient as a conventional semiconductor. Consequently, dye-containing wastewater could represent a challenge for photocatalytic process due to its intrinsic optical characteristics. Nonetheless, in some cases, integration processes can be achieved exploiting the sensitization characteristics of dyes within the photocatalytic characteristics of the semiconductor, to enhance the remediation of wastewater [20].

Despites the amount of turbidity and color intensity, once the light is near the catalyst particle, the photons need to surpass the interfacial energy through the liquid solution and the active site of the semiconductor. This energetic resistance depends on the physical-chemical nature of the catalyst and the pollutant [21]. Similar to the mass transfer process, the photons are governed by the same transport laws. Both the pH of water systems as well as the surface charge of the catalyst allow the electrostatic interaction between the semiconductor with the pollutant [22]. This means that for acid type catalyst, pH of the solution must be lower than the pH of zero-point charge of the material to minimize the energy density for the pass of light. Once the photons reach the active site of the semiconductor, the activation mechanism takes place, generating an electron-hole pair and a successive interfacial electron transfer reaction is carried out.

### 2.1.2. Semiconductor

When the semiconductor is irradiated by an input light possessing a higher energy gap ($hv > E_g$), a valence band electron is excited to the conduction band, leaving behind a photo-generated hole at the valence band [23]. In semiconductor suspensions, surfaces reactive holes and electrons ($h_r^+$ & $e_r^-$) can oxidize ($D \rightarrow D^+$) and reduce ($A \rightarrow A^-$) any species depending on its surface state energies (*i.e.* redox potentials of suspensions) [24]; then, ROS could be generated through water oxidation or oxygen reduction for hydroxyl and superoxide radical production, respectively (Figure 1). Consequently, surface states and reactive oxygen species could transform or degrade organic pollutants [25].

Titanium dioxide ($TiO_2$) is the most widely studied photocatalyst due to its abundance, nontoxicity, high stability, and unique photocatalytic efficiency. Likewise, the main mechanism for degradation pathway is given by hydroxyl radical attack and, in some cases, superoxide radical attack [26,27]. Nevertheless, activation wavelength and wide band gap energy, that cause fast recombination of photogenerated charge, are the main reasons of unavailability for its application to real wastewater systems. Additionally, bicarbonate alkalinity plays a major role in water treatment processes since it negatively affects the photocatalysis process with $TiO_2$, leading to its deactivation, attributable to the scavenging of reactive oxygen species and the aggregation behaviour that reduces the available catalyst surface, which involves the unavailability for its application on real wastewater treatment [28–30]. Therefore, a variety of modification routes as doping, coupling, heterostructure, and dye sensitization, as well as the proposal of novel materials as graphene oxide, bismuth oxyhalides and polymeric semiconductors have been taking attraction due to the increase of the visible light response of photocatalysts [31–34].

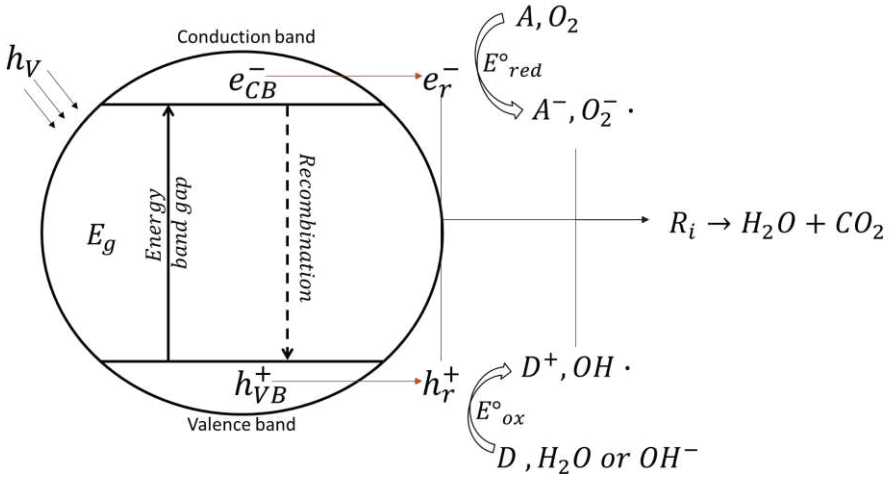


**Figure 1.** Photocatalytic reaction mechanisms to generate electron-hole pair and reactive oxygen species.

Since the development of graphitic carbon nitride for highly efficient hydrogen production under visible irradiation [35], the polymeric semiconductors have been investigated for both energy generation and water remediation, resulting on highly active materials [34,36–38]. Also, it has been demonstrated that the activation of

polymeric semiconductors differs from conventional metallic semiconductors (*i.e.* $TiO_2$). The energetic states of amorphous carbon depend on $sp^2$ and $sp^3$ hybridization, polymerization degree, and π state order. At higher $sp^2$ clusters, π states increases, conducting to a stronger photon absorption in the visible light region, carrying basal π states to excited π state $(\pi - \pi*)$, leading to the generation mechanism of reactive species as a conventional semiconductor [35–37,39]. In addition, due to the organic nature of polymeric semiconductors, modification or coupling to other semiconductors seems highly suitable to manage the absorption characteristics of photocatalyst and fits with the electromagnetic radiation field of different irradiation sources. Therefore, photons will be effectively transmitted and semiconductor's full potential will be reached [40].

### 2.1.3. The irradiation sources

Irradiation sources can be divided into two general groups: natural and artificial light sources. The usage of cheaply available natural daylight (solar irradiation) is advantageous when the high cost of artificial light sources (lamps and electricity) have to be avoided; however, highly efficient solar photocatalysis systems requires complex design and components [41]. Sunlight as a natural source of UV irradiation is cost-effective, but it is also insufficient and not available in all geographic locations.

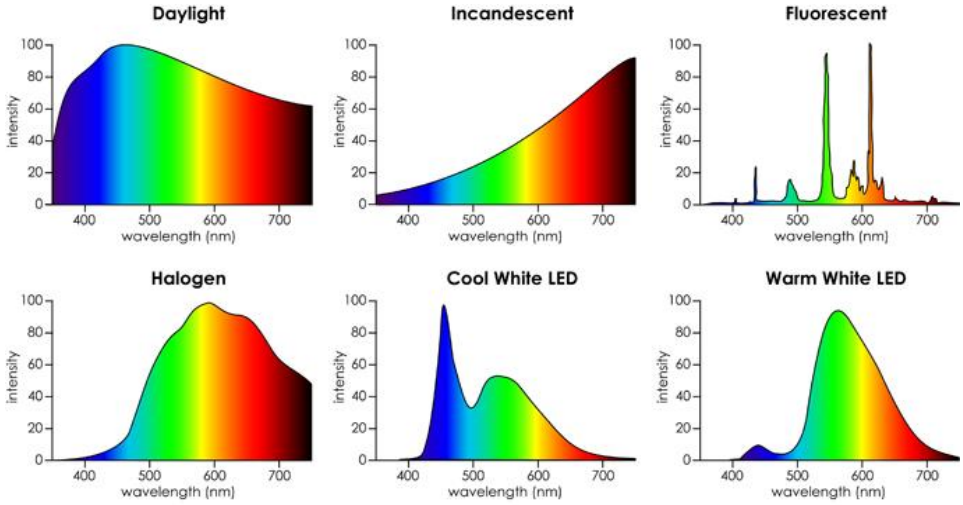


**Figure 2**. Wavelength screening for different irradiation sources.

Alternatively, if artificial light sources are chosen over natural solar light, a number of artificial light devices can be employed, for example, Xe arc, halide, lasers, fluorescent or light emitting diodes (LED) lamps [42]. As observed in Figure 2, several irradiation sources can be employed for the activation of the visible-active photocatalyst, being the halogen and the LED lamps the best options to be selected considering the electromagnetic radiation emission intensity, due to the simulation of natural daylight with the advantageous higher irradiance. Moreover, UV lamps and solar irradiation have been widely employed as a model source of irradiation for heterogeneous photocatalysis with $TiO_2$ [41,43]. However, for visible-active novel materials, some researchers have recently focused in seeking an efficient light source, being the visible-LED lamps the most promising irradiation source for photocatalytic process due to their properties such as high quantum efficiency, low cost and long lifetime [42].

Finally, the photocatalytic reactor design and scaled up operation emerge as the most challenging issues for the application of advanced oxidation processes for industrial wastewater treatment, but the fundamental aspects such as the reactive system, semiconductor, and irradiation source must be coupled to achieve an adequate design of the reactor.

### 2.1.4. Reactor geometry

The simulation and full predictive design of large-scale photocatalytic reactors can be carried out by solving the conservation equations of momentum, energy, and mass on the system, similarly to conventional chemical reactors. The momentum and mass balance equations take the same expressions as those corresponding to thermal reactors, since they depend on the fluid dynamic behaviour of the reactor (well-mixed, plug-flow, axial dispersion, *etc.*), the relevant mass transfer mechanism (diffusion and/or convection) and the expression corresponding to the reaction rate taking into consideration the stoichiometry of the chemical reactions [44]. The main feature that distinguishes a photoreactor from a chemical reactor is the presence of photons. Photons can be considered as a chemical reagent whose

function is that of exciting molecules in the homogeneous systems and of generating electron-hole pairs on the heterogeneous systems. Consequently, it is of fundamental importance to develop a photocatalytic reactor model that considers the fate of the photons in the reactor. The development of a complete photocatalytic reactor model at different scales includes the four main components: (i) the reactive system, (ii) the irradiation source, (iii) the semiconductor photocatalyst, and (iv) the reactor type and geometry. These elements should be clearly defined to describe correctly the modeling equations and the phenomenological processes of a photocatalytic process.

There are various radiative balances, however, for the election of an accurate phenomenological equation, reactor geometry must be established from the beginning. Related to the concentration profiles, reactor type can be divided into two general groups: immobilized catalyst reactor and slurry reactor. For a better comprehension of the geometry, a brief explanation of each type of reactor is discussed in the following section.

a. Immobilized photocatalyst reactor

Photocatalytic reactors with supported/immobilized catalyst have been studied for both liquid and gas phases, mainly for the oxidation of pollutants in air and water. The performance of the photocatalytic process in a packed-bed catalytic reactor configuration allows the continued use of the photocatalytic process by eliminating the post-treatment step in the wastewater decontamination; besides, a high-volume wastewater treatment could be implemented operating in a continuous-flow mode. Several types of photoreactors are described in the bibliography, among them, packed-bed and fluidized-bed reactors [45]. The flat-plate and the annular reactor are the most studied geometries, but the coupling of the solar-CPC reactor has been recently conducted [46]. Figure 3 shows the geometrical characteristics of the above-mentioned photocatalytic reactors.

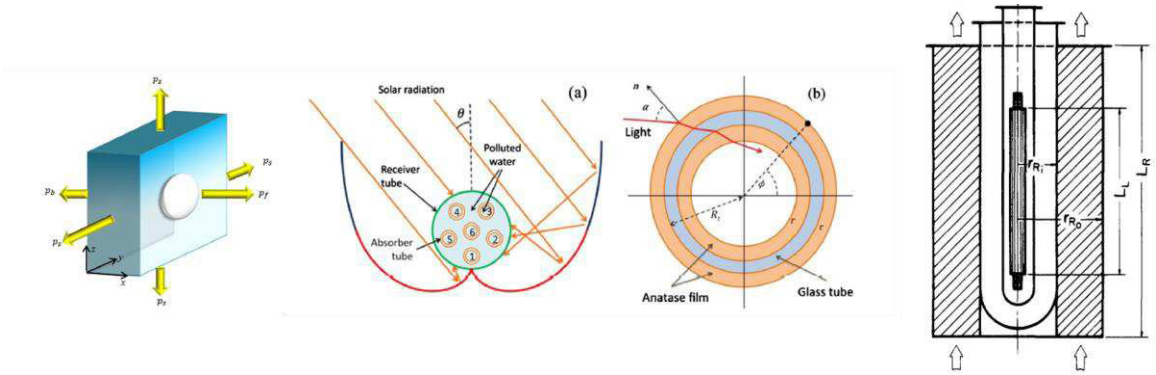


**Figure 3**. Different configuration of the photocatalytic reactor with supported catalyst.

It is important to notice that three-step transport phenomena of photons are carried out in the photocatalytic process with supported catalyst: absorption, transmission, and reflection of light. Likewise, two main approaches have been employed for the modeling of the radiative absorption of light on photocatalytic reactors. Monte Carlo ray tracing is a well-known numerical method for the solution of radiation problems and has been used before to describe radiation absorption fields in supported photocatalytic reactors [47–49]. However, due to intrinsic statistic nature, the evaluation does not represent the phenomenological behaviour of the photon transport. On the other hand, the semi-predictive radiation models that depict the phenomenological behaviour of radiative process have been proposed, being the derivatization of characteristic matrix an advantageous model to predict the radiation absorption field in different reactor geometries [46].

Besides the radiative process, another aspect on supported catalyst reactor controls the phenomenological behaviour of the photocatalytic process. Therefore, to elucidate the physical interaction of the fluid with the catalytic particle, as well as the rate of chemical change, kinetic and mass transfer model must be established to describe the physical-chemical behaviour of the photocatalytic process. Even more, the diffusion process (external or internal) takes a major relevance because the constant interaction of the fluid with the supported particles and it would depend on the flow regime.

b. Suspended photocatalytic reactor

Contrary to the attached photocatalytic reactor, suspended photocatalytic reactor needs a separation process at the ending stage of the treatment, but higher rates of decompositions have been observed in this type of reactor [11,50–57]. Moreover, it has been demonstrated that the mass transfer process has no relevance to the phenomenological behaviour of slurry reactors [58]. Likewise, the radiative process has been widely evaluated with three different models: Monte Carlo approach, radiative transfer equation (RTE) and six-flux model (SFM). As mentioned above, Monte Carlo can be used for the simulation of the radiative process and has been widely employed for the validation of RTE and SFM [47,59]. Similar to reactors with a supported photocatalyst, three different phenomena are carried out within particles in suspension inside the reactor: absorption, scattering, and emission. These are well described by the RTE, but the mathematical complexity leads to a high computational time. As another option, the six-flux model has been proposed and it is a simplified method of the RTE based on geometric optics, maintaining the fundamental aspects of radiation field modeling. The algebraic structure allows an easy implementation and low computational times, even for solar radiation on tubular and CPC reactors [53]. Moreover, the annular reactor, as well as the flat plate reactor, have been evaluated under different conditions, demonstrating the feasibility of the SFM [57,60]. Reactor geometries showed in Figure 4, could be applied on the suspended photocatalyst reactor as previously discussed. Finally, quantum yield appears as the quantity of absorbed light that is utilized for the activation of the semiconductor (*i.e.* electron-hole pair generation), and it depends on the intrinsic characteristics of the photocatalyst as well as its relationship with the reactive media. These two main characteristics depict the rate of electron-hole pair generation and must be considered in the development of the kinetic model [61]. Once the four fundamental aspects are compacted into the rate of reaction, the design of a photocatalytic reactor can be established, and the operational parameters must be determined for the best condition.

## *2.2. Blue wastewater*

Wastewater generated on public transportation (aircraft, ships, trains, buses, etc.), commonly known as blue wastewater, represents a great concern because this kind of effluents contains dyes (*e.g.* methylene blue), sanitizing products and biodegradable organic matter. Blue wastewater can also contain aldehydes, glycols, aromatics, ammonia, and glyoxal [62]. This effluent becomes a serious problem in conventional wastewater treatment because the biological process efficiency decreases due to the inhibition of microbial activity and, consequently, the collapse of biological reactors. In addition, there are only a few studies for evaluation of non-conventional blue wastewater treatment. Liu *et al.* (2007) [63] evaluated a membrane bioreactor (MBR) process for treating Qingdao international airport blue wastewater. During two years of operation, the MBR process demonstrated to be effective to accomplish the water discharge and reuse quality requirements at the airport. In addition, Moreno-Andrade *et al.* (2014) [64] implemented a sequencing batch reactor (SBR) with acclimated microorganisms for toilet wastewater treatment generated in aircraft. At concentrations of ~1 g COD/L, efficiencies about 80% were achieved. To the best of our knowledge, those two articles are the unique studies that implemented non-conventional biological treatment for blue wastewater.

## *2.3. Photocatalytic degradation process*

Treatment of complex wastewater by photocatalytic processes have been tested in the last decades. Lima *et al*. (2015) [65] successfully decolorized a real sample of textile wastewater (mainly azo dyes) through a simple, fast, and efficient photocatalytic treatment by using of polypyrrole as the photocatalyst. Under sunlight irradiation, 98% of decolorization was achieved in 30 minutes, and the generated by-products were non-toxic in nature. Besides, the treatment for hospital effluent containing moxifloxacin was developed via heterogeneous photocatalysis with $TiO_2$ as the photocatalyst. It was found that the advanced oxidation process

applied for the treatment of the hospital effluent was two times slower than the result obtained with deionized water. Deactivation of the photocatalyst by means of inorganics (*e.g.* chloride and bicarbonates), organic matrix constituents (like organic matter and humic substances) and low UV light irradiation, may be the primary cause of the decrease for the degradation rate of moxifloxacin. About 70% of the inhibitory effects for degradation of moxifloxacin were observed, showing high relevance for the photocatalytic treatment of complex wastewater [30]. For these reasons, there is a great interest in synthesizing and testing different semiconductor materials with photocatalytic activity at visible light to reduce costs, to avoid poison and deactivation of the catalyst.

Nowadays in the field of photocatalysis, ZnO has emerged as the leading candidate as an efficient and promising semiconductor in green environmental management system because of its unique characteristics, such as direct and wide band gap in the near-UV spectral region, strong oxidation ability, good photocatalytic property and a large free-extinction binding energy so that excitonic emission processes can persist at or even above room temperature. This last feature diminishes the effect of the recombination process enhancing the photocatalytic activity for the degradation process [66]. Moreover, the price of zinc oxide in the market is about US$1,500/Ton, which is lower than the price of titanium dioxide (US%28,000/Ton) (Information provided by Zinc Nacional company), so the importance to improve the photodegradation efficiency of ZnO over $TiO_2$. Among the strategies to modify the chemical structure of ZnO, anionic and cationic doping agents appear as an easy and reliable strategy to improve the photocatalytic characteristics of this material. However, a high degree of engineering design is necessary to avoid the saturation of the dopant agent, that further increases the recombination of an electron-hole pair. Therefore, dye sensitization and coupling with polymers have been recently studied. The polymeric coating of zinc oxide has been evaluated improving its photocatalytic characteristics [37]. The photocatalytic decolorization of methylene blue with ZnO-polypyrrole composite was about 20-times greater than pure ZnO in the same conditions. This can be attributed to the ligand to metal charge transfer mechanism

that governs the interfacial electron transfer among the polymeric matrix. Therefore, the importance of the selection of a photoactive polymer structure that enhances the visible-light absorption characteristics and the electron transfer capacity.

Likewise, dye sensitization has been employed as a simple and interesting strategy for achieving effective visible light harvesting and multielectron transfer on the photocatalytic process [23]. This alternative has been mainly applied for hydrogen production, but less explored for the photocatalytic degradation processes [67]. Recently, sensitization of $TiO_2$ and ZnO, with natural and artificial dyes, was successfully employed for photocatalytic degradation of methylene blue, sulfamethoxazole and rose bengal, increasing the photocatalytic activity [68–70]. Instead, green pigments have demonstrated an intrinsic potential for photochemical processes, due to mimicking photosynthesis. The chloroplast furnished on the polymeric structure of the plant cell contains the chlorophyll molecules, which grant its excellent photochemical properties for the carbon dioxide reduction, producing oxygen and hydrocarbon for the cell structure. There are a few studies about chlorophyll-sensitized materials for photocatalytic degradation processes, observing a major photoreduction mechanism, demonstrating that free Mg acts as a trapping site of the charge carriers that further enhance the electron transport through the semiconductor lattice [71,72]. This behaviour represented on semiconductor materials has been called as a Z-scheme mechanism, derived from the classic photosynthesis. However, metal oxides do not mimic the photochemical mechanism present on the plant cell. Therefore, coupling the chlorophyll molecules onto a polymeric semiconductor may be the key for highly active materials for the photocatalytic process. Although the polymeric semiconductors that have been studied, carbon nitride appears as the best candidate to enhance its optical process due to its high potential as an electron carrier material [34,73]. However, the high cost of reagents, complicated and expensive synthesis methods, do not allow its application on the remediation of wastewater. Thereby, phenolic resins have emerged as a low cost, reliable, highly active material for photocatalytic processes [74–78]. This polymer has been

studied for both wastewater remediation and hydrogen production, being modified with titanium oxide and ruthenium to enhance its photochemical properties, leading to a better photocatalytic activity. Likewise, to the best of our knowledge, there are no studies about modification of phenolic resin with zinc oxide as well as phenolic resin dye-sensitization with natural pigments, for its application on the photocatalytic degradation process.

## *2.4. Modeling of the photocatalytic degradation process*

The six-flux model appears as the most reliable mathematical expression to depict the radiation distribution across the reactor volume. However, some disadvantages have been limited the further utilization on the photocatalytic process. Nevertheless, Acosta-Herazo *et al*. (2016) simplify the six-flux model, incorporating the generalized Henyey-Greenstein (HG) phase function for the distribution probabilities under different conditions [54]. Likewise, to the best of our knowledge, titanium dioxide is the only semiconductor that has been evaluated for radiant field estimation. Therefore, the assessment of SFM-HG for other semiconductors would increase the interest in the evaluation of the radiant field as a characterization method. On the other hand, quantum yield has been evaluated from the indirect determination of the parameters of a variety of kinetic models, but recent researchers have been implemented novel quantum yield mathematical models. Mueses *et al.* (2013) proposed for the first time a mathematical model for the evaluation of the quantum yield depending on the SFM and the intrinsic characteristics of the semiconductor. The model predicts the quantum yield with a high degree of confidence for titanium dioxide under different conditions [61]. Thus, there is an opportunity for the simulation of both quantum yield and SFM for novel materials because the prediction of quantum yield relies on the SFM simulation.

Moreover, different kinetic models have been employed for the photocatalytic degradation of organic contaminants, being the most used the pseudo-first-order and Langmuir-Hinshelwood models [79–82]. However, these models do not depict the phenomenological behaviour of the photocatalytic process, thereby novel kinetic models considering the absorption of light into the reactor and/or the

quantum yield of the semiconductor has been proposed for a better understanding of the process and the influence of the operational parameters [11,57,83–86]. Finally, Mueses *et al*. (2013) proposed a generalized kinetic model based on the hydroxyl radical attack and the activation of the semiconductor. This generalized kinetic model represents an extension of the reaction scheme proposed by Turchi & Ollis (1990) and a modification on the estimation of the rate of electron-hole pair generation developed by Alfano et al. (1997) [26,50]. However, the novel materials do not follow the same mechanisms as titanium dioxide for the photocatalytic degradation process. Thereby, a novel kinetic model must be proposed considering the attack of the other reactive oxygen species. Even more, the generalized kinetic model proposed by Mueses *et al*. (2013) does not consider the rate of interfacial electron transfer as observed on the direct-indirect model [85]. Consequently, this lack of information could give a questionable response to the evaluation of the photocatalytic degradation process at different operational conditions.

For the above-mentioned reasons, the aim of this study is to propose an extension of kinetic and quantum yield model as well as the evaluation of the radiation absorption phenomena on a visible-LED reactor for the photocatalytic blue wastewater degradation employing a novel material as a photocatalyst, based on zinc oxide, green pigments, and phenolic resins.

### *A. Hypothesis*

Mathematical modeling of blue wastewater photocatalytic degradation on a tubular reactor under visible-LED irradiation by a composite based on phenolic resins and, zinc oxide or green pigments, considering the physical-chemical mechanisms of degradation, enhance the prediction of experimental data.

### *B. General objective*

To develop a mathematical model that predicts the photocatalytic degradation of blue wastewater on a tubular reactor under visible-LED irradiation by a composite based on phenolic resin with ZnO and phenolic resin with green pigments.

### *C. Specific objectives*

- To synthesize phenol-formaldehyde resins and to incorporate ZnO and chlorophyll.
- To determine the physical-chemical properties of the obtained materials.
- To develop a generalized kinetic model for any photocatalytic degradation mechanisms via reactive species.
- To determine the photocatalytic degradation mechanisms via reactive species of the synthesized materials.
- To evaluate the photocatalytic activity of the obtained materials under visible-LED irradiation by methylene blue degradation kinetic experiments.
- To validate the generalized kinetic model from the rate of electron-hole pair generation and degradation kinetics on a tubular reactor under visible-LED irradiation.
- To evaluate the photocatalytic degradation of blue wastewater with the best photocatalyst.

# 3. Model

## *3.1. Effective photocatalytic mechanism model*

In this work, a new approach for estimating the effective physicochemical mechanism via reactive oxygen species on photocatalytic degradation processes is proposed. This model is based on the following assumptions:

1. For photoactive semiconductors, interfacial charge transfer ($e^-$ and $h^+$ trapping) for generation of reactive oxygen species ($H_2O \rightarrow OH^{\cdot}, O_2 \rightarrow O_2^{-\cdot}, H_2O + O_2 \rightarrow H_2O_2, \chi^- \rightarrow \chi.$) or other chemical reactions to an electron donor or acceptor adsorbate ($A \rightarrow A^-, D \rightarrow D^+$) will act simultaneously on the photocatalytic process [24,25].
2. Depending on its electrochemical constraint, the feasibility of the generation of each reactive species could be estimated via scavenger tests.

The effective fraction contribution of each mechanism ($\varphi_{i=h^+, e^-, H_2O_2, OH^{\cdot}, O_2^{-\cdot}, \chi^{\cdot}}$) on the photocatalytic activity can be calculated by the following equation:

$$\varphi_i = 1 - \frac{\mathrm{k}_{app,scavenger}^{atm}}{\mathrm{k}_{app,control}^{atm}} \ldots (2)$$

Where $k_{app,control}^{atm}$ is the apparent reaction rate constant for the control experiment without addition of scavenger, $k_{app,scavenger}^{atm}$ is the apparent reaction rate constant of the scavenging experiment of the $i$th interfacial charge transfer or reactive oxygen species on aerobic or anaerobic atmosphere, respectively. Finally, the photocatalytic mechanism effectiveness ($\mathcal{M}_{eff}$) constraint must be approximately equal to unity; therefore, the sum of the fraction contribution is given by:

$$\mathrm{M}_{eff} = \sum_{i=h^+, e^-, OH^{\cdot}, O_2^{-\cdot}, \chi^{\cdot}} \varphi_i = \varphi_{h^+} + \varphi_{e^-} + \varphi_{O_2^{-\cdot}} + \varphi_{H_2O_2, OH^{\cdot}} + \varphi_{\chi^{\cdot}} = 1 \ldots (3)$$

Two general cases can be proposed to estimate the effective contribution of photogenerated reactive species: without reactive ionic species and with reactive ionic species.

In the first case, the conventional mechanism evaluates hole oxidation, electron reduction, hydrogen peroxide, hydroxyl radical and superoxide radical.

First, the photogenerated hole scavenging would depend on the addition of electron donor scavenger (EDS) under anaerobic conditions. This assumption implies that both hydrogen peroxide and hydroxyl radical need dissolved oxygen to react with water molecules, as well as the photogenerated hole energy:

$$\varphi_{h^+} = \left(1 - \frac{k_{app,EDS}^{N_2}}{k_{app,control}^{N_2}}\right)\varphi_{N_2} \quad \ldots(4)$$

On the other hand, the scavenging of the excited electron would depend on the addition of the electron acceptor scavenger (EAS) under anaerobic conditions. In water systems, regardless of the electron-donor nature of the pollutant, dissolved oxygen is the only species that can be reduced by electron transport, generating superoxide radical. Therefore, in the absence of oxygen, electron transport would be redirected to the pollutant:

$$\varphi_{e^-} = \left(1 - \frac{k_{app,EAS}^{N_2}}{k_{app,control}^{N_2}}\right)\varphi_{N_2} \quad \ldots(5)$$

In both contributions, $\varphi_{N_2}$ depicts the anaerobic contribution of the photocatalytic activity, and can be denoted as:

$$\varphi_{N_2} = \frac{k_{app,control}^{N_2}}{k_{app,control}^{O_2}} \quad \ldots(6)$$

Moreover, EAS can be employed under aerobic conditions for the scavenging of superoxide radical. Likewise, EAS scavenges superoxide radical as well as the excited electrons, so it is necessary to subtract the electron contribution:

$$\varphi_{O_2^{-}\cdot} = \left(1 - \frac{k_{app,EAS}^{O_2}}{k_{app,control}^{O_2}}\right) - \varphi_{e^-} \quad \ldots(7)$$

Finally, the contribution of hydrogen peroxide and hydroxyl radical could be subtracted from equation (7) because the scavenging of the reducing species would allow the attack of the other reactive species ($H_2O_2, OH\cdot, h^+$). Also, the hole contribution must be taken into account in the mathematical structure:

$$\varphi_{H_2O_2,OH\cdot} = \left(1 - \varphi_{O_2^{-}\cdot}\right) - \varphi_{h^+} \quad \ldots(8)$$

To validate the effective photocatalytic mechanism, equation (3) must be accomplished, then combining equations (4-8) can give:

$$M_{eff} = \sum_{i=h^+,e^-,OH\cdot,O_2^-\cdot,\chi\cdot} \varphi_i = \left(1-\frac{k_{app,EDS}^{N_2}}{k_{app,control}^{N_2}}\right)\left(\frac{k_{app,control}^{N_2}}{k_{app,control}^{O_2}}\right)+\left(1-\frac{k_{app,EAS}^{N_2}}{k_{app,control}^{N_2}}\right)\left(\frac{k_{app,control}^{N_2}}{k_{app,control}^{O_2}}\right)+\left(1-\frac{k_{app,EAS}^{O_2}}{k_{app,control}^{O_2}}\right)$$

$$-\left(1-\frac{k_{app,EAS}^{N_2}}{k_{app,control}^{N_2}}\right)\left(\frac{k_{app,control}^{N_2}}{k_{app,control}^{O_2}}\right)+\left[1-\left(1-\frac{k_{app,EAS}^{O_2}}{k_{app,control}^{O_2}}\right)-\left(1-\frac{k_{app,EAS}^{N_2}}{k_{app,control}^{N_2}}\right)\left(\frac{k_{app,control}^{N_2}}{k_{app,control}^{O_2}}\right)\right]-\left(1-\frac{k_{app,EDS}^{N_2}}{k_{app,control}^{N_2}}\right)\left(\frac{k_{app,control}^{N_2}}{k_{app,control}^{O_2}}\right)=1$$

$$M_{eff} = \sum_{i=h^+,e^-,OH\cdot,O_2^-\cdot,\chi\cdot} \varphi_i = \left(\frac{k_{app,control}^{N_2}+k_{app,control}^{N_2}+k_{app,control}^{O_2}+k_{app,EAS}^{N_2}+k_{app,EAS}^{O_2}+k_{app,EDS}^{N_2}}{k_{app,control}^{O_2}}\right)$$

$$-\left(\frac{k_{app,EDS}^{N_2}+k_{app,EAS}^{N_2}+k_{app,EAS}^{O_2}+k_{app,control}^{N_2}+k_{app,control}^{N_2}}{k_{app,control}^{O_2}}\right)$$

$$M_{eff} = \sum_{i=h^+,e^-,OH\cdot,O_2^-\cdot,\chi\cdot} \varphi_i = \left(\frac{k_{app,control}^{O_2}}{k_{app,control}^{O_2}}\right)=1$$

For the second case, ionic species (present in the reactive media) could generate reactive species. In previous reports, carbonate and sulfate anions have been transformed into anion radicals via photocatalysis to degrade organic pollutants [87,88]. Also, it was reported that carbonate species deactivate the photocatalytic process, reducing the degradation of pollutants in aqueous solutions [28,29] Therefore, the contribution of ionic species in solution must be considered in the effectiveness of the photocatalytic mechanism.

Foremost, the contribution of reactive ionic species ($\varphi_{\chi\cdot}$) would depend on ionic species scavenger ($S\chi$) under aerobic conditions, and the mathematical structure of the model must be defined as the lack of contribution (*i.e.* anaerobic contribution), then:

$$\varphi_{\chi\cdot} = \left(\frac{k_{app,S\chi}^{O_2}}{k_{app,control}^{O_2}}\right) \ldots (9)$$

If $\varphi_{\chi\cdot} < 1$, ionic species would contribute on the photocatalytic degradation mechanism via $\chi$ radical formation. However, if $\varphi_{\chi\cdot} > 1$, ionic species would deactivate the process, affecting negatively to the photocatalytic degradation.

Therefore, to avoid mathematical discrepancies, the absolute numerical value of $\varphi_{\chi\cdot}$ must be employed for the estimation of the other reactive species contribution. Subtracting this contribution from the total effect would be associated with the reactive oxygen species contribution present in conventional mechanism:

$$\varphi_{ROS} = \left(1 - \left|\varphi_{\chi\cdot}\right|\right) \ldots(10)$$

Therefore, the specific contribution of each mechanism can be modified from equation (4, 5, 7 and 8), as follows:

$$\varphi_{h^+} = \left(1 - \frac{\mathrm{k}_{app,EDS}^{N_2}}{\mathrm{k}_{app,control}^{N_2}}\right)\varphi_{N_2}\varphi_{ROS} \ldots(11)$$

$$\varphi_{e^-} = \left(1 - \frac{\mathrm{k}_{app,EAS}^{N_2}}{\mathrm{k}_{app,control}^{N_2}}\right)\varphi_{N_2}\varphi_{ROS} \ldots(12)$$

$$\varphi_{O_2^-\cdot} = \left(1 - \frac{\mathrm{k}_{app,EAS}^{O_2}}{\mathrm{k}_{app,control}^{O_2}}\right)\varphi_{ROS} - \varphi_{e^-} \ldots(13)$$

$$\varphi_{H_2O_2,OH\cdot} = \left(\frac{\mathrm{k}_{app,EAS}^{O_2}}{\mathrm{k}_{app,control}^{O_2}}\right)\varphi_{ROS} - \varphi_{h^+} \ldots(14)$$

Where every contribution of the conventional mechanism is associated with the lack of reactive ionic species contribution ($\varphi_{ROS}$).

## *3.2. Generalized kinetic model*

In recent years, great progress has been made in material preparation and photocatalytic property studies. However, thermodynamics and kinetics of photocatalysis have been poorly discussed to date, which leads to a fact that some researchers knew less about them and explained the observed experimental results incorrectly [84]. Many different empirical and semi-predictive kinetic models for photocatalytic degradation process have been proposed. Nevertheless, only a few studies represent the phenomenological behaviour of the degradation process.

Mueses *et al*. (2013) were the first group to evaluate the Turchi & Ollis generalized kinetic model [89], for the photocatalytic degradation of organic pollutants under solar irradiation, employing $TiO_2$ P25. Likewise, this model takes into account the light-activation mechanism of the semiconductor, the recombination process, the mechanistic generation of hydroxyl radical and the further attack on the organic pollutant. Nonetheless, novel materials have been demonstrated that different reactive oxygen species could be generated, as well as the combined effect of light-temperature that further increases the interfacial electron transfer has not been considered. Therefore, based on the reaction scheme developed by Turchi & Ollis [89], an extended reaction scheme is proposed, and the rate of reaction kinetic model is established based on the steps shown in Table 1.

**Table 1.** Photocatalytic reaction scheme

| | | |
|---|---|---|
| Activation | $S \xrightarrow{h\upsilon} h_f^+ + e_f^-$ | 1 |
| Recombination | $h_f^+ + e_f^- \rightarrow heat$ | 2 |
| Ionization | $O_L^{2-} + H_2O \leftrightarrow O_L H + OH^-$ | 3 |
| Adsorption | $OH^- + S_{ox} \leftrightarrow S_{ox} - OH^-$ | 4 |
| | $O_2 + S_{ox} \leftrightarrow S_{ox} - O_2$ | 5 |
| | $\chi + S_{ox} \leftrightarrow S_{ox} - \chi$ | 6 |
| | $h_f^+ + S_{ox} \leftrightarrow h_s^+$ | 7 |
| | $OH\cdot + S_{ox} \leftrightarrow S_{ox} \mid OH\cdot$ | 8 |
| | $e_f^- + S_{ox} \leftrightarrow e_s^-$ | 9 |
| | $O_2^- \cdot + S_{ox} \leftrightarrow S_{ox} \mid O_2^- \cdot$ | 10 |
| | $\chi^+ \cdot + S_{ox} \leftrightarrow S_{ox} \mid \chi^+ \cdot$ | 11 |
| | $\chi^- \cdot + S_{ox} \leftrightarrow S_{ox} \mid \chi^- \cdot$ | 12 |
| | $Site + R_i \leftrightarrow R_{i,ads}$ | 13 |

| | | |
|---|---|---|
| Hole trapping | $S_{ox} - OH^- + h_s^+ \leftrightarrow S_{ox} + S_{ox} \mid OH\cdot$ | 14 |
| | $S_{ox} - OH^- + h_f^+ \leftrightarrow S_{ox} \mid OH\cdot$ | 15 |
| | $OH^- + h_s^+ \leftrightarrow S_{ox} + OH\cdot$ | 16 |
| | $OH^- + h_f^+ \leftrightarrow OH\cdot$ | 17 |
| | $S_{ox} - \chi + h_s^+ \leftrightarrow S_{ox} + S_{ox} \mid \chi^+\cdot$ | 18 |
| | $S_{ox} - \chi + h_f^+ \leftrightarrow S_{ox} \mid \chi^+\cdot$ | 19 |
| | $\chi + h_s^+ \leftrightarrow S_{ox} + \chi^+\cdot$ | 20 |
| | $\chi + h_f^+ \leftrightarrow \chi^+\cdot$ | 21 |
| Hole attack | $h_s^+ + R_{i,ads} \rightarrow S_{ox} + R_{j,ads}$ | 22 |
| | $h_f^+ + R_{i,ads} \rightarrow R_{j,ads}$ | 23 |
| | $h_s^+ + R_i \rightarrow S_{ox} + R_j$ | 24 |
| | $h_f^+ + R_i \rightarrow R_j$ | 25 |
| Hydroxyl radical attack | $S_{ox} \mid OH\cdot + R_{i,ads} \rightarrow S_{ox} + R_{j,ads}$ | 26 |
| | $OH\cdot + R_{i,ads} \rightarrow R_{j,ads}$ | 27 |
| | $S_{ox} \mid OH\cdot + R_i \rightarrow S_{ox} + R_j$ | 28 |
| | $OH\cdot + R_i \rightarrow R_j$ | 29 |
| Cation radical attack | $S_{ox} \mid \chi^+\cdot + R_{i,ads} \rightarrow S_{ox} + R_{j,ads}$ | 30 |
| | $\chi^+\cdot + R_{i,ads} \rightarrow R_{j,ads}$ | 31 |
| | $S_{ox} \mid \chi^+\cdot + R_i \rightarrow S_{ox} + R_j$ | 32 |
| | $\chi^+\cdot + R_i \rightarrow R_j$ | 33 |
| Electron trapping | $S_{ox} - O_2 + e_s^- \leftrightarrow S_{ox} + S_{ox} \mid O_2^-\cdot$ | 34 |
| | $S_{ox} - O_2 + e_f^- \leftrightarrow S_{ox} \mid O_2^-\cdot$ | 35 |

| | | |
|---|---|---|
| | $O_2 + e_s^- \leftrightarrow S_{ox} + O_2^- \cdot$ | 36 |
| | $O_2 + e_f^- \leftrightarrow O_2^- \cdot$ | 37 |
| | $S_{ox} - \chi + e_s^- \leftrightarrow S_{ox} + S_{ox} \mid \chi^- \cdot$ | 38 |
| | $S_{ox} - \chi + e_f^- \leftrightarrow S_{ox} \mid \chi^- \cdot$ | 39 |
| | $\chi + e_s^- \leftrightarrow S_{ox} + \chi^- \cdot$ | 40 |
| | $\chi + e_f^- \leftrightarrow \chi^- \cdot$ | 41 |
| Electron attack | $e_s^- + R_{i,ads} \rightarrow S_{ox} + R_{j,ads}$ | 42 |
| | $e_f^- + R_{i,ads} \rightarrow R_{j,ads}$ | 43 |
| | $e_s^- + R_i \rightarrow S_{ox} + R_j$ | 44 |
| | $e_f^- + R_i \rightarrow R_j$ | 45 |
| Superoxide radical attack | $S_{ox} \mid O_2^- \cdot + R_{i,ads} \rightarrow S_{ox} + R_{j,ads}$ | 46 |
| | $O_2^- \cdot + R_{i,ads} \rightarrow R_{j,ads}$ | 47 |
| | $S_{ox} \mid O_2^- \cdot + R_i \rightarrow S_{ox} + R_j$ | 48 |
| | $O_2^- \cdot + R_i \rightarrow R_j$ | 49 |
| Anion radical attack | $S_{ox} \mid \chi^- \cdot + R_{i,ads} \rightarrow S_{ox} + R_{j,ads}$ | 50 |
| | $\chi^- \cdot + R_{i,ads} \rightarrow R_{j,ads}$ | 51 |
| | $S_{ox} \mid \chi^- \cdot + R_i \rightarrow S_{ox} + R_j$ | 52 |
| | $\chi^- \cdot + R_i \rightarrow R_j$ | 53 |
| | $h_f^+ + e_f^- \rightarrow heat$ | 54 |

*Semiconductor $(S)$; surface $(s)$; free $(f)$; i$^{th}$ component $(i)$; j$^{th}$ component $(j)$; oxidized $(ox)$; adsorbed $(ads)$.

For a particle with a surface area equal to $a_S$ and volume equal to $v_P$, the rate of transformation of reactant $R_i$ is given by:

$$\begin{aligned}
-r_P &= \mathrm{k}_{22} C_{h_s^+} C_{R_{i,ads}} a_s^2 + \mathrm{k}_{23} C_{h_f^+} C_{R_{i,ads}} a_s + \mathrm{k}_{24} C_{h_s^+} C_{R_i} a_s + \mathrm{k}_{25} C_{h_f^+} C_{R_i} \\
&+ \mathrm{k}_{26} C_{S_{ox}|OH.} C_{R_{i,ads}} a_s^2 + \mathrm{k}_{27} C_{OH.} C_{R_{i,ads}} a_s + \mathrm{k}_{28} C_{S_{ox}|OH.} C_{R_i} a_s + \mathrm{k}_{29} C_{OH.} C_{R_i} \\
&+ \mathrm{k}_{30} C_{S_{ox}|\chi^+.} C_{R_{i,ads}} a_s^2 + \mathrm{k}_{31} C_{\chi^+.} C_{R_{i,ads}} a_s + \mathrm{k}_{32} C_{S_{ox}|\chi^+.} C_{R_i} a_s + \mathrm{k}_{33} C_{\chi^+.} C_{R_i} \\
&+ \mathrm{k}_{42} C_{e_s^-} C_{R_{i,ads}} a_s^2 + \mathrm{k}_{43} C_{e_f^-} C_{R_{i,ads}} a_s + \mathrm{k}_{44} C_{e_s^-} C_{R_i} a_s + \mathrm{k}_{45} C_{e_f^-} C_{R_i} \\
&+ \mathrm{k}_{46} C_{S_{ox}|O_2^-.} C_{R_{i,ads}} a_s^2 + \mathrm{k}_{47} C_{O_2^-.} C_{R_{i,ads}} a_s + \mathrm{k}_{48} C_{S_{ox}|O_2^-.} C_{R_i} a_s + \mathrm{k}_{49} C_{O_2^-.} C_{R_i} \\
&+ \mathrm{k}_{50} C_{S_{ox}|\chi^-.} C_{R_{i,ads}} a_s^2 + \mathrm{k}_{51} C_{\chi^-.} C_{R_{i,ads}} a_s + \mathrm{k}_{52} C_{S_{ox}|\chi^-.} C_{R_i} a_s + \mathrm{k}_{53} C_{\chi^-.} C_{R_i}
\end{aligned} \quad \ldots(15)$$

Where:

$r_P[=]\ mol\ R_i\ s^-\ particle^-$

$\mathrm{k}_{22}, \mathrm{k}_{26}, \mathrm{k}_{30}, \mathrm{k}_{42}, \mathrm{k}_{46}\ \&\ \mathrm{k}_{50}[=]\ particle\ mol^-s^-$

$\mathrm{k}_{23,24}, \mathrm{k}_{27,28}, \mathrm{k}_{31,32}, \mathrm{k}_{43,44}, \mathrm{k}_{47,48}\ \&\ \mathrm{k}_{51,52}[=]\ m^3\ mol^-s^-$

$\mathrm{k}_{25}, \mathrm{k}_{29}, \mathrm{k}_{33}, \mathrm{k}_{45}, \mathrm{k}_{49}\ \&\ \mathrm{k}_{53}[=]\ m^6\ mol^-s^-particle^-$

The concentration of the bulk, such as $C_{h_f^+}, C_{OH.}, C_{\chi^+.}, C_{e_f^-}, C_{O_2^-.}, C_{\chi^-.}\ \&\ C_{R_i}$ must be thought of as those existing in the fluid film adjacent and very close to the catalytic particle.

The adsorbed organic substances concentration on the semiconductor, $C_{h_s^+}, C_{S_{ox}|OH.}, C_{S_{ox}|\chi^+.}, C_{e_s^-}, C_{S_{ox}|O_2^-.}, C_{S_{ox}|\chi^-.}\ \&\ C_{R_{i,ads}}$, can be obtained assuming equilibrium for the reactions (4 – 13):

$$r_{C_{S_{ox}-OH^-}} = \mathrm{k}_{4^-} C_{S_{ox}-OH^-} - \mathrm{k}_{4^+} C_{OH^-} C_{S_{ox}} = 0 \ldots(16)$$

$$r_{C_{S_{ox}-O_2}} = \mathrm{k}_{5^-} C_{S_{ox}-O_2} - \mathrm{k}_{5^+} C_{O_2} C_{S_{ox}} = 0 \ldots(17)$$

$$r_{C_{S_{ox}-\chi}} = \mathrm{k}_{6^-} C_{S_{ox}-\chi} - \mathrm{k}_{6^+} C_{\chi} C_{S_{ox}} = 0 \ldots(18)$$

$$r_{C_{h_s^+}} = \mathrm{k}_{7^-} C_{h_s^+} - \mathrm{k}_{7^+} C_{h_f^+} C_{S_{ox}} = 0 \ldots(19)$$

$$r_{C_{S_{ox}|OH.}} = \mathrm{k}_{8^-} C_{S_{ox}|OH.} - \mathrm{k}_{8^+} C_{OH.} C_{S_{ox}} = 0 \ldots(20)$$

$$r_{C_{e_s^-}} = \mathrm{k}_{9^-} C_{e_s^-} - \mathrm{k}_{9^+} C_{e_f^-} C_{S_{ox}} = 0 \ldots (21)$$

$$r_{C_{S_{ox}|O_2^-.}} = \mathrm{k}_{10^-} C_{S_{ox}|O_2^-.} - \mathrm{k}_{10^+} C_{O_2^-.} C_{S_{ox}} = 0 \ldots (22)$$

$$r_{C_{S_{ox}|\chi^+.}} = \mathrm{k}_{11^-} C_{S_{ox}|\chi^+.} - \mathrm{k}_{11^+} C_{\chi^+.} C_{S_{ox}} = 0 \ldots (23)$$

$$r_{C_{S_{ox}|\chi^-.}} = \mathrm{k}_{12^-} C_{S_{ox}|\chi^-.} - \mathrm{k}_{12^+} C_{\chi^-.} C_{S_{ox}} = 0 \ldots (24)$$

$$r_{C_{R_{i,ads}}} = \mathrm{k}_{13^-} C_{R_{i,ads}} - \mathrm{k}_{13^+} C_{R_i} C_{S_{ox}} = 0 \ldots (25)$$

$$C_{S_{ox}-OH^-} = \mathrm{K}_4 C_{OH^-} C_{S_{ox}} \ldots (26)$$

$$C_{S_{ox}-O_2} = \mathrm{K}_5 C_{O_2} C_{S_{ox}} \ldots (27)$$

$$C_{S_{ox}-\chi} = \mathrm{K}_6 C_{\chi} C_{S_{ox}} \ldots (28)$$

$$C_{h_s^+} = \mathrm{K}_7 C_{h_f^+} C_{S_{ox}} \ldots (29)$$

$$C_{S_{ox}|OH.} = \mathrm{K}_8 C_{OH.} C_{S_{ox}} \ldots (30)$$

$$C_{e_s^-} = \mathrm{K}_9 C_{e_f^-} C_{S_{ox}} \ldots (31)$$

$$C_{S_{ox}|O_2^-.} = \mathrm{K}_{10} C_{O_2^-.} C_{S_{ox}} \ldots (32)$$

$$C_{S_{ox}|\chi^+.} = \mathrm{K}_{11} C_{\chi^+.} C_{S_{ox}} \ldots (33)$$

$$C_{S_{ox}|\chi^-.} = \mathrm{K}_{12} C_{\chi^-.} C_{S_{ox}} \ldots (34)$$

$$C_{R_{i,ads}} = \mathrm{K}_{13} C_{R_i} C_{Site} \ldots (35)$$

Substituting equations (26 – 35) into equation (15) we have:

$$\begin{aligned}
-r_P = {} & \mathrm{k}_{22}\mathrm{K}_7 C_{h_f^+} C_{S_{ox}} \mathrm{K}_{13} C_{R_i} C_{Site} a_s^2 + \mathrm{k}_{23} C_{h_f^+} \mathrm{K}_{13} C_{R_i} C_{Site} a_s + \mathrm{k}_{24}\mathrm{K}_7 C_{h_f^+} C_{S_{ox}} C_{R_i} a_s + \mathrm{k}_{25} C_{h_f^+} C_{R_i} \\
& + \mathrm{k}_{26}\mathrm{K}_8 C_{OH.} C_{S_{ox}} \mathrm{K}_{13} C_{R_i} C_{Site} a_s^2 + \mathrm{k}_{27} C_{OH.} \mathrm{K}_{13} C_{R_i} C_{Site} a_s + \mathrm{k}_{28}\mathrm{K}_8 C_{OH.} C_{S_{ox}} C_{R_i} a_s + \mathrm{k}_{29} C_{OH.} C_{R_i} \\
& + \mathrm{k}_{30}\mathrm{K}_{11} C_{\chi^+.} C_{S_{ox}} \mathrm{K}_{13} C_{R_i} C_{Site} a_s^2 + \mathrm{k}_{31} C_{\chi^+.} \mathrm{K}_{13} C_{R_i} C_{Site} a_s + \mathrm{k}_{32}\mathrm{K}_{11} C_{\chi^+.} C_{S_{ox}} C_{R_i} a_s + \mathrm{k}_{33} C_{\chi^+.} C_{R_i} \\
& + \mathrm{k}_{42}\mathrm{K}_9 C_{e_f^-} C_{S_{ox}} \mathrm{K}_{13} C_{R_i} C_{Site} a_s^2 + \mathrm{k}_{43} C_{e_f^-} \mathrm{K}_{13} C_{R_i} C_{Site} a_s + \mathrm{k}_{44}\mathrm{K}_9 C_{e_f^-} C_{S_{ox}} C_{R_i} a_s + \mathrm{k}_{45} C_{e_f^-} C_{R_i} \\
& + \mathrm{k}_{46}\mathrm{K}_{10} C_{O_2^-.} C_{S_{ox}} \mathrm{K}_{13} C_{R_i} C_{Site} a_s^2 + \mathrm{k}_{47} C_{O_2^-.} \mathrm{K}_{13} C_{R_i} C_{Site} a_s + \mathrm{k}_{48}\mathrm{K}_{10} C_{O_2^-.} C_{S_{ox}} C_{R_i} a_s + \mathrm{k}_{49} C_{O_2^-.} C_{R_i} \\
& + \mathrm{k}_{50}\mathrm{K}_{12} C_{\chi^-.} C_{S_{ox}} \mathrm{K}_{13} C_{R_i} C_{Site} a_s^2 + \mathrm{k}_{51} C_{\chi^-.} \mathrm{K}_{13} C_{R_i} C_{Site} a_s + \mathrm{k}_{52}\mathrm{K}_{12} C_{\chi^-.} C_{S_{ox}} C_{R_i} a_s + \mathrm{k}_{53} C_{\chi^-.} C_{R_i}
\end{aligned} \quad \ldots (36)$$

$$
\begin{aligned}
-r_P = {} & C_{h_f^+} C_{R_i} \left[ \mathrm{k}_{22} \mathrm{K}_7 C_{S_{ox}} \mathrm{K}_{13} C_{Site} a_s^2 + \mathrm{k}_{23} \mathrm{K}_{13} C_{Site} a_s + \mathrm{k}_{24} \mathrm{K}_7 C_{S_{ox}} a_s + \mathrm{k}_{25} \right] \\
& + C_{OH\cdot} C_{R_i} \left[ \mathrm{k}_{26} \mathrm{K}_8 C_{S_{ox}} \mathrm{K}_{13} C_{Site} a_s^2 + \mathrm{k}_{27} \mathrm{K}_{13} C_{Site} a_s + \mathrm{k}_{28} \mathrm{K}_8 C_{S_{ox}} a_s + \mathrm{k}_{29} \right] \\
& + C_{\chi^+\cdot} C_{R_i} \left[ \mathrm{k}_{30} \mathrm{K}_{11} C_{S_{ox}} \mathrm{K}_{13} C_{Site} a_s^2 + \mathrm{k}_{31} \mathrm{K}_{13} C_{Site} a_s + \mathrm{k}_{32} \mathrm{K}_{11} C_{S_{ox}} a_s + \mathrm{k}_{33} \right] \\
& + C_{e_f^-} C_{R_i} \left[ \mathrm{k}_{42} \mathrm{K}_9 C_{S_{ox}} \mathrm{K}_{13} C_{Site} a_s^2 + \mathrm{k}_{43} \mathrm{K}_{13} C_{Site} a_s + \mathrm{k}_{44} \mathrm{K}_9 C_{S_{ox}} a_s + \mathrm{k}_{45} \right] \\
& + C_{O_2^-\cdot} C_{R_i} \left[ \mathrm{k}_{46} \mathrm{K}_{10} C_{S_{ox}} \mathrm{K}_{13} C_{Site} a_s^2 + \mathrm{k}_{47} \mathrm{K}_{13} C_{Site} a_s + \mathrm{k}_{48} \mathrm{K}_{10} C_{S_{ox}} a_s + \mathrm{k}_{49} \right] \\
& + C_{\chi^-\cdot} C_{R_i} \left[ \mathrm{k}_{50} \mathrm{K}_{12} C_{S_{ox}} \mathrm{K}_{13} C_{Site} a_s^2 + \mathrm{k}_{51} \mathrm{K}_{13} C_{Site} a_s + \mathrm{k}_{52} \mathrm{K}_{12} C_{S_{ox}} a_s + \mathrm{k}_{53} \right]
\end{aligned} \quad \ldots(37)
$$

$$
\mathrm{k}_{ads,at\text{k-}h_f^+} = \mathrm{K}_7 C_{S_{ox}} \mathrm{K}_{13} C_{Site} a_s^2 + \mathrm{k}_{23} \mathrm{K}_{13} C_{Site} a_s + \mathrm{k}_{24} \mathrm{K}_7 C_{S_{ox}} a_s + \mathrm{k}_{25} \ldots(38)
$$

$$
\mathrm{k}_{ads,at\text{k-}OH\cdot} = \mathrm{k}_{26} \mathrm{K}_8 C_{S_{ox}} \mathrm{K}_{13} C_{Site} a_s^2 + \mathrm{k}_{27} \mathrm{K}_{13} C_{Site} a_s + \mathrm{k}_{28} \mathrm{K}_8 C_{S_{ox}} a_s + \mathrm{k}_{29} \ldots(39)
$$

$$
\mathrm{k}_{ads,at\text{k-}\chi^+\cdot} = \mathrm{k}_{30} \mathrm{K}_{11} C_{S_{ox}} \mathrm{K}_{13} C_{Site} a_s^2 + \mathrm{k}_{31} \mathrm{K}_{13} C_{Site} a_s + \mathrm{k}_{32} \mathrm{K}_{11} C_{S_{ox}} a_s + \mathrm{k}_{33} \ldots(40)
$$

$$
\mathrm{k}_{ads,at\text{k-}e_f^-} = \mathrm{k}_{42} \mathrm{K}_9 C_{S_{ox}} \mathrm{K}_{13} C_{Site} a_s^2 + \mathrm{k}_{43} \mathrm{K}_{13} C_{Site} a_s + \mathrm{k}_{44} \mathrm{K}_9 C_{S_{ox}} a_s + \mathrm{k}_{45} \ldots(41)
$$

$$
\mathrm{k}_{ads,at\text{k-}O_2^-\cdot} = \mathrm{k}_{46} \mathrm{K}_{10} C_{S_{ox}} \mathrm{K}_{13} C_{Site} a_s^2 + \mathrm{k}_{47} \mathrm{K}_{13} C_{Site} a_s + \mathrm{k}_{48} \mathrm{K}_{10} C_{S_{ox}} a_s + \mathrm{k}_{49} \ldots(42)
$$

$$
\mathrm{k}_{ads,at\text{k-}\chi^-\cdot} = \mathrm{k}_{50} \mathrm{K}_{12} C_{S_{ox}} \mathrm{K}_{13} C_{Site} a_s^2 + \mathrm{k}_{51} \mathrm{K}_{13} C_{Site} a_s + \mathrm{k}_{52} \mathrm{K}_{12} C_{S_{ox}} a_s + \mathrm{k}_{53} \ldots(43)
$$

Substituting equations (38 – 43) into equation (37) we have:

$$
\begin{aligned}
-r_P = {} & \mathrm{k}_{ads,at\text{k-}h_f^+} C_{h_f^+} C_{R_i} + \mathrm{k}_{ads,at\text{k-}OH\cdot} C_{OH\cdot} C_{R_i} + \mathrm{k}_{ads,at\text{k-}\chi^+\cdot} C_{\chi^+\cdot} C_{R_i} \\
& + \mathrm{k}_{ads,at\text{k-}e_f^-} C_{e_f^-} C_{R_i} + \mathrm{k}_{ads,at\text{k-}O_2^-\cdot} C_{O_2^-\cdot} C_{R_i} + \mathrm{k}_{ads,at\text{k-}\chi^-\cdot} C_{\chi^-\cdot} C_{R_i}
\end{aligned} \quad \ldots(44)
$$

To obtain $OH\cdot, O_2^-\cdot, \chi^+\cdot \,\&\, \chi^-\cdot$ concentrations, a steady-state approximation can be applied:

$$
\begin{aligned}
r_{OH\cdot} = {} & \mathrm{k}_{14^+} C_{S_{ox}-OH^-} \mathrm{K}_7 C_{h_f^+} C_{S_{ox}} a_S{}^2 - \mathrm{k}_{14^-} \mathrm{K}_8 C_{OH\cdot} C_{S_{ox}} C_{S_{ox}} a_S{}^2 + \mathrm{k}_{15^+} C_{S_{ox}-OH^-} C_{h_f^+} a_S - \mathrm{k}_{15^-} \mathrm{K}_8 C_{OH\cdot} C_{S_{ox}} a_S \\
& + \mathrm{k}_{16^+} C_{OH^-} \mathrm{K}_7 C_{h_f^+} C_{S_{ox}} a_S - \mathrm{k}_{16^-} C_{OH\cdot} C_{S_{ox}} a_S + \mathrm{k}_{17^+} C_{OH^-} C_{h_f^+} - \mathrm{k}_{17^-} C_{OH\cdot} - \mathrm{k}_{ads,at\text{k-}OH\cdot} C_{OH\cdot} C_{R_i}
\end{aligned} \quad \ldots(45)
$$

$$
\begin{aligned}
r_{\chi^+\cdot} = {} & \mathrm{k}_{18^+} \mathrm{K}_6 C_\chi C_{S_{ox}} \mathrm{K}_7 C_{h_f^+} C_{S_{ox}} a_S{}^2 - \mathrm{k}_{18^-} \mathrm{K}_{11} C_{\chi^+\cdot} C_{S_{ox}} C_{S_{ox}} a_S{}^2 + \mathrm{k}_{19^+} \mathrm{K}_6 C_\chi C_{S_{ox}} C_{h_f^+} a_S - \mathrm{k}_{19^-} \mathrm{K}_{11} C_{\chi^+\cdot} C_{S_{ox}} a_S \\
& + \mathrm{k}_{20^+} C_\chi \mathrm{K}_7 C_{h_f^+} C_{S_{ox}} a_S - \mathrm{k}_{20^-} C_{\chi^+\cdot} C_{S_{ox}} a_S + \mathrm{k}_{21^+} C_\chi C_{h_f^+} - \mathrm{k}_{21^-} C_{\chi^+\cdot} - \mathrm{k}_{ads,at\text{k-}\chi^+\cdot} C_{\chi^+\cdot} C_{R_i}
\end{aligned} \quad \ldots(46)
$$

$$
\begin{aligned}
r_{O_2^-\cdot} = {} & \mathrm{k}_{34^+} \mathrm{K}_5 C_{O_2} C_{S_{ox}} \mathrm{K}_9 C_{e_f^-} C_{S_{ox}} a_S{}^2 - \mathrm{k}_{34^-} \mathrm{K}_{10} C_{O_2^-\cdot} C_{S_{ox}} C_{S_{ox}} a_S{}^2 + \mathrm{k}_{35^+} \mathrm{K}_5 C_{O_2} C_{S_{ox}} C_{e_f^-} a_S - \mathrm{k}_{35^-} \mathrm{K}_{10} C_{O_2^-\cdot} C_{S_{ox}} a_S \\
& + \mathrm{k}_{36^+} C_{O_2} \mathrm{K}_9 C_{e_f^-} C_{S_{ox}} a_S - \mathrm{k}_{36^-} C_{O_2^-\cdot} C_{S_{ox}} a_S + \mathrm{k}_{37^+} C_{O_2} C_{e_f^-} - \mathrm{k}_{37^-} C_{O_2^-\cdot} - \mathrm{k}_{ads,at\text{k-}O_2^-\cdot} C_{O_2^-\cdot} C_{R_i}
\end{aligned} \quad \ldots(47)
$$

$$r_{\chi^{-}\cdot} = \mathrm{k}_{38^{+}}\mathrm{K}_6 C_{\chi} C_{S_{ox}} \mathrm{K}_9 C_{e_f^{-}} C_{S_{ox}} a_S{}^2 - \mathrm{k}_{38^{-}}\mathrm{K}_{11} C_{\chi^{-}\cdot} C_{S_{ox}} C_{S_{ox}} a_S{}^2 + \mathrm{k}_{39^{+}}\mathrm{K}_6 C_{\chi} C_{S_{ox}} C_{e_f^{-}} a_S - \mathrm{k}_{39^{-}}\mathrm{K}_{11} C_{\chi^{-}\cdot} C_{S_{ox}} a_S$$
$$+\mathrm{k}_{40^{+}} C_{\chi} \mathrm{K}_9 C_{e_f^{-}} C_{S_{ox}} a_S - \mathrm{k}_{40^{-}} C_{\chi^{-}\cdot} C_{S_{ox}} a_S + \mathrm{k}_{41^{+}} C_{\chi} C_{e_f^{-}} - \mathrm{k}_{41^{-}} C_{\chi^{-}\cdot} - \mathrm{k}_{ads,atk\text{-}\chi^{-}\cdot} C_{\chi^{-}\cdot} C_{R_i} \quad \ldots(48)$$

In equation (45), $C_{OH^{-}}$ & $C_{S_{ox}-OH^{-}}$ represents the adjacent film and superficial concentration of $OH^{-}$ or water. This is the species that it is assumed to react with the holes. In wastewater systems, Turchi and Ollis [89] assumed that this concentration may be constant. Hence,

$$\begin{aligned} \mathrm{k}'_{14^{+}} &= \mathrm{k}_{14^{+}} C_{S_{ox}-OH^{-}} \\ \mathrm{k}'_{15^{+}} &= \mathrm{k}_{15^{+}} C_{S_{ox}-OH^{-}} \\ \mathrm{k}'_{15^{+}} &= \mathrm{k}_{15^{+}} C_{OH^{-}} \\ \mathrm{k}'_{16^{+}} &= \mathrm{k}_{16^{+}} C_{OH^{-}} \end{aligned} \quad \ldots(49)$$

Substituting equation (49) and subtracting the reactive radical species concentration, it gives:

.

$$r_{OH\cdot} = C_{h_f^{+}} \left[ \mathrm{k}'_{14^{+}} \mathrm{K}_7 C_{S_{ox}} a_S{}^2 + \mathrm{k}'_{16^{+}} \mathrm{K}_7 C_{S_{ox}} a_S + \mathrm{k}'_{15^{+}} a_S + \mathrm{k}'_{17^{+}} \right]$$
$$-C_{OH\cdot} \left[ \mathrm{k}_{14^{-}} \mathrm{K}_8 C_{S_{ox}} C_{S_{ox}} a_S{}^2 + \mathrm{k}_{15^{-}} \mathrm{K}_8 C_{S_{ox}} a_S + \mathrm{k}_{16^{-}} C_{S_{ox}} a_S - \mathrm{k}_{17^{-}} + \mathrm{k}_{ads,atk\text{-}OH\cdot} C_{R_i} \right] = 0 \quad \ldots(50)$$
$$C_{OH\cdot} = \frac{C_{h_f^{+}} \left[ \mathrm{k}'_{14^{+}} \mathrm{K}_7 C_{S_{ox}} a_S{}^2 + \mathrm{k}'_{16^{+}} \mathrm{K}_7 C_{S_{ox}} a_S + \mathrm{k}'_{15^{+}} a_S + \mathrm{k}'_{17^{+}} \right]}{\mathrm{k}_{14^{-}} \mathrm{K}_8 C_{S_{ox}} C_{S_{ox}} a_S{}^2 + \mathrm{k}_{15^{-}} \mathrm{K}_8 C_{S_{ox}} a_S + \mathrm{k}_{16^{-}} C_{S_{ox}} a_S + \mathrm{k}_{17^{-}} + \mathrm{k}_{ads,atk\text{-}OH\cdot} C_{R_i}}$$

$$r_{\chi^{+}\cdot} = C_{h_f^{+}} C_{\chi} \left[ \mathrm{k}_{18^{+}} \mathrm{K}_6 C_{S_{ox}} \mathrm{K}_7 C_{S_{ox}} a_S{}^2 + \mathrm{k}_{19^{+}} \mathrm{K}_6 C_{S_{ox}} a_S + \mathrm{k}_{20^{+}} \mathrm{K}_7 C_{S_{ox}} a_S + \mathrm{k}_{21^{+}} \right]$$
$$-C_{\chi^{+}\cdot} \left[ \mathrm{k}_{18^{-}} \mathrm{K}_{11} C_{S_{ox}} C_{S_{ox}} a_S{}^2 + \mathrm{k}_{19^{-}} \mathrm{K}_{11} C_{S_{ox}} a_S + \mathrm{k}_{20^{-}} C_{S_{ox}} a_S + \mathrm{k}_{21^{-}} + \mathrm{k}_{ads,atk\text{-}\chi^{+}\cdot} C_{R_i} \right] = 0 \quad \ldots(51)$$
$$C_{\chi^{+}\cdot} = \frac{C_{h_f^{+}} C_{\chi} \left[ \mathrm{k}_{18^{+}} \mathrm{K}_6 C_{S_{ox}} \mathrm{K}_7 C_{S_{ox}} a_S{}^2 + \mathrm{k}_{19^{+}} \mathrm{K}_6 C_{S_{ox}} a_S + \mathrm{k}_{20^{+}} \mathrm{K}_7 C_{S_{ox}} a_S + \mathrm{k}_{21^{+}} \right]}{\mathrm{k}_{18^{-}} \mathrm{K}_{11} C_{S_{ox}} C_{S_{ox}} a_S{}^2 + \mathrm{k}_{19^{-}} \mathrm{K}_{11} C_{S_{ox}} a_S + \mathrm{k}_{20^{-}} C_{S_{ox}} a_S + \mathrm{k}_{21^{-}} + \mathrm{k}_{ads,atk\text{-}\chi^{+}\cdot} C_{R_i}}$$

$$r_{O_2^{-}\cdot} = C_{e_f^{-}} C_{O_2} \left[ \mathrm{k}_{34^{+}} \mathrm{K}_5 C_{S_{ox}} \mathrm{K}_9 C_{S_{ox}} a_S{}^2 + \mathrm{k}_{35^{+}} \mathrm{K}_5 C_{S_{ox}} a_S + \mathrm{k}_{36^{+}} \mathrm{K}_9 C_{S_{ox}} a_S + \mathrm{k}_{37^{+}} \right]$$
$$-C_{O_2^{-}\cdot} \left[ \mathrm{k}_{34^{-}} \mathrm{K}_{10} C_{S_{ox}} C_{S_{ox}} a_S{}^2 + \mathrm{k}_{35^{-}} \mathrm{K}_{10} C_{S_{ox}} a_S + \mathrm{k}_{36^{-}} C_{S_{ox}} a_S + \mathrm{k}_{37^{-}} + \mathrm{k}_{ads,atk\text{-}O_2^{-}\cdot} C_{R_i} \right] = 0 \quad \ldots(52)$$
$$C_{O_2^{-}\cdot} = \frac{C_{e_f^{-}} C_{O_2} \left[ \mathrm{k}_{34^{+}} \mathrm{K}_5 C_{S_{ox}} \mathrm{K}_9 C_{S_{ox}} a_S{}^2 + \mathrm{k}_{35^{+}} \mathrm{K}_5 C_{S_{ox}} a_S + \mathrm{k}_{36^{+}} \mathrm{K}_9 C_{S_{ox}} a_S + \mathrm{k}_{37^{+}} \right]}{\mathrm{k}_{34^{-}} \mathrm{K}_{10} C_{S_{ox}} C_{S_{ox}} a_S{}^2 + \mathrm{k}_{35^{-}} \mathrm{K}_{10} C_{S_{ox}} a_S + \mathrm{k}_{36^{-}} C_{S_{ox}} a_S + \mathrm{k}_{37^{-}} + \mathrm{k}_{ads,atk\text{-}O_2^{-}\cdot} C_{R_i}}$$

$$r_{\chi^{-}\cdot} = C_{e_f^-} C_{\chi} \left[ \mathrm{k}_{38^+} \mathrm{K}_6 C_{S_{ox}} \mathrm{K}_9 C_{S_{ox}} a_S{}^2 + \mathrm{k}_{39^+} \mathrm{K}_6 C_{S_{ox}} a_S + \mathrm{k}_{40^+} \mathrm{K}_9 C_{S_{ox}} a_S + \mathrm{k}_{41^+} \right]$$

$$-C_{\chi^{-}\cdot} \left[ \mathrm{k}_{38^-} \mathrm{K}_{11} C_{S_{ox}} C_{S_{ox}} a_S{}^2 + \mathrm{k}_{39^-} \mathrm{K}_{11} C_{S_{ox}} a_S + \mathrm{k}_{40^-} C_{S_{ox}} a_S + \mathrm{k}_{41^-} + \mathrm{k}_{ads,at\text{-}\chi^{-}\cdot} C_{R_i} \right] = 0 \ldots(53)$$

$$C_{\chi^{-}\cdot} = \frac{C_{e_f^-} C_{\chi} \left[ \mathrm{k}_{38^+} \mathrm{K}_6 C_{S_{ox}} \mathrm{K}_9 C_{S_{ox}} a_S{}^2 + \mathrm{k}_{39^+} \mathrm{K}_6 C_{S_{ox}} a_S + \mathrm{k}_{40^+} \mathrm{K}_9 C_{S_{ox}} a_S + \mathrm{k}_{41^+} \right]}{\mathrm{k}_{38^-} \mathrm{K}_{11} C_{S_{ox}} C_{S_{ox}} a_S{}^2 + \mathrm{k}_{39^-} \mathrm{K}_{11} C_{S_{ox}} a_S + \mathrm{k}_{40^-} C_{S_{ox}} a_S + \mathrm{k}_{41^-} + \mathrm{k}_{ads,at\text{-}\chi^{-}\cdot} C_{R_i}}$$

Redefining constant values of equations (50 – 53):

$$\mathrm{k}_{ads,act-OH\cdot} = \mathrm{k'}_{14^+} \mathrm{K}_7 C_{S_{ox}} a_S{}^2 + \mathrm{k'}_{16^+} \mathrm{K}_7 C_{S_{ox}} a_S + \mathrm{k'}_{15^+} a_S + \mathrm{k'}_{17^+} \ldots(54)$$

$$\mathrm{k}_{ads,desact-OH\cdot} = \mathrm{k}_{14^-} \mathrm{K}_8 C_{S_{ox}} C_{S_{ox}} a_S{}^2 + \mathrm{k}_{15^-} \mathrm{K}_8 C_{S_{ox}} a_S + \mathrm{k}_{16^-} C_{S_{ox}} a_S + \mathrm{k}_{17^-} \ldots(55)$$

$$\mathrm{k}_{ads,act-\chi^{+}\cdot} = \mathrm{k}_{18^+} \mathrm{K}_6 C_{S_{ox}} \mathrm{K}_7 C_{S_{ox}} a_S{}^2 + \mathrm{k}_{19^+} \mathrm{K}_6 C_{S_{ox}} a_S + \mathrm{k}_{20^+} \mathrm{K}_7 C_{S_{ox}} a_S + \mathrm{k}_{21^+} \ldots(56)$$

$$\mathrm{k}_{ads,desact-\chi^{+}\cdot} = \mathrm{k}_{18^-} \mathrm{K}_{11} C_{S_{ox}} C_{S_{ox}} a_S{}^2 + \mathrm{k}_{19^-} \mathrm{K}_{11} C_{S_{ox}} a_S + \mathrm{k}_{20^-} C_{S_{ox}} a_S + \mathrm{k}_{21^-} \ldots(57)$$

$$\mathrm{k}_{ads,act-O_2^-\cdot} = \mathrm{k}_{34^+} \mathrm{K}_5 C_{S_{ox}} \mathrm{K}_9 C_{S_{ox}} a_S{}^2 + \mathrm{k}_{35^+} \mathrm{K}_5 C_{S_{ox}} a_S + \mathrm{k}_{36^+} \mathrm{K}_9 C_{S_{ox}} a_S + \mathrm{k}_{37^+} \ldots(58)$$

$$\mathrm{k}_{ads,desact-O_2^-\cdot} = \mathrm{k}_{34^-} \mathrm{K}_{10} C_{S_{ox}} C_{S_{ox}} a_S{}^2 + \mathrm{k}_{35^-} \mathrm{K}_{10} C_{S_{ox}} a_S + \mathrm{k}_{36^-} C_{S_{ox}} a_S + \mathrm{k}_{37^-} \ldots(59)$$

$$\mathrm{k}_{ads,act-\chi^{-}\cdot} = \mathrm{k}_{38^+} \mathrm{K}_6 C_{S_{ox}} \mathrm{K}_9 C_{S_{ox}} a_S{}^2 + \mathrm{k}_{39^+} \mathrm{K}_6 C_{S_{ox}} a_S + \mathrm{k}_{40^+} \mathrm{K}_9 C_{S_{ox}} a_S + \mathrm{k}_{41^+} \ldots(60)$$

$$\mathrm{k}_{ads,desact-\chi^{-}\cdot} = \mathrm{k}_{38^-} \mathrm{K}_{11} C_{S_{ox}} C_{S_{ox}} a_S{}^2 + \mathrm{k}_{39^-} \mathrm{K}_{11} C_{S_{ox}} a_S + \mathrm{k}_{40^-} C_{S_{ox}} a_S + \mathrm{k}_{41^-} \ldots(61)$$

Simplifying:

.

$$C_{OH\cdot} = \frac{C_{h_f^+} \mathrm{k}_{ads,act-OH\cdot}}{\mathrm{k}_{ads,desact-OH\cdot} + \mathrm{k}_{ads,at\text{-}OH\cdot} C_{R_i}} \ldots(62)$$

$$C_{\chi^{+}\cdot} = \frac{C_{h_f^+} C_{\chi} \mathrm{k}_{ads,act-\chi^{+}\cdot}}{\mathrm{k}_{ads,desact-\chi^{+}\cdot} + \mathrm{k}_{ads,at\text{-}\chi^{+}\cdot} C_{R_i}} \ldots(63)$$

$$C_{O_2^-\cdot} = \frac{\mathrm{k}_{ads,act-O_2^-\cdot} C_{e_f^-} C_{O_2}}{\mathrm{k}_{ads,desact-O_2^-\cdot} + \mathrm{k}_{ads,at\text{-}O_2^-\cdot} C_{R_i}} \ldots(64)$$

$$C_{\chi^{-}\cdot} = \frac{\mathrm{k}_{ads,act-\chi^{-}\cdot} C_{e_f^-} C_{\chi}}{\mathrm{k}_{ads,desact-\chi^{-}\cdot} + \mathrm{k}_{ads,at\text{-}\chi^{-}\cdot} C_{R_i}} \ldots(65)$$

Regrouping constant of equations (62 – 65):

$$\alpha_{OH\cdot} = \frac{\mathrm{k}_{ads,attack-OH\cdot}}{\mathrm{k}_{ads,desact-OH\cdot}} \ldots(66)$$

$$\alpha_{\chi^{+}\cdot} = \frac{\mathrm{k}_{ads,ark-\chi^{+}\cdot}}{\mathrm{k}_{ads,desact-\chi^{+}\cdot}} \ldots(67)$$

$$\alpha_{O_2^{-}\cdot} = \frac{\mathrm{k}_{ads,attack-O_2^{-}\cdot}}{\mathrm{k}_{ads,desact-O_2^{-}\cdot}} \ldots(68)$$

$$\alpha_{\chi^{-}\cdot} = \frac{\mathrm{k}_{ads,ark-\chi^{-}\cdot}}{\mathrm{k}_{ads,desact-\chi^{-}\cdot}} \ldots(69)$$

It is achieved:

$$C_{OH\cdot} = \frac{C_{h_f^{+}}\mathrm{k}_{ads,act-OH\cdot}}{\mathrm{k}_{ads,desact-OH\cdot}\left(1+\alpha_{OH\cdot}C_{R_i}\right)} \ldots(70)$$

$$C_{\chi^{+}\cdot} = \frac{C_{h_f^{+}}C_{\chi}\mathrm{k}_{ads,act-\chi^{+}\cdot}}{\mathrm{k}_{ads,desact-\chi^{+}\cdot}\left(1+\alpha_{\chi^{+}\cdot}C_{R_i}\right)} \ldots(71)$$

$$C_{O_2^{-}\cdot} = \frac{\mathrm{k}_{ads,act-O_2^{-}\cdot}C_{e_f^{-}}C_{O_2}}{\mathrm{k}_{ads,desact-O_2^{-}\cdot}\left(1+\alpha_{O_2^{-}\cdot}C_{R_i}\right)} \ldots(72)$$

$$C_{\chi^{-}\cdot} = \frac{\mathrm{k}_{ads,act-\chi^{-}\cdot}C_{e_f^{-}}C_{\chi}}{\mathrm{k}_{ads,desact-\chi^{-}\cdot}\left(1+\alpha_{\chi^{-}\cdot}C_{R_i}\right)} \ldots(73)$$

Rewriting equation (44):

$$-r_P = \left[ \mathrm{k}_{ads,atk\text{-}h_f^+} C_{R_i} + \mathrm{k}_{ads,act-OH\cdot} \frac{\alpha_{OH\cdot} C_{R_i}}{\left(1+\alpha_{OH\cdot} C_{R_i}\right)} + \mathrm{k}_{ads,act-\chi^+\cdot} C_\chi \frac{\alpha_{\chi^+\cdot} C_{R_i}}{\left(1+\alpha_{\chi^+\cdot} C_{R_i}\right)} \right] C_{h_f^+}$$
$$+ \left[ \mathrm{k}_{ads,atk\text{-}e_f^-} C_{R_i} + \mathrm{k}_{ads,act-O_2^-\cdot} C_{O_2} \frac{\alpha_{O_2^-\cdot} C_{R_i}}{\left(1+\alpha_{O_2^-\cdot} C_{R_i}\right)} + \mathrm{k}_{ads,act-\chi^-\cdot} C_\chi \frac{\alpha_{\chi^-\cdot} C_{R_i}}{\left(1+\alpha_{\chi^-\cdot} C_{R_i}\right)} \right] C_{e_f^-} \quad \ldots(74)$$

Some terms of equation (74) have a remembrance of the Langmuir-Hinshelwood kinetic model, as mentioned by Mueses *et al.* (2013). Therefore, defining *theta* (θ) values as follows:

$$\theta_{OH\cdot} = \frac{\alpha_{OH\cdot} C_{R_i}}{\left(1+\alpha_{OH\cdot} C_{R_i}\right)} \ldots(75)$$

$$\theta_{\chi^+\cdot} = \frac{\alpha_{\chi^+\cdot} C_{R_i}}{\left(1+\alpha_{\chi^+\cdot} C_{R_i}\right)} \ldots(76)$$

$$\theta_{O_2^-\cdot} = \frac{\alpha_{O_2^-\cdot} C_{R_i}}{\left(1+\alpha_{O_2^-\cdot} C_{R_i}\right)} \ldots(77)$$

$$\theta_{\chi^-\cdot} = \frac{\alpha_{\chi^-\cdot} C_{R_i}}{\left(1+\alpha_{\chi^-\cdot} C_{R_i}\right)} \ldots(78)$$

Hence, simplifying equation (74), it gives:

$$-r_P = \left[ \mathrm{k}_{ads,atk\text{-}h_f^+} C_{R_i} + \mathrm{k}_{ads,act-OH\cdot} \theta_{OH\cdot} + \mathrm{k}_{ads,act-\chi^+\cdot} C_\chi \theta_{\chi^+\cdot} \right] C_{h_f^+}$$
$$+ \left[ \mathrm{k}_{ads,atk\text{-}e_f^-} C_{R_i} + \mathrm{k}_{ads,act-O_2^-\cdot} C_{O_2} \theta_{O_2^-\cdot} + \mathrm{k}_{ads,act-\chi^-\cdot} C_\chi \theta_{\chi^-\cdot} \right] C_{e_f^-} \quad \ldots(79)$$

For the generation of the electron-hole pair, recombination must be considered as a reversible process. Therefore, through interfacial charge transfer, electron-hole pair present a relaxation to the reactive surface states. Once more, the steady-state approximation may be used to obtain the hole and electron concentration:

$$\mathrm{r}_{h^+} = \mathrm{R}_g - \mathrm{k}^- C_{h^+} C_{e^-} v_P \cong 0 \ldots(80)$$

$$C_{h^+}C_{e^-} = \frac{R_g}{\mathrm{k}_R^- v_P} \ldots(81)$$

$$\mathrm{r}_{h_f^+} = \mathrm{k}_{IT}(T)C_{h^+}C_{e^-}v_P - \mathrm{k}_{ads,act-OH\cdot}C_{h_f^+} - \mathrm{k}_{ads,attack-h_f^+}C_{h_f^+}C_{R_i} - \mathrm{k}_{ads,act-\chi^+\cdot}C_{h_f^+} - \mathrm{k}_{54}v_P C_{h_f^+}C_{e_f^-} \cong 0 \ldots(82)$$

Substituting equation (81) on equation (82), the following equation is obtained:

$$\mathrm{r}_{h_f^+} = \frac{\mathrm{k}_{IT}(T)}{\mathrm{k}_R^-}R_g - \mathrm{k}_{ads,act-OH\cdot}C_{h_f^+} - \mathrm{k}_{ads,attack-h_f^+}C_{h_f^+}C_{R_i} - \mathrm{k}_{ads,act-\chi^+\cdot}C_{h_f^+} - \mathrm{k}_{54}v_P C_{h_f^+}{}^2 \cong 0 \ldots(83)$$

Reorganizing equation (83):

$$\mathrm{k}_{54}v_P C_{h_f^+}{}^2 + \left[\mathrm{k}_{ads,act-OH\cdot} + \mathrm{k}_{ads,attack-h_f^+}C_{R_i} + \mathrm{k}_{ads,act-\chi^+\cdot}\right]C_{h_f^+} - \frac{\mathrm{k}_{IT}(T)}{\mathrm{k}_R^-}R_g \cong 0 \ldots(84)$$

Solving the quadratic equation (84) for the concentration of holes, it is obtained:

$$C_{h_f^+} = \frac{-\left[\mathrm{k}_{ads,act-OH\cdot} + \mathrm{k}_{ads,attack-h_f^+}C_{R_i} + \mathrm{k}_{ads,act-\chi^+\cdot}\right] + \sqrt{\left[\mathrm{k}_{ads,act-OH\cdot} + \mathrm{k}_{ads,attack-h_f^+}C_{R_i} + \mathrm{k}_{ads,act-\chi^+\cdot}\right]^2 + 4\mathrm{k}_{54}v_P\frac{\mathrm{k}_{IT}(T)}{\mathrm{k}_R^-}R_g}}{2\mathrm{k}_{54}v_P}$$

…(85)

Reorganizing equation (85):

$$C_{h_f^+} = \frac{\left[\mathrm{k}_{ads,act-OH\cdot} + \mathrm{k}_{ads,attack-h_f^+}C_{R_i} + \mathrm{k}_{ads,act-\chi^+\cdot}\right]\left[-1 + \sqrt{1 + \frac{4\mathrm{k}_{54}v_P\mathrm{K}_{IT}(T)R_g}{\left[\mathrm{k}_{ads,act-OH\cdot} + \mathrm{k}_{ads,attack-h_f^+}C_{R_i} + \mathrm{k}_{ads,act-\chi^+\cdot}\right]^2}}\right]}{2\mathrm{k}_{54}v_P} \ldots(86)$$

The mathematical expression solved for the concentration of holes is similar for electrons:

$$C_{e_f^-} = \frac{\left[\mathrm{k}_{ads,act-O_2^-\cdot} + \mathrm{k}_{ads,attack-e_f^-}C_{R_i} + \mathrm{k}_{ads,act-\chi^-\cdot}\right]\left[-1 + \sqrt{1 + \frac{4\mathrm{k}_{54}v_{PIT}\mathrm{K}_{IT}(T)R_g}{\left[\mathrm{k}_{ads,act-O_2^-\cdot} + \mathrm{k}_{ads,attack-e_f^-}C_{R_i} + \mathrm{k}_{ads,act-\chi^-\cdot}\right]^2}}\right]}{2\mathrm{k}_{54}v_P} \ldots(87)$$

Here $R_g$, is the rate of electron-hole generation per particle $r_g[=]mol\ s^{-1}\ particle^{-1}$.

Combining the equations (67), (73) and (74) result in the global mathematical expression for the photocatalytic degradation processes. However, for the practical application, the mathematical expression results in a complicated numerical solution. Nevertheless, as it is established for the effective photocatalytic mechanism, different pathways for the degradation of organic pollutants could be settled:

*Electron-hole pair*

$$-r_P = \mathrm{k}_{ads,atk\text{-}h_f^+} C_{R_i} C_{h_f^+} \ldots(88)$$

$$-r_P = \mathrm{k}_{ads,atk\text{-}e_f^-} C_{R_i} C_{e_f^-} \ldots(89)$$

$$C_{h_f^+} = \frac{\mathrm{k}_{ads,attack-h_f^+} C_{R_i} \left[ -1 + \sqrt{1 + \frac{4\mathrm{k}_{54} v_P \mathrm{K}_{IT}(T) R_g}{\left[ \mathrm{k}_{ads,attack-h_f^+} C_{R_i} \right]^2}} \right]}{2\mathrm{k}_{54} v_P} \ldots(90)$$

$$C_{e_f^-} = \frac{\mathrm{k}_{ads,attack-e_f^-} C_{R_i} \left[ -1 + \sqrt{1 + \frac{4\mathrm{k}_{54} v_P \mathrm{K}_{IT}(T) R_g}{\left[ \mathrm{k}_{ads,attack-e_f^-} C_{R_i} \right]^2}} \right]}{2\mathrm{k}_{54} v_P} \ldots(91)$$

The restriction of electroneutrality on a catalyst particle maintains that one $e^-$ must react for each $h^+$ reacted. This means that $C_{e^-} = C_{h^+}$. This restriction was validated as deduced above. Therefore:

$$-r_P = \frac{\mathrm{k}_{ads,attack-h_f^+}{}^2 C_{R_i}{}^2}{2\mathrm{k}_{54} v_P} \left[ -1 + \sqrt{1 + \frac{4\mathrm{k}_{54} v_P \mathrm{K}_{IT}(T) R_g}{\mathrm{k}_{ads,attack-h_f^+}{}^2 C_{R_i}{}^2}} \right] \ldots(92)$$

$$-r_P = \frac{\mathrm{k}_{ads,attack-e_f^-}{}^2 C_{R_i}{}^2}{2\mathrm{k}_{54} v_P} \left[ -1 + \sqrt{1 + \frac{4\mathrm{k}_{54} v_P \mathrm{K}_{IT}(T) R_g}{\mathrm{k}_{ads,attack-e_f^-}{}^2 C_{R_i}{}^2}} \right] \ldots(93)$$

$$\alpha_{h_f^+} = \frac{\mathrm{k}_{ads,attack-h_f^+}{}^2}{2\mathrm{k}_{54} v_P} \ldots(94)$$

$$\alpha_{e_f^-} = \frac{\mathrm{k}_{ads,attack-e_f^-}{}^2}{2\mathrm{k}_{54} v_P} \ldots(95)$$

$$-r_P = \alpha_{h_f^+}\left[-1+\sqrt{1+\frac{2\mathrm{K}_{IT}(T)R_g}{\alpha_{h_f^+}C_{R_i}{}^2}}\right]C_{R_i}{}^2 \ldots(96)$$

$$-r_P = \alpha_{e_f^-}\left[-1+\sqrt{1+\frac{2\mathrm{K}_{IT}(T)R_g}{\alpha_{e_f^-}C_{R_i}{}^2}}\right]C_{R_i}{}^2 \ldots(97)$$

$$-r_P = \alpha_{h^+-e^-}\left[-1+\sqrt{1+\frac{2\mathrm{K}_{IT}(T)R_g}{\alpha_{h^+-e^-}C_{R_i}{}^2}}\right]C_{R_i}{}^2 \ldots(98)$$

Considering the particle properties by $\kappa_P$:

$$-r_{R_i} = 2\frac{\alpha_{h^+-e^-}}{\kappa_P}\left[-1+\sqrt{1+\frac{\kappa_P}{\alpha_{h^+-e^-}}\frac{\mathrm{K}_{IT}(T)R_g}{C_{R_i}{}^2}}\right]C_{R_i}{}^2 \ldots(99)$$

With

$$\kappa_P = S_g C_{Cat} \ldots(100)$$

$$\alpha_{h^+-e^-}[=]\frac{m\cdot L}{mg\cdot h}$$

*Reactive radical species*

For the attack via radical species, four principal cases can be developed from the equation (79):

$$-r_P = \mathrm{k}_{ads,act-OH\cdot}\theta_{OH\cdot}C_{h_f^+} \ldots(101)$$

$$-r_P = \mathrm{k}_{ads,act-\chi^+\cdot}C_\chi\theta_{\chi^+\cdot}C_{h_f^+} \ldots(102)$$

$$-r_P = \mathrm{k}_{ads,act-O_2^-\cdot}C_{O_2}\theta_{O_2^-\cdot}C_{e_f^-} \ldots(103)$$

$$-r_P = \mathrm{k}_{ads,act-\chi^-\cdot}C_\chi\theta_{\chi^-\cdot}C_{e_f^-} \ldots(104)$$

$$C_{h_f^+} = \frac{\mathrm{k}_{ads,act-OH\cdot}}{2\mathrm{k}_{54}v_P}\left[-1+\sqrt{1+\frac{4\mathrm{k}_{54}v_P\mathrm{K}_{IT}(T)R_g}{\mathrm{k}_{ads,act-OH\cdot}{}^2}}\right]\ldots(105)$$

$$C_{h_f^+} = \frac{\mathrm{k}_{ads,act-\chi^+\cdot}}{2\mathrm{k}_{54}v_P}\left[-1+\sqrt{1+\frac{4\mathrm{k}_{54}v_P\mathrm{K}_{IT}(T)R_g}{\mathrm{k}_{ads,act-\chi^+\cdot}^{\ 2}}}\right] \ldots(106)$$

$$C_{e_f^-} = \frac{\mathrm{k}_{ads,act-O_2^-\cdot}}{2\mathrm{k}_{54}v_P}\left[-1+\sqrt{1+\frac{4\mathrm{k}_{54}v_P\mathrm{K}_{IT}(T)R_g}{\mathrm{k}_{ads,act-O_2^-\cdot}^{\ 2}}}\right] \ldots(107)$$

$$C_{e_f^-} = \frac{\mathrm{k}_{ads,act-\chi^-\cdot}}{2\mathrm{k}_{54}v_P}\left[-1+\sqrt{1+\frac{4\mathrm{k}_{54}v_P\mathrm{K}_{IT}(T)R_g}{\mathrm{k}_{ads,act-\chi^-\cdot}^{\ 2}}}\right] \ldots(108)$$

$$-r_P = \frac{\mathrm{k}_{ads,act-OH\cdot}^{\ 2}}{2\mathrm{k}_{54}v_P}\left[-1+\sqrt{1+\frac{4\mathrm{k}_{54}v_P\mathrm{K}_{IT}(T)R_g}{\mathrm{k}_{ads,act-OH\cdot}^{\ 2}}}\right]\theta_{OH\cdot} \ldots(109)$$

$$-r_P = \frac{\mathrm{k}_{ads,act-\chi^+\cdot}^{\ 2}}{2\mathrm{k}_{54}v_P}\left[-1+\sqrt{1+\frac{4\mathrm{k}_{54}v_P\mathrm{K}_{IT}(T)R_g}{\mathrm{k}_{ads,act-\chi^+\cdot}^{\ 2}}}\right]C_\chi\theta_{\chi^+\cdot} \ldots(110)$$

$$-r_P = \frac{\mathrm{k}_{ads,act-O_2^-\cdot}^{\ 2}}{2\mathrm{k}_{54}v_P}\left[-1+\sqrt{1+\frac{4\mathrm{k}_{54}v_P\mathrm{K}_{IT}(T)R_g}{\mathrm{k}_{ads,act-O_2^-\cdot}^{\ 2}}}\right]C_{O_2}\theta_{O_2^-\cdot} \ldots(111)$$

$$-r_P = \frac{\mathrm{k}_{ads,act-\chi^-\cdot}^{\ 2}}{2\mathrm{k}_{54}v_P}\left[-1+\sqrt{1+\frac{4\mathrm{k}_{54}v_P\mathrm{K}_{IT}(T)R_g}{\mathrm{k}_{ads,act-\chi^-\cdot}^{\ 2}}}\right]C_\chi\theta_{\chi^-\cdot} \ldots(112)$$

Regrouping constants:

$$\mathrm{k}_{OH\cdot} = \frac{\mathrm{k}_{ads,act-OH\cdot}^{\ 2}}{2\mathrm{k}_{54}v_P} \ldots(113)$$

$$\mathrm{k}_{\chi^+\cdot} = \frac{\mathrm{k}_{ads,act-\chi^+\cdot}^{\ 2}}{2\mathrm{k}_{54}v_P} \ldots(114)$$

$$\mathrm{k}_{O_2^-\cdot} = \frac{\mathrm{k}_{ads,act-O_2^-\cdot}^{\ 2}}{2\mathrm{k}_{54}v_P} \ldots(115)$$

$$\mathrm{k}_{\chi^-\cdot} = \frac{\mathrm{k}_{ads,act-\chi^-\cdot}^{\ 2}}{2\mathrm{k}_{54}v_P} \ldots(116)$$

Then:

$$-r_P = \mathrm{k}_{OH\cdot}\left[-1+\sqrt{1+\frac{2\mathrm{K}_{IT}(T)R_g}{\mathrm{k}_{OH\cdot}}}\right]\theta_{OH\cdot} \ldots(117)$$

$$-r_P = \mathrm{k}_{\chi^+\cdot}\left[-1+\sqrt{1+\frac{2\mathrm{K}_{IT}(T)R_g}{\mathrm{k}_{\chi^+\cdot}}}\right]C_\chi\theta_{\chi^+\cdot} \ldots(118)$$

$$-r_P = \mathrm{k}_{O_2^-\cdot}\left[-1+\sqrt{1+\frac{2\mathrm{K}_{IT}(T)R_g}{\mathrm{k}_{O_2^-\cdot}}}\right]C_{O_2}\theta_{O_2^-\cdot} \ldots(119)$$

$$-r_P = \mathrm{k}_{\chi^-\cdot}\left[-1+\sqrt{1+\frac{2\mathrm{K}_{IT}(T)R_g}{\mathrm{k}_{\chi^-\cdot}}}\right]C_\chi\theta_{\chi^-\cdot} \ldots(120)$$

Considering the particle properties as above mentioned:

$$-r_{R_i} = 2\frac{\mathrm{k}_{OH\cdot}}{\kappa_P}\left[-1+\sqrt{1+\frac{\kappa_P}{\mathrm{k}_{OH\cdot}}\mathrm{K}_{IT}(T)R_g}\right]\theta_{OH\cdot} \ldots(121)$$

$$-r_{R_i} = 2\frac{\mathrm{k}_{\chi^+\cdot}}{\kappa_P}\left[-1+\sqrt{1+\frac{\kappa_P}{\mathrm{k}_{\chi^+\cdot}}\mathrm{K}_{IT}(T)R_g}\right]C_\chi\theta_{\chi^+\cdot} \ldots(122)$$

$$-r_{R_i} = 2\frac{\mathrm{k}_{O_2^-\cdot}}{\kappa_P}\left[-1+\sqrt{1+\frac{\kappa_P}{\mathrm{k}_{O_2^-\cdot}}\mathrm{K}_{IT}(T)R_g}\right]C_{O_2}\theta_{O_2^-\cdot} \ldots(123)$$

$$-r_{R_i} = 2\frac{\mathrm{k}_{\chi^-\cdot}}{\kappa_P}\left[-1+\sqrt{1+\frac{\kappa_P}{\mathrm{k}_{\chi^-\cdot}}\mathrm{K}_{IT}(T)R_g}\right]C_\chi\theta_{\chi^-\cdot} \ldots(124)$$

## *3.3. Six flux model with Henyey-Greenstein phase function*

For evaluating the overall volumetric rate of photon absorption ( $\hat{E}^a_{g(\lambda-\lambda')}$), the SFM-HG was employed. The local volumetric rate of photon absorption (LVRPA) divided by the incident radiation flux at a point x in the photoreactor calculated with SFM for a plane geometry is:

$$\frac{LVRPA}{I_0} = \frac{1}{\lambda_{\omega_{corr}}\omega_{corr}(1-\gamma)}\left[\omega_{corr}-1+\sqrt{1-\omega_{corr}^2}\,e^{\frac{-x}{\lambda_{\omega_{corr}}}}+\gamma\left(\omega_{corr}-1-\sqrt{1-\omega_{corr}^2}\,e^{\frac{x}{\lambda_{\omega_{corr}}}}\right)\right] \ldots(125)$$

Where $a$, $b$, $\omega_{corr}$ and $\gamma$ are SFM parameters defined as follows:

$$a = 1 - \omega p_f - \frac{4\omega^2 p_s^2}{1 - \omega p_f - \omega p_b - 2\omega p_s} \ldots(126)$$

$$b = \omega p_b + \frac{4\omega^2 p_s^2}{1 - \omega p_f - \omega p_b - 2\omega p_s} \ldots(127)$$

$$\omega_{corr} = \frac{b}{a} \ldots(128)$$

$$\lambda_{\omega_{corr}} = \frac{1}{a\beta\sqrt{1 - \omega_{corr}^2}} \ldots(129)$$

$$\gamma = \frac{1 - \sqrt{1 - \omega_{corr}^2}}{1 + \sqrt{1 - \omega_{corr}^2}} e^{-2\tau_{app}} \ldots(130)$$

Where the apparent optical thickness $\tau_{app}$ is:

$$\tau_{app} = a\tau\sqrt{1 - \omega_{corr}^2} \ldots(131)$$

The above SFM parameters are computed exclusively from the photocatalyst scattering albedo, reactor optical thickness, and the scattering phase function. The scattering albedo is defined as:

$$\omega = \frac{\sigma}{\beta} = \frac{\sigma}{\sigma + \kappa} \ldots(132)$$

Where $\beta$, $\kappa$ and $\sigma$ are the photocatalyst specific extinction, absorption and scattering coefficients. The optical thickness is given by:

$$\tau = L\beta C_{cat} \ldots (96)$$

With $L$ and $C_{cat}$ are the reactor length and catalyst load, respectively. The scattering phase function is specified in the SFM by the scattering probabilities: forward "$p_f$", backward "$p_b$" and sideward "$p_s$". They must satisfy the SFM main principle, from their definition of probabilities:

$$p_f + p_b + 4p_s = 1 \ldots(133)$$

Acosta-Herazo *et al.* (2016) coupled SFM to Henyey-Greenstein phase function, resulting in a mathematical expression of SFM as a function of the probabilities related to asymmetry factor " $g$ " [54]. The Montecarlo approach was employed and the fitting parameters within the SFG-HG equation develop a mathematical relationship of the probabilities with the asymmetry factor as follows:" [54]. The Montecarlo approach was employed and the fitting parameters within the SFG-HG equation develop a mathematical relationship of the probabilities with the asymmetry factor as follows:

$$p_f = 0.4467g + 0.5193 \ldots (98)$$

$$p_b = \begin{cases} -0.4691g + 0.3805 & -1 \le g \le 0.8 \\ 0 & g > 0.8 \end{cases} \ldots (134)$$

$$p_s = \frac{1}{4}\left(1 - p_f - p_b\right) \ldots (100)$$

The resulting mathematical expression of the SFM-HG is a function of the optical properties of the material, the catalyst load, the length of the reactor and the phase function that can be defined as isotropic scattering, specular anisotropy, and diffuse anisotropy, as a function of the asymmetry factor.

## *3.4. Extension of the effective quantum yield model*

A maximum probability function for the absorption of radiation is defined as the ratio of the specific absorption coefficient and extinction coefficient, both of which are intrinsic properties of the semiconductor:

$$P_{\varphi}^{a} \equiv \frac{\kappa_{\lambda}\left(\lambda \to \lambda^{'}\right)}{\beta_{\lambda}\left(\lambda \to \lambda^{'}\right)} \ldots (135)$$

Where the interval $\left(\lambda \to \lambda^{'}\right)$ corresponds to the absorption spectrum of the catalyst. It is important to note that equation (101) is also equivalent to $1-\omega$.

For optimal conditions of irradiation, the maximum quantum yield can be expressed as follows:

$$\phi_{g,\max}^{Eff} = \phi_g^{id} P_\varphi^a \ldots(136)$$

Where $\phi_g^{id}$ is the ideal value of the quantum yield, that corresponds to the maximum generation of the electron-hole pair and zero charge recombination. The effective value of $\phi_{g,\max}^{Eff}$ is a constant value associated with the intrinsic nature of the catalyst.

Since the observed quantum yields $\phi_g^{Eff}$ vary with the experimental conditions such as substrate type, pH, radiation field, catalyst load, and reactor geometry, the effects of these operational parameters can be decoupled from $\phi_g^{Eff}$ by introducing a new function $\Psi$, which takes into account these effects:

$$\Psi = \delta^{'} A_\Phi \ldots(137)$$

$$A_\Phi = f\left(\psi_E\right) e^{-\xi_\Phi} \ldots(138)$$

$$\xi_\Phi = -p\left(\mathrm{k}_{ads}\right) S_g \frac{C_{Cat}}{\rho_{Cat}} \left(\frac{C_{O_2}}{C_{i,0}}\right) \left(\frac{pH_{solution}}{zpc_{Cat}}\right) \ldots(139)$$

where $\rho_{Cat}$, $C_{Cat}$ and $zpc_{Cat}$ are the density, concentration and the point of zero charge of the catalyst, respectively, $p\left(\mathrm{k}_{ads}\right)$ is a probability function of the molecular adsorption for the i$^{th}$ component in equilibrium per unit of molecular weight, $pH_{solution}$ is the initial pH for the reaction, $C_{i,0}$ is the initial substrate concentration, $C_{O_2}$ is the dissolved oxygen concentration and $\delta^{'}$ is the Kronecker delta function. It is important to notice that the probability function developed by Mueses *et al*. (2013) can be estimated experimentally by adsorption equilibrium assessment [22]. Therefore, the term $p\left(\mathrm{k}_{ads}\right)$ can be changed for $f\left(\mathrm{k}_{ads}\right)$ and it can be calculated as follows:

$$\xi_\Phi = -f\left(\mathrm{k}_{ads}\right) S_g \frac{C_{Cat}}{\rho_{Cat}} \left(\frac{C_{O_2}}{C_{i,0}}\right) \left(\frac{pH_{solution}}{zpc_{Cat}}\right) \ldots(140)$$

$$f\left(\mathrm{k}_{ads}\right)=\frac{C_{Cat}Q_e}{C_{i,0}} \ldots(141)$$

Moreover, the relation of the volumetric rate of photon absorption at different catalyst dosage and at the reactor wall exposed to the incident radiation can be estimated as follows:

$$\psi_E=\frac{\hat{E}^a_{g(\lambda-\lambda')}}{\hat{E}^a_{g(\lambda-\lambda'),0}} \ldots(142)$$

For solar photocatalysis with titanium dioxide, Mueses *et al.* (2013) employed the absorption wavelength range of the $TiO_2$ and the UV zone of the power spectrum of the sun for further estimation of the quantum yield [61]. Thereby, the value of $\psi_E$ represents the spectral power distribution of the irradiation source. Nevertheless, as observed in Figure 3, the wavelength range of the light of emission may differ on intensity. This issue generates a mathematical inconsistency with the application of artificial light (*i.e.* LED). For this reason, the quantum estimation must be carried out by splitting the wavelength range spectrum into different zones and to simulate the quantum yield separately ($\phi^{Eff}_{g\ (\lambda\rightarrow\lambda')}$). Once the quantum yield for each zone was estimated, the procedure proposed by Mueses et al. (2013) can be employed as reported for solar photocatalysis. A detailed discussion of the quantum yield calculation will be present in section 5.7.

# 4. Methodology

## *4.1. Materials and reagents*

Zinc oxide employed for the modification of phenol-formaldehyde resins was obtained from a local industry (Zinc Nacional corporation) located in Monterrey, Nuevo León, México. Nitrogen gas, for the anaerobic conditions on the scavenger tests, was obtained from AOC (80% purity). Oxalic acid, sodium bicarbonate, and tetrahydrofuran were obtained from J.T. Baker. Anthraquinone 2 sulfonate, ascorbic acid, sodium pyruvate, and hexamethylenetetramine were procured from Sigma Aldrich (Analytical grade). Phenol (99%), formaldehyde (37%), hydrochloric acid (37%), acetone (80%) and ethanol (96%) were obtained from Desarrollo de Especialidades Químicas. Phenol (99%), formaldehyde (37%), hydrochloric acid (37%), acetone (80%) and ethanol (96%) were obtained from Desarrollo de Especialidades Químicas (DEQ). Sani-Pak® and blue wastewater sample were obtained from the International airport of Monterrey, Nuevo León, México.

## *4.2. Synthesis of polymer semiconductor*

Phenolic resins were prepared mixing 100 g of phenol with formaldehyde (P: F) at 1.5 molar ratio in 0.025 M oxalic acid solution for 30 minutes at 60°C. Next, the temperature was raised to 90°C and the mixture was continuously stirred for 5 hours. Afterward, sodium bicarbonate was added stoichiometrically to neutralize the oxalic acid and to stop the polymerization reaction. The resulting gel was washed three times with 100 mL of acetone and 100 mL of water and dried at 100°C for 14 h [74,76,90–92].

## *4.3. Chlorophyll solvent extraction*

The spinach leaves were macerated in a mortar with 10 ml of acetone (80% purity), samples were kept under diffuse light and submerged in an ice bath. Then, 1.3 g of calcium carbonate was added and mixed homogeneously until the appearance of the green liquid extract (*i.e.* solvent of chlorophyll extract). Subsequently, the solids were separated from the liquid extract by rapid filtration. The filtered solution

was centrifuged at 3000 rpm for 15 minutes, and the obtained supernatant was stored in an amber bottle for later use.

### *4.4. Incorporation of zinc oxide and chlorophyll on phenolic resin*

The incorporation of chlorophyll onto phenolic resin was carried out mixing 500 mL of the chlorophyll-extract solvent (chlorophyll concentration not measured) with 80 g of phenolic resin, then 250 mL of deionized water was added, and the chlorophyll was absorbed by the gel that is insoluble in water. Next, the water excess is removed by decantation, and the liquid gel was mixed with 5% w/w of polyvinyl alcohol (PVA) on a three-neck flask with reflux condenser system, where the temperature is at 70°C and continuously stirred during 45 minutes. Then, the temperature was raised (90°C) and 5% w/w hexamethylenetetramine (HMTA) was added as the crosslinking agent. This reaction was carried out for 5 hours and then the suspension was cooled to room temperature, obtaining brownish solid spherical particles related to the incorporated chlorophyll into the phenolic resin (R-C). The R-C spherical particles were crushed into powder in a vibratory mill for 5 minutes to get fine powder for further characterization and photocatalytic experiments. The incorporation of ZnO was carried out similarly as the previously described chlorophyll sensitization, but the metal oxide was mixed with the liquid gel (~10%w/w) before the addition of PVA.

### *4.5. Characterization of semiconductor materials*

To determine the molecular weight of the synthesized resins, gel permeation chromatography (GPC) was carried out. Briefly, 250 mg of phenolic resins from different molar ratios (R 1.50, R 1.75 and R 2.00) were separately dissolved with 10 mL of tetrahydrofuran (HPLC grade) and 1 mL of the resulting solution was filtered and deposited in a vial for its analysis on HPLC YL9100.

Fourier transform infrared spectra (FT-IR) were taken with a spectrophotometer (Perkin Elmer Spectrum One) in the frequency range of 4000–600 $cm^{-1}$ with a resolution of 4 $cm^{-1}$. Likewise, X-ray powder diffraction (XRD) was carried out in a

diffractometer Siemens D-5000, operating at 45 kV, 25 mA and CuKa radiation (λ=1.5406 A), from 5° to 90° (2θ angle).

Cyclic voltammetry (CVA) experiments for the synthesized phenolic resins were performed using a potentiostat/galvanostat (epsilon E2). The analytic solutions were prepared with 1.0 M NaCl as electrolyte and 1 g/L of phenolic resins (R 1.50, R 1.75 and R 2.00) on ultra-pure water (18 MΩ). Anaerobic conditions were established by flushing the solution with $N_2$ for 5 minutes in order to minimize the potential scavenging of reactive oxygen species. Graphite, coiled Pt wire, and Ag/AgCl were used as the working, counter, and reference electrodes. The electrodes were immersed in the analytic solution at room temperature in continuous stirring and electrochemical scanning was carried out at 20 mV/s. The measured potentials vs. Ag/AgCl were converted to the normal hydrogen electrode (NHE) scale according to the Nernst equation:

$$E_{NHE} = E_{Ag/AgCl} + 0.059\,pH + E^{\circ}_{Ag/AgCl} \ldots(143)$$

Where $E_{NHE}$ is the converted potential vs. NHE, $E^{\circ}_{Ag/AgCl} = 0.1976$ at 25°C, and $E_{Ag/AgCl}$ is the experimentally measured potential against Ag/AgCl reference.

The optical properties of the material were obtained by diffuse reflectance UV-vis and conventional UV-vis spectrometry. The specific extinction coefficient was determined from extinctance measurements as previously reported [93]. Briefly, synthesized materials were dried in an oven at 100°C during 12 h. Suspensions of 1 g/L of catalyst load ($C_{cat}$) were prepared with ultra-pure water (18 MΩ) and sonicated during 30 min. Prior the measurement, each suspension was sonicated one more time for 10 min and a scanning wavelength was recorded from the UV-vis spectrophotometer (Thermo Scientific, Genesis 10S) in the range of 300 to 800 nm. The absorbance readings obtained from the spectrophotometer are denoted as $EXT_{\lambda}$, for each wavelength ($\lambda$) and each cell path length (L), the specific extinction coefficient can be written as:

$$\beta_{\lambda} = \frac{2.303 EXT_{\lambda}}{L(cm) C_{cat}} \ldots(144)$$

The diffuse reflectance absorption spectra (DRS) of the samples were recorded in the range from 300 to 800 nm using a Hitachi U-3010 spectrophotometer equipped with an integrated sphere attachment and $BaSO_4$ was used as a reference. The Kubelka-Munk theory was employed to obtain the isotropic scattering albedo as follows. The scattering albedo can be defined as:

$$\omega_\lambda = \frac{\sigma_\lambda}{\beta_\lambda} = \frac{\sigma_\lambda}{\sigma_\lambda + \kappa_\lambda} \dots (145)$$

Where, $\sigma_\lambda$ is the specific scattering coefficient and $\kappa_\lambda$ is the specific absorption coefficient. Also, $\beta_\lambda$ is the specific extinction coefficient and the sum of the contribution of $\sigma_\lambda$ and $\kappa_\lambda$. Likewise, the Kubelka-Munk equation can be written as:

$$f\left(R_\lambda\right) = \frac{\left(1-R_\lambda\right)^2}{2R_\lambda} = \frac{\kappa_\lambda}{\sigma_\lambda} \dots (146)$$

Where, $R$ is the reflectance fraction of the sample at a specific wavelength. Therefore, combining equation (145) and (146), we obtain:

$$\omega_\lambda = \frac{2R_\lambda}{1+R_\lambda{}^2} \dots (147)$$

Once scattering albedo is obtained, specific scattering and absorption coefficient can be subtracted from equation (146). Furthermore, Tauc plot was employed to obtain the energy gap of the synthesized photocatalyst as follows:

$$f\left(E_g\right) = \left(\kappa_\lambda h\nu\right)^{1/r} \dots (148)$$

Where, $h$ is the Planck constant, $\upsilon$ is the wave frequency and $r$ denotes the nature of the transition. For the evaluated materials, the direct allowed transition $r = 1/2$ fits better with the experimental reflectance measurements.

The point of zero charge determination was determinate by the equilibrium pH technique. Samples of 80 mg of semiconductor were added separately to 80 mL of as prepared aqueous solution at different initial pH values in the range of 3.13 – 10.84. These experiments were continuously stirred at 150 rpm under dark conditions, until equilibrium was achieved. The pH of the final solution was measured, and the ΔpH were calculated ($\Delta pH = pH_{eq} - pH_f$) in order to find the pH value where the semiconductor has equilibrated charges (ΔpH = 0).

## *4.6. Adsorption isotherms*

The adsorption capacity of methylene blue onto the synthesized materials, as well as for zinc oxide was determinate on four different water matrices: deionized water, tap water, acidified tap water, and alkaline water. Samples of 80 mg of semiconductor were added separately to 80 mL of methylene blue concentrations of 5-20 mg/L. These experiments were continuously stirred at 150 rpm until equilibrium was achieved. Aliquots of 1 mL were taken to measure the initial and the final methylene blue concentration by UV-vis spectrophotometer at 664 nm.

## *4.7. Activity tests*

For activity tests, prior to the blue wastewater assessment, methylene blue was employed as a model pollutant, because of the presence of this dye on the sanitizing product of toilet disinfection. Briefly, a mass of 80 mg of sample powder photocatalyst (phenolic resins R 1.50, R 1.75, R 2.00, R-ZnO and R-C) was dispersed in deionized water (DW), tap water (TW), acidified tap water (ATW) and alkaline water (AW), with 5, 10 and 15 mg/L of dye concentration on 120 mL serum bottles containing 80 mL. These bottles were immediately sealed with Teflon stoppers and aluminum caps. The experiments were carried out at aerobic conditions and continuous stirring (See Figure 4). Following, decolorization kinetics were carried out in a photocatalytic chamber, continuously irradiated with 50 W LED 5000K. Sample aliquots were withdrawn intermittently during the illumination time and centrifugated for catalyst sedimentation. The supernatant was analyzed to measure the methylene blue concentration over time by UV-vis spectrophotometer (Thermo Scientific Genesis 10S) at 664 nm.

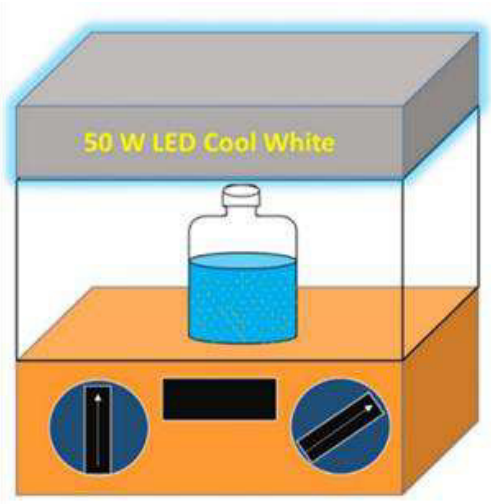


**Figure 4.** Schematic photocatalytic chamber irradiated with 50W LED lamp.

## *4.8. Photocatalytic blue wastewater degradation*

The photocatalytic blue wastewater degradation was carried out as the previously described activity tests (section 4.7). A synthetic blue wastewater was prepared with the aircraft lavatory deodorant Sani-Pak® with an initial MB concentration of 10 mg/L using tap water (TW) and acidified tap water (ATW). Then, the photocatalytic blue wastewater degradation was evaluated with three different catalyst dosage (1, 2 and 3 g/L) analyzing dye concentration by UV-vis at 664 nm and the chemical oxygen demand (COD), following the closed-reflux procedure proposed by the standard methods for the examination of water and wastewater of the American Public Health Association [94].

## *4.9. Scavenger tests*

To understand the physicochemical role of reactive oxygen species, controlled photoactivity experiments using different scavengers were carried out as the above-mentioned photocatalytic activity tests (section 4.7), except that scavenger (20 mM) were added to the reaction system. The selected scavengers in aerobic conditions were anthraquinone-2-sulfonate (AQS), ascorbic acid (AA) and acidic conditions (pH 4.3). Likewise, under anaerobic conditions, AQS, AA, pyruvate, and acidic conditions were employed [75,76,95–97]. To validate the EPM model, kinetic

constants were determined by the method of the least squares, employing a pseudo first-order kinetic model:

$$\ln\left(\frac{C_{i,0}}{C_i}\right) = \mathrm{k}_{app} t \ \ldots(149)$$

Where $\mathrm{k}_{app}$ is the pseudo first order apparent rate constant for dye decolorization, $C_{i,0}$ is the initial dye concentration, $C_i$ is the dye concentration over time of irradiation ($t$). The involved scavenging species are presented in Table 2.

**Table 2**. Scavenging of the reactive oxygen species (ROS) employing different scavengers (red filled cells) and the inhibition of generation of the ROS (gray filled cells) on (A) $O_2$ atmosphere and (B) $N_2$ atmosphere.

| ***Scavenger*** | (A) $O_2$ atmosphere | | | | | (B) $N_2$ atmosphere | | | | |
|---|---|---|---|---|---|---|---|---|---|---|
| | **OH·** | **$O_2^{-}$·** | **$CO_3^{-}$·** | **$e^-$** | **$h^+$** | **OH·** | **$O_2^{-}$·** | **$CO_3^{-}$·** | **$e^-$** | **$h^+$** |
| ***Without (control)*** | | | | | | | | | | |
| ***Ascorbic acid*** | | | | | | | | | | |
| ***AQS*** | | | | | | | | | | |
| ***Pyruvate*** | | | | | | | | | | |
| ***pH 4.3*** | | | | | | | | | | |

AQS: anthraquinone-2-sulfonate

## *4.10. Effective photocatalytic mechanism*

To validate the effective photocatalytic mechanism (EPM) model, equation (3) must be accomplished. The values of $\varphi_i$ were estimated by equation (9-14) from the pseudo first order apparent reaction rate constants estimated from scavenger tests. For the scavenging of reactive ionic species, acidic conditions were established to minimize the presence of bicarbonate species and, therefore, the equation 9 can be rewrite as follows:

$$\varphi_{CO_3^{-}\cdot} = \left( \frac{\mathrm{k}_{app,pH\,4.3}^{O_2}}{\mathrm{k}_{app,control}^{O_2}} \right) \ldots (150)$$

Likewise, the robustness of the model was also evaluated on different photocatalytic water matrices, and the results are discussed in section 5.5.

## *4.11. SFM-HG of semiconductors*

To evaluate the radiation absorption on the visible-LED tubular reactor, SFM-HG was employed assuming a distributed parameter system with isotropic radiation incident perpendicularly to the reactor in the yz plane (g=0). The optical properties of the synthesized semiconductors were obtained from the previous characterization. For cylindrical geometries, the LVRPA is given by the following equation:

$$\hat{e}_{\lambda}^{a} = \frac{I_0}{\lambda_{\omega,corr}\omega_{corr}\left(1-\gamma\right)}\left[\left(\omega_{corr}-1+\sqrt{1-\omega_{corr}{}^2}\right)e^{-r'_P/\lambda_{\omega,corr}} + \gamma\left(\omega_{corr}-1-\sqrt{1-\omega_{corr}{}^2}\right)e^{r'_P/\lambda_{\omega,corr}}\right] \ldots (151)$$

The incident radiation on the photocatalytic chamber for the plug flow reactor was estimated by the linear source spherical emission (LSSE) model along the reactor length (z). In Figure 5, the representative geometry of the lamp emission is established, as well as the following equation represents the incident radiation profile near the reactor wall:

$$I_{r,z} = \frac{r_1 I_w}{2}\int_{(H-L)/2}^{(H+L)/2} \frac{1}{r^2+\left(z-x'\right)^2}dx' \ldots (152)$$

$$I_{(\eta R),z} = \frac{r_1 I_w}{2\eta R}\left[\arctan\left(\frac{2z-H+L}{2\eta R}\right) - \arctan\left(\frac{2z-H-L}{2\eta R}\right)\right] \ldots (153)$$

Where, L is the length of the lamp (m) and H is the length of the reactor (m) in the z-direction, and ηR is the distance between the lamp and the outer wall. The model was validated with the average measure of the incident radiation with a visible-light range radiometer along the reactor length inside the photocatalytic chamber.

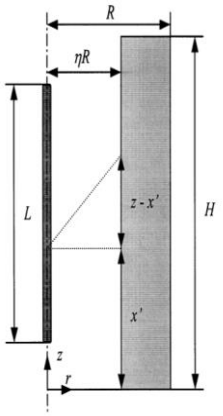


**Figure 5.** The geometry of the incident radiation over a plug flow reactor of sodium borosilicate glass.

Once the incident radiation is estimated, the photon distribution on the reactor volume can be simulated by the LVRPA. To associate the radiant field contribution on the kinetic model, the overall rate of photon absorption (OVRPA) can be calculated by the following equation:

$$OVRPA = \hat{E}^{a}_{g(\lambda\rightarrow\lambda')} = \frac{1}{v_R}\int_{v} \hat{e}^{a}_{\lambda} dv \quad \ldots(154)$$

## *4.12. The laboratory scale tubular reactor*

A laboratory scale tubular reactor, located at the laboratory of chemical engineering (I) in the graduate school of chemical sciences, was employed for the treatment of methylene blue and synthetic blue wastewater, as well as for the validation of the proposed models. It was operated in batch mode with recirculation, a flow-through mode with the water passing through an external tank as observed in Figure 6.

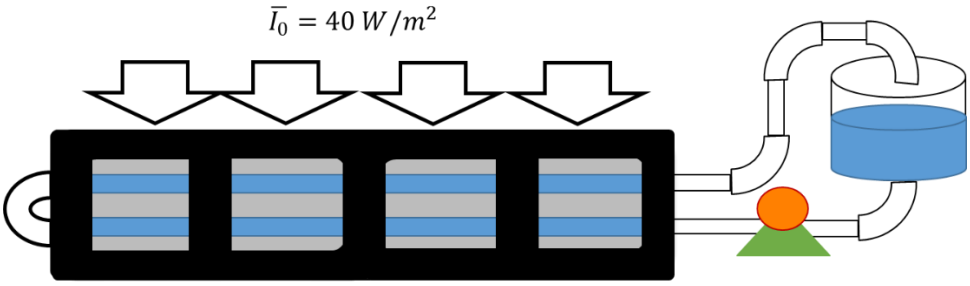


**Figure 6.** Representative scheme of the LED tubular reactor with recirculation; about 1 L of illuminated volume.

The reactor was continuously irradiated by a four LED lamps symmetrically distributed along the reactor length. The concentration of the substrate "i" after each pass through the reactor was estimated from the material balance and the axial coordinate z:

$$\frac{dC_{R_i}}{dt} = \frac{V_R}{V_T}\langle R_i \rangle \ldots(155)$$

$$v_z \left.\frac{dC_A}{dz}\right|_{\tau pass} = \frac{1}{V_T}\int_0^R r \int_0^{2\pi} r_i(r,\theta) \ldots(156)$$

For small reactant conversions per pass, a condition which is verified in many standard solar tubular photoreactors because of small Damkholer numbers, the material balance can be expressed as an equation with the reaction step at a pseudo-steady-state evaluated for each spatial time $\tau_{pass}$ (residence time) as a function of the axial coordinate (z).

$$n_{Pass,Total} = \frac{Qt}{V_R} \ldots(157)$$

The reactant concentration at the reactor outlet corresponds to the evaluation of equation (156) at z = L (reactor length) was coupled with the balance of the liquid volumes in the dark to yield a relationship between concentration at the inlet and outlet of the reactor:

$$C_{R_i,\tau pass+1} = \frac{C_{R_i}(t-\tau_{pass})[V_T - V_R] + C_{R_i}(\tau_{pass})V_R}{V_T} \ldots(158)$$

With $i = 1,2,3...n_{pass}$

Where "$i$" is the number of passes.

For photodegradation of blue wastewater, the concentration $C_{R_i}$ may be replaced by a global concentration parameter such as COD or TOC concentration.

The predominant hydrodynamic flow regimes in the tubular reactor were turbulent with negligible viscous effects. The hydrodynamic equation was taken from the literature [55]:

$$\frac{v_z}{v_{\max}} = \left(1 - \frac{r}{R}\right)^{1/\eta_z} \ldots(159)$$

$$\eta_z = 0.41\sqrt{\frac{8}{f}} \ldots(160)$$

$$f = \frac{0.0076\,\mathrm{Re}^{*0.165}}{1 + \mathrm{Re}^{*7.0}} + \frac{16}{\mathrm{Re}} \ldots(161)$$

$$\mathrm{Re}^* = 3170 / \mathrm{Re}$$

$$\frac{v_{z,\max}}{v_{z,av}} = \frac{(\eta_z + 1)(2\eta_z + 1)}{2\eta_z{}^2} \ldots(162)$$

$$v_{z.av} = \frac{Q}{\pi R^2} \ldots(163)$$

## *4.13. Photocatalytic blue wastewater treatment: model validation and further predictions*

The best-obtained result from the photocatalytic blue wastewater degradation was carried out in the visible-LED tubular reactor. The COD concentration was analyzed at selected periods during 6 h of treatment. The experimental data were computed to fit with the proposed kinetic model that further consider the radiative effects, as well as the quantum yield of the photocatalyst. A predictive simulation was carried out changing the operational parameters of the photocatalytic treatment. A detailed discussion is present in section 5.7.

## *4.14. Waste management*

All generated wastes (solid and liquid) were disposed of according to the general disposition of hazardous waste established by the environmental, health and safety department of the School of Chemical Sciences, UANL.

# 5. Results and discussion

In order to assess the influence of the polymerization degree of the synthesized phenolic resins at different molar ratios, an extensive characterization of these materials, as well as photocatalytic activity tests, were performed. In the following sections, a more in detail discussion is shown.

## *5.1. Selection of the molar ratio of the synthesized phenolic resins*

### 5.1.1. The polymerization degree of phenolic resins

Gel permeation chromatography (GPC) technique was first used to determine the molecular weight and polydispersity index ($PD_{index}$) of the synthesized phenolic resins. When the molar ratio (P: F) increased, the molecular weight ($M_w$) of the polymer decreased and the $PD_{index}$ slightly increased (Table 3). This last result may suggest that despite the difference between molecular weight, the molecule size dispersion is similar in all three cases (R 1.50, R 1.75, R 2.00); therefore, the most important effect on the photocatalytic properties will be associated to the number of moles present in each resin.

**Table 3.** Surface state energies ($E\ e_s^-$, $E\ h_s^+$), optical properties ($E_{gap}$, $\lambda_{act}$), molecular weight ($M_w$) and polydispersity index ($PD_{index}$) of the synthesized phenolic resins at the different molar ratio (1.50, 1.75, 2.00).

| Phenolic resin | $E\ e_s^-$ (V) | $E\ h_s^+$ (V) | $E_{gap}$ (eV) | $\lambda_{act}$ (nm) | $M_w$ (g/mol) | $PD_{index}$ |
|---|---|---|---|---|---|---|
| R 1.50 | -0.169 | 2.161 | 2.17 | 480 | 1831 | 4.764 |
| R 1.75 | -0.183 | 2.03 | 2.10 | 482 | 1252 | 4.813 |
| R 2.00 | -0.177 | 1.976 | 2.06 | 493 | 843 | 4.939 |

Surface state energies were estimated via cyclic voltammetry by the Nernst equation (Eq. 143); optical properties were estimated by Kubelka - Munk function using reflectance spectra obtained from diffuse reflectance UV-vis analysis (Figure S1 from supplementary material); molecular weight and polydispersity index were obtained by gel permeation chromatography.

### 5.1.2. Electrochemical and optical properties of phenolic resins

Table 3 shows the surface state energies of the phenolic resins at different molecular weight estimated by CVA experiments. It is important to mention that

electron trapping energy of all resins ($E_{e_s^- / R\ 1.50}$) was lesser than the oxygen reduction energy for superoxide radical generation. Conversely, the hole trapping energy of resins ($E_{h_s^+ / R\ 1.50}$) was lower than the water oxidation energy to hydroxyl radical generation, but higher for other reactive oxygen species that further degrade organic contaminants. These findings prevailed throughout the pH range as shown in Figure 7.

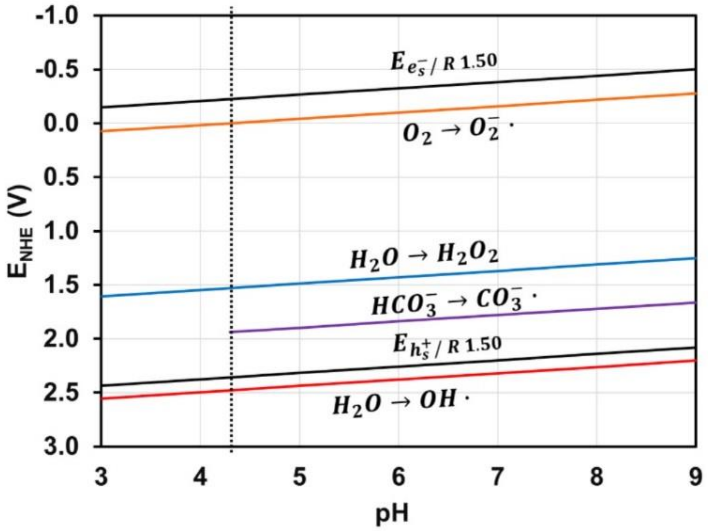


**Figure 7.** Energy requirements along the pH range to generate reactive oxygen species, and surface states energies for R 1.50.

It is also important to notice that carbonate radical energy generation is lower than the hole trapping energy of the resins (Figure 7); therefore, bicarbonate alkalinity may act as a scavenger of other reactive oxygen species [28,29], or as a promoter on the photolytic degradation process [88]. Consequently, the physicochemical mechanism of phenolic resins for degradation/transformation of contaminants could be electrochemically possible via hole trapping, hydrogen peroxide, electron trapping, superoxide radical and carbonate anion radical.

Additionally, the energy gap and activation wavelength were estimated by the Kubelka-Munk function from the UV-vis reflectance spectra and the results are summarized in Table 3. The red-shifts in the absorption of light for all three resins can be attributed to the changes in the density of electronic states of the aromatic rings upon functionalization, dominated by direct pi-pi* transitions [75,76]. To

further confirm this optical characteristic, scattering albedo (related to the scattering contribution with respect to the incident photon energy) of resins were estimated and it is shown in Figure 8.

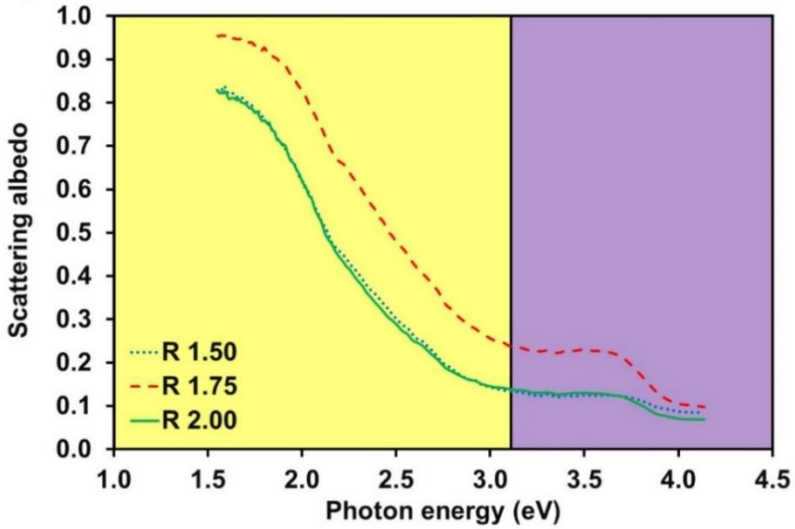


**Figure 8.** Scattering albedo associated with the photon energy usage (UV range is represented as a purple area, whereas visible range as a yellow area).

At UV photon energy range (>3.10 eV, purple zone in Figure 8), the scattering albedo remains lower than 0.139 for R 1.50 and R 2.00, but lower than 0.238 for R 1.75. These results suggest that all tested semiconductors have a high absorption capacity of UV-light, and it could be due to the low recombination rates. Likewise, the absorption of light prevailed higher than 50% of the incident radiation along visible range (yellow zone in Figure 8) with photon energy higher than 2.12 eV for R 1.50 and R 2.00, and 2.45 eV for R 1.75. It is also expected to have a high recombination activity with R 1.75 because the obtained scattering albedo (along with the UV-vis photon energy range) was higher than those estimated for R 1.50 and R 2.00 (Figure 8). This phenomenon may be related to the nitrogen atoms in phenolic resins, provided by the crosslinking agent in the curing stage. These nitrogen atoms could act as recombination sites, attaining a lower absorption of light. Despite the differences of scattering albedo, all phenolic resins maintained high absorption characteristics along the visible light region, which entails its

applicability on photocatalytic degradation processes with a visible source of irradiation.

### 5.1.3. Kinetics of decolorization

Based on the low photon energy to activate the semiconductor and scattering albedo analysis, all synthesized phenolic resins exhibited good optical properties in the visible light region. Therefore, the photocatalytic performance of phenolic resins under visible light for methylene blue degradation was evaluated. Figure 9 shows the results of the photocatalytic degradation of MB, evaluating the polymerization degree of phenolic resins on deionized water (DW), tap water (TW) and acidified tap water (ATW). For these three water matrices, photolysis control experiments showed relatively high color removal (about 45-78%) after 6 h indicating that MB was photo sensible under LED irradiation. This finding can be explained easily taking into account that MB acts as a photosensitizer, it may generate reactive oxygen species and degrades itself. If bicarbonate ions are presented in MB solutions, carbonate anion radical could be generated too and this radical may contribute to MB degradation [19].

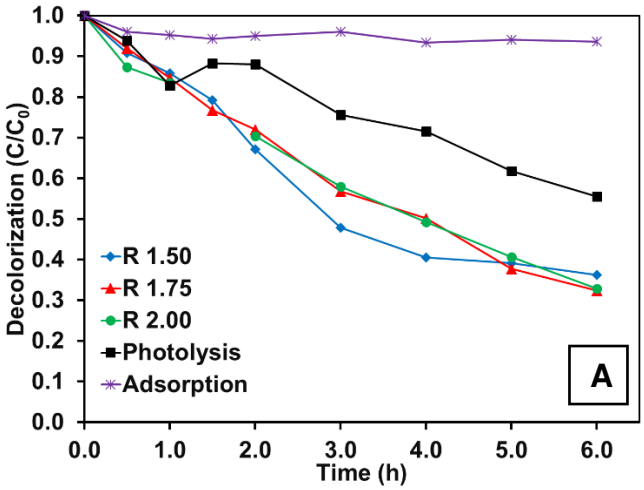

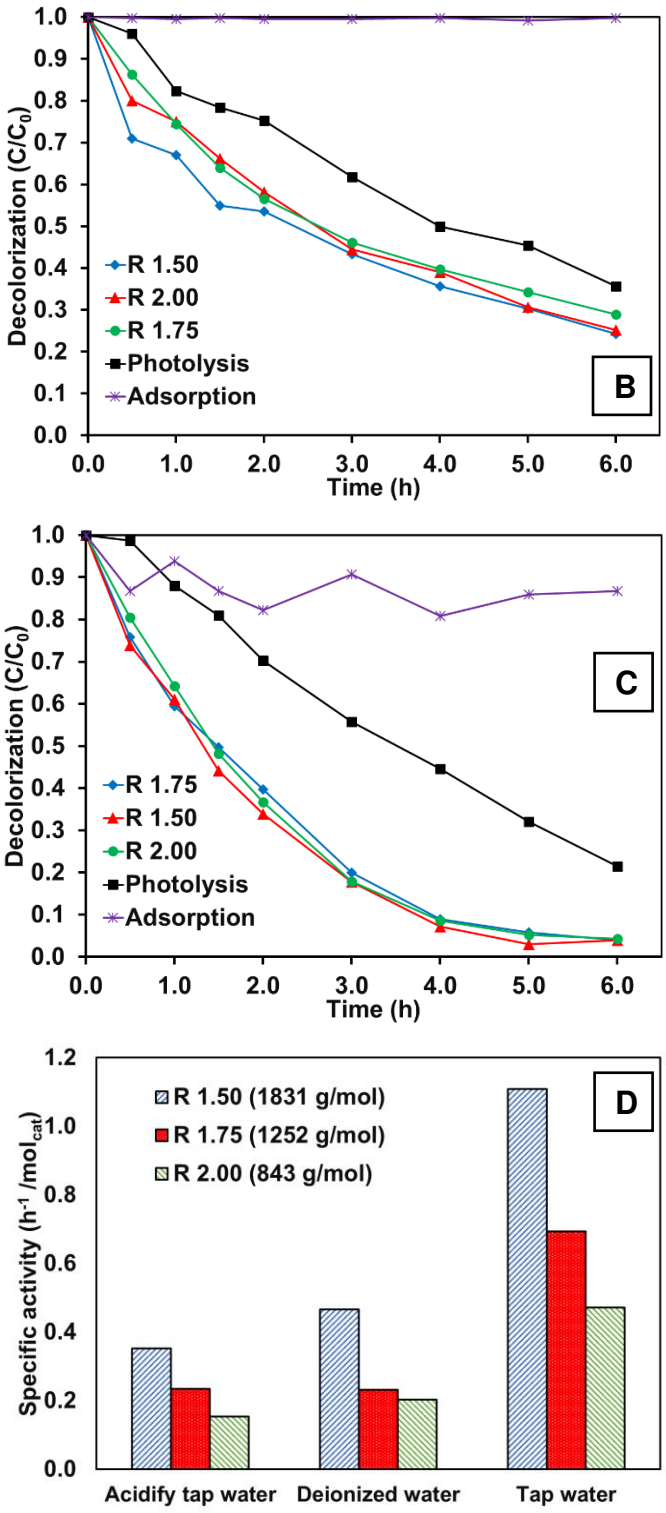


**Figure 9.** Kinetic decolorization of methylene blue using phenolic resins as a photocatalyst under LED irradiation, as well as the photolysis control on ATW (A), DW (B) and TW (C), as well as specific activity (D) of decolorization on ATW, DW, and TW.

Furthermore, decolorization of MB increased (about 70-97%) after 6 h of LED irradiation when phenolic resins were used as a photocatalyst (Figure 6A-C). Apparently, there was no effect on decolorization of MB regardless of the polymerization degree, showing no significant difference in kinetic behaviour between all tested phenolic resins. However, if the specific activity is compared among resins, a clear difference can be observed (Figure 9D). As the molecular weight of phenolic resin increased, a higher specific activity was achieved; consequently**,** R 1.50 demonstrated the highest activity for all three water matrices, being 1.6-fold greater than R 1.75 and 2.3-fold higher than R 2.00. Also, a diminished specific activity was observed as the pH of the water matrix decreases. This behaviour could be related to chloride anions presented on ATW (pH 4.3): these species could be scavenging surface holes, electrons or reactive oxygen species [98], diminishing the photocatalytic activity of phenolic resins compared to the other two water matrices. Moreover, a slight increase on the specific activity was observed on DW when no ionic species were presented in solution. Finally, an unexpected improved photocatalytic activity due to bicarbonate alkalinity was observed on TW, being 2.37 – 3.15 times greater than DW and ATW, respectively. This finding shows that R 1.50 is the best candidate for its modification with ZnO and chlorophyll molecules due to it's high specific activity with lesser need for its synthesis. Hence, following the methodology is shown in section 4.4, ZnO-incorporated phenolic resin (R-ZnO) and chlorophyll-sensitized phenolic resin (R-C) were obtained.

## *5.2. Characterization of synthesized semiconductors*

### 5.2.1. ZnO-incorporated phenolic resin

a. X-ray diffraction

Figure 10 shows the XRD patterns used to characterize the crystal phases and crystallinity of the photocatalysts, as well as for the incorporation of zinc oxide structures onto phenolic resins. According to the JCPDS card No: 00-036-1451, the crystalline phase of zinc oxide present on Figure 10A is associated with *zincite* structure [99]. Likewise, once ZnO was incorporated into the polymeric structure,

the crystal phase of zincite remained in the composite diffraction pattern (Figure 10C). It is important to notice that phenolic resin showed an amorphous phase with an intense signal at 19 degrees (2θ angle), related to carbon atoms and its observed in both diffractograms (Figure 10B-C) [100]. This valuable information suggests that the photocatalytic properties of zinc oxide may prevail once incorporated into the phenolic resin.

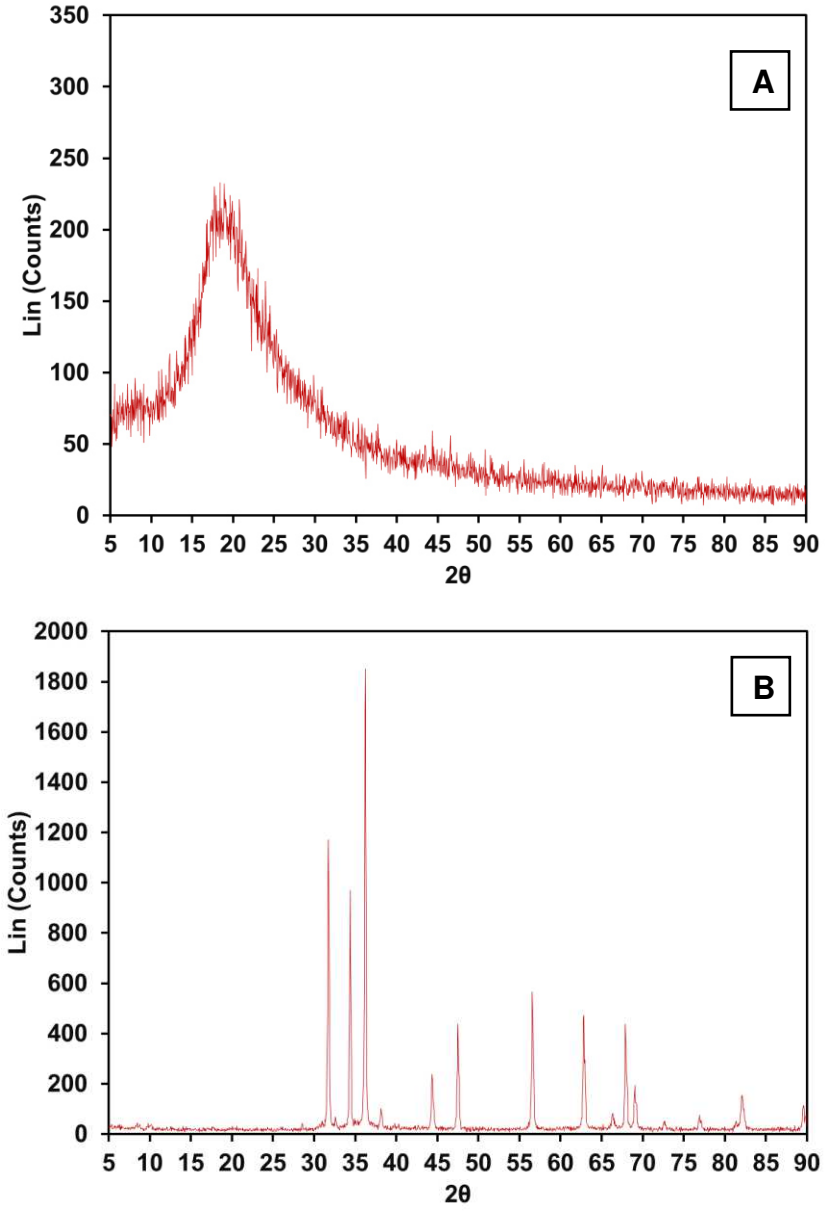

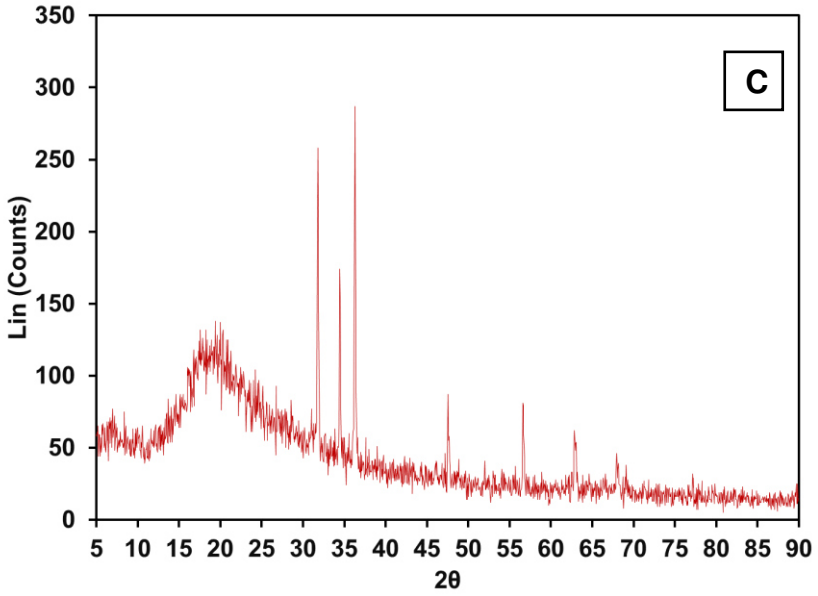


**Figure 10.** X-ray diffraction of A) phenolic resin (R), B) zinc oxide (ZnO) and C) R-ZnO.

b. Fourier transform Infrared spectrometry

Figure 11 shows the infrared spectra of zinc oxide, phenolic resins, and zinc oxide incorporated into phenolic resin. Typical bands of novolac phenolic resins are observed for both phenolic resin (R) and ZnO-incorporated phenolic resin (R-ZnO) [101]. Hydroxyl functional groups appeared in both infrared spectra with a slight signal at 3300 $cm^{-1}$, being for R stronger than R-ZnO, which implies an interaction of ZnO structure on the hydroxyl groups. Moreover, both resins showed signals at 1596, 1509 and 1441 $cm^{-1}$, corresponding to the aromatic ring vibrations of the phenyl-propane monomer. It is important to notice that both phenolic resin and ZnO-incorporated phenolic resin showed a similar intensity of transmittance signals, indicating that the polymeric structure remained almost equals in both cases, except at 1000 cm-1, observing a stronger signal for R-ZnO that could be attributed to the ZnO transmittance observed at the same wavenumber. These findings suggest that the immobilization mechanism of ZnO can be due to electrostatic interaction with the hydroxyl groups of the phenyl-propane monomer. This behaviour was also observed on titanium dioxide incorporated into phenolic resins [74,77].

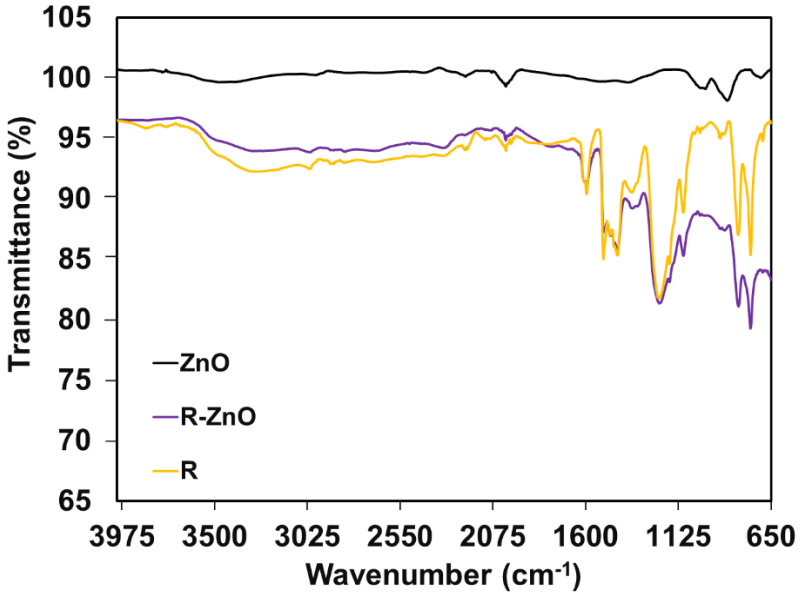


**Figure 11.** ATR-FTIR spectra of zinc oxide and phenolic resin.

c. Optical and electronic properties

Absorption coefficient estimation was carried out for modified and unmodified phenolic resin, as well as for zinc oxide, and the obtained results are observed in Figure 12. As expected, zinc oxide presented a higher absorption coefficient on the UV range, being about 6 times greater than the synthesized phenolic resins. It is well known that zinc oxide achieves high activity for photocatalytic degradation process, being considered as the cheapest substitution of titanium dioxide for it similarly photocatalytic properties [66]. Even more, it is interesting to notice that the coupling of zinc oxide onto polymeric structures, increases its absorption on both UV and visible range. As observed in Figure 12, R-ZnO showed an increase in the absorption of light, is almost three times higher than the unmodified phenolic resin. These results suggest that even with a low proportion of metal oxide semiconductor (~10%) incorporated into the polymeric structure, its optical properties were improved. Similar optical properties were reported with the resol-type phenolic resin modified with titanium dioxide [102].

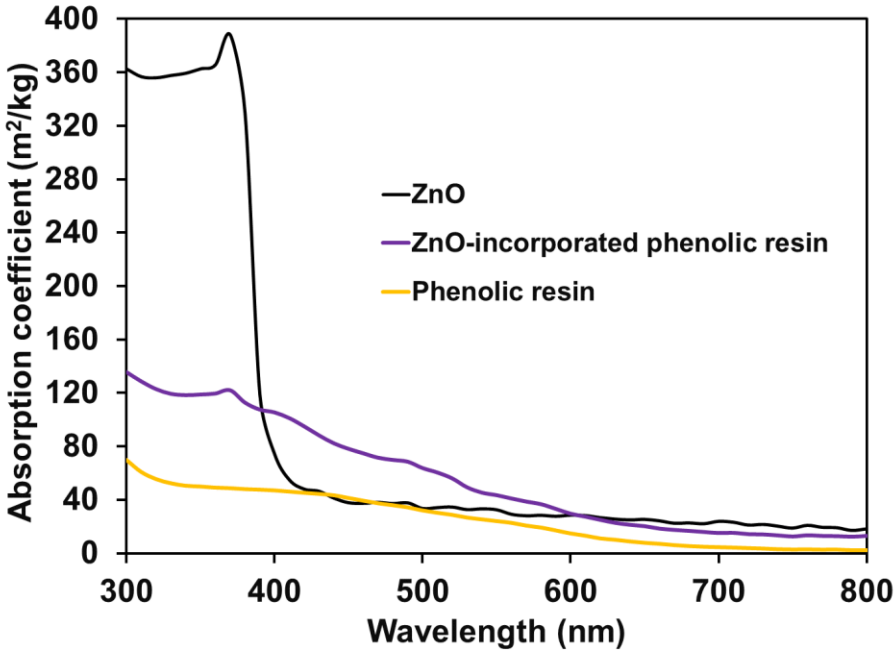


**Figure 12**. The absorption coefficient of zinc oxide and phenolic resin structures.

Additionally, electrochemical properties of semiconductors give valuable information about the reaction that could be carried out on the photocatalytic processes. It is expected that the inclusion of zinc oxide on the phenolic resin structure could change the reaction pathway for the generation of reactive oxygen species. Figure 13 shows the electrochemical behaviour of both synthesized resins, observing a maximum anodic peak at 1710 and 1736 mV, and a maximum cathodic peak at -619 and -803 mV, for phenolic resin and ZnO-incorporated phenolic resin, respectively.

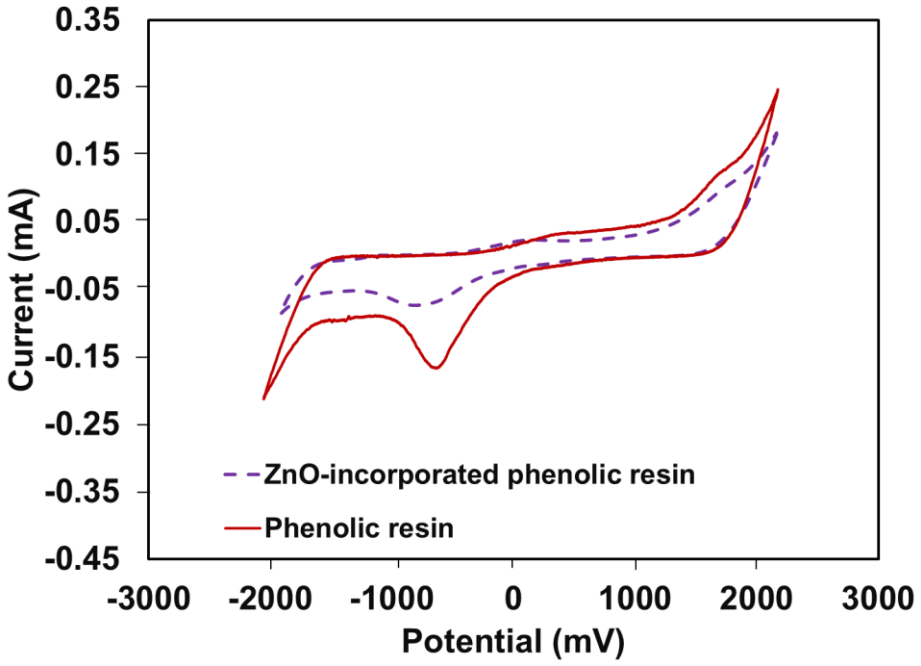


**Figure 13.** Current-potential measurements for phenolic resin and ZnO-incorporated phenolic resin.

The lower current intensity of R-ZnO compared to the unmodified phenolic resin indicated that ZnO deaccelerates the electron transport through the organometallic lattice. However, a diminishing on the reduction potential may allow several reduction reactions with higher energy requirements that further enhance the photocatalytic degradation of water pollutants. On the contrary, the oxidation potential does not change evidently, so is expected that mechanistic oxidation pathway will not change between modified and unmodified phenolic resin. Moreover, the surface states energies $\left(h_r^+ + e_r^-\right)$ were estimated following the equation (143), as well as the standard redox potential was calculated as follows:

$$E^{\circ}_{redox} = \frac{E_{h_r^+} + E_{e_r^-}}{2} \quad \ldots(164)$$

The summarized results are present in Table 4.

**Table 4.** Redox potentials and reactive surface states of the studied semiconductors.

| *Semiconductor* | $E_{ox}$ (V) | $E_{red}$ (V) | $h_r^+$ (V) | $e_r^+$ (V) | $E°_{redox}$ (V) |
|---|---|---|---|---|---|
| ***Phenolic resin*** | 1.710 | -0.619 | 2.161 | -0.167 | 0.996 |
| ***ZnO-incorporated phenolic resin*** | 1.736 | -0.803 | 2.1873 | -0.351 | 0.9178 |

As observed in Table 4, electron trapping energy of ZnO-incorporated phenolic resin is 2.1 times greater than the unmodified phenolic resin. This increasing energy can generate superoxide radical species and it is high enough for water splitting reaction for hydrogen production. Likewise, hole trapping remains almost equal after ZnO incorporation being capable of generating hydrogen peroxide and carbonate anion radical (Figure 7). Even more, the standard redox potential decreases, suggesting a selective reduction process due to ZnO particles incorporated into the phenolic resin.

Additionally, the optical energy gap of both synthesized materials was estimated by the Tauc plot (equation ), from the absorption coefficient estimation described in section 4.5. As observed in Figure 14, phenolic resin showed a photon energy need about 2.16 eV (570 nm) that is consistent with the reported on the literature [74–77]. In contrast, ZnO-incorporated phenolic resin showed two energetic boundaries. The first one at the same energy gap of phenolic resin, attributed to the phenolic resin itself and its high proportion on the synthesized semiconductor. Moreover, the second limit is observed at 2.53 eV (about 490 nm), attributed to the ligand to metal charge transfer (LMCT) of phenolic resins to zinc oxide structures, which increase the optical energy gap of phenolic resin(about 2.16 eV). A similar behaviour was also found for other composite semiconductors, except that the metal oxide quantity was higher than the polymeric structure [37,74,77].

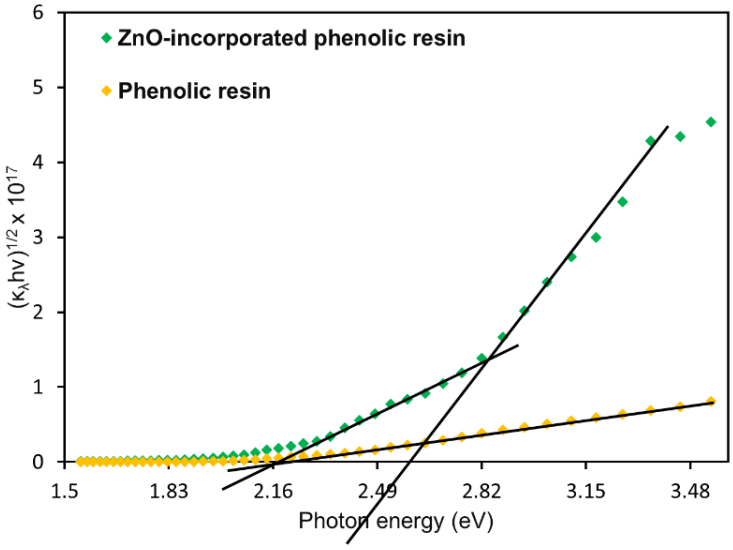


**Figure 14.** Energy gap determination for phenolic resin and ZnO-incorporated phenolic resin.

### 5.2.2. Chlorophyll-sensitized phenolic resin

a. Fourier transform infrared spectrometry

Figure 15 shows the FTIR spectra of chlorophyll, phenolic resins, and chlorophyll-sensitized phenolic resins. Functional groups of chlorophyll dye, extracted from spinach leaves, were associated with O-H and N-H vibrations as strong bands at 3400 and 1650 $cm^{-1}$, respectively (Figure 14a). Furthermore, C=O stretch band at 1703 $cm^{-1}$, the C-O stretch band at 1093 $cm^{-1}$ and a C-N stretch band of porphyrins at 1642 $cm^{-1}$ are also observed in the chlorophyll spectra [103]. On the other hand, typical bands of novolac phenolic resins are observed for both phenolic resin and chlorophyll-sensitized phenolic resin [101]. Hydroxyl functional groups appear in both infrared spectra with a slight signal at 3300 $cm^{-1}$. Moreover, both resins showed transmittance at 1596, 1509 and 1441 $cm^{-1}$, corresponding to the aromatic ring vibrations of the phenyl-propane monomer. Likewise, chlorophyll-sensitized phenolic resin showed a strong band at 1700 $cm^{-1}$ that is related to carbonyl groups present on chlorophyll, but this signal was not exhibited on phenolic resin, confirming the presence of chlorophyll molecules on the polymeric structure. It is important to notice that chlorophyll-sensitized resin showed a stronger signal of transmittance than the unmodified phenolic resin. This result suggests a higher number of phenyl-propane groups present on the phenolic resin of the sensitized

material, suggesting a crosslinking immobilization across the polymeric matrix. Also, the markedly C-N stretch band observed at 1367 and 1600 $cm^{-1}$ of sensitized resin, could suggest the immobilization bound of chlorophyll molecules.

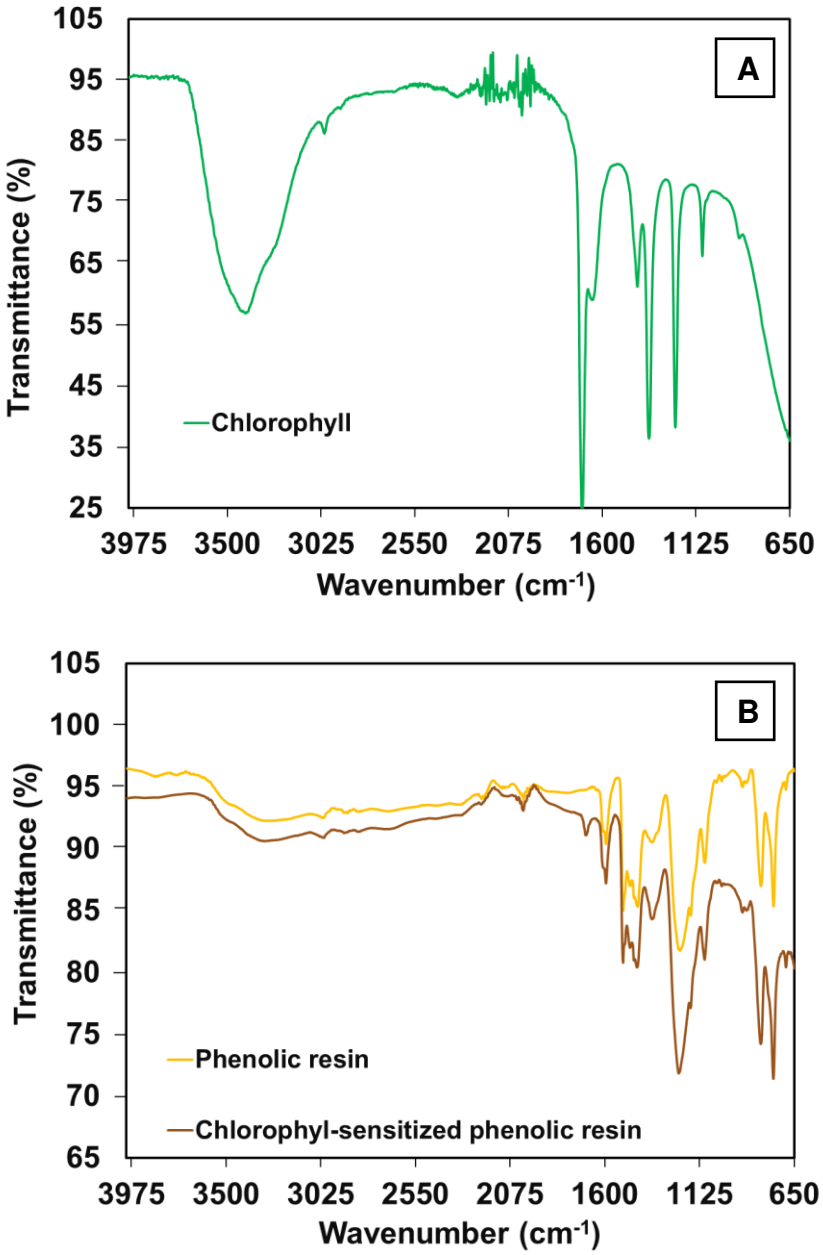


**Figure 15.** ATR-FTIR spectra of A) chlorophyll molecules and B) phenolic resin structures (chlorophyll concentration not measured).

b. Optical and electronic properties

For dye-sensitized materials, two mains characteristics are enhanced for the photocatalytic process. The first one is related to the promotion of a harvesting site for a better absorption of light and the second one is associated with the interfacial electron transport enhancement. Therefore, absorption coefficient estimation was carried out for both synthesized materials following the methodology described above and the results are plotted in Figure 16.

As observed in Figure 16, the highest absorption of light was achieved by chlorophyll-sensitized phenolic resin, is about 2.6 to 9.1 times greater than phenolic resin absorption of light on the visible range (400 – 800 nm). These results revealed that chlorophyll sites present in the polymeric structures further absorb a higher quantity of photons for activation in comparison with the unmodified phenolic resins. Also, it should be noted that an absorption peak near 680 nm is observed and can be attributed to the maximum absorption peak of *photosystem*, that is the most powerful oxidant known in biology [104].

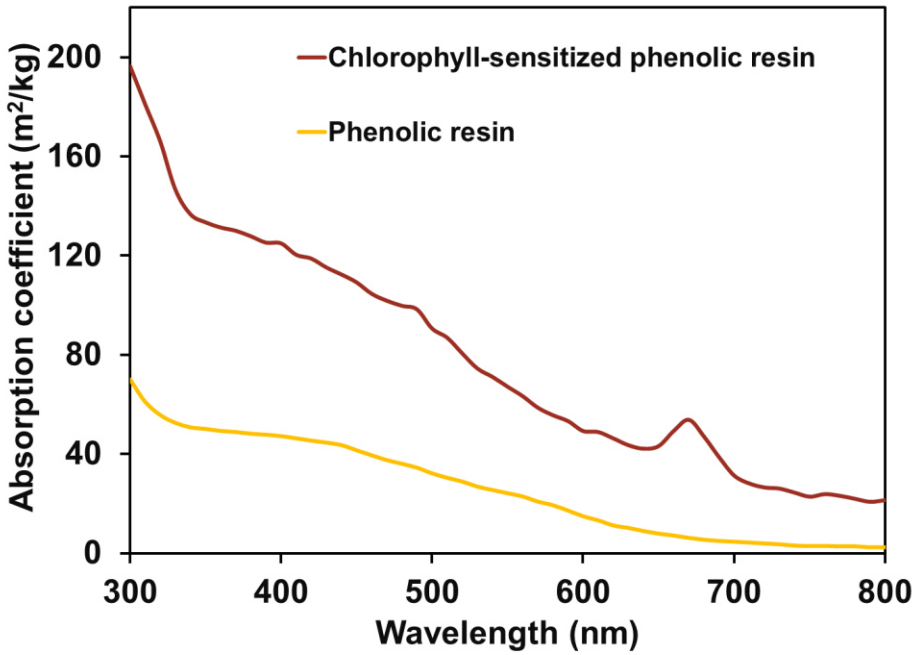


**Figure 16**. The absorption coefficient of phenolic resin and sensitized phenolic resin structures.

This oxidative potential, associated with the electrochemical behaviour of the photocatalyst, can be evaluated by CV measurements. Figure 17 shows the

electrochemical behaviour of both synthesized resins, observing a maximum anodic peak on 1710 and 1830 mV, and a maximum cathodic peak at -619 and -628 mV, for phenolic resins and chlorophyll-sensitized phenolic resins, respectively.

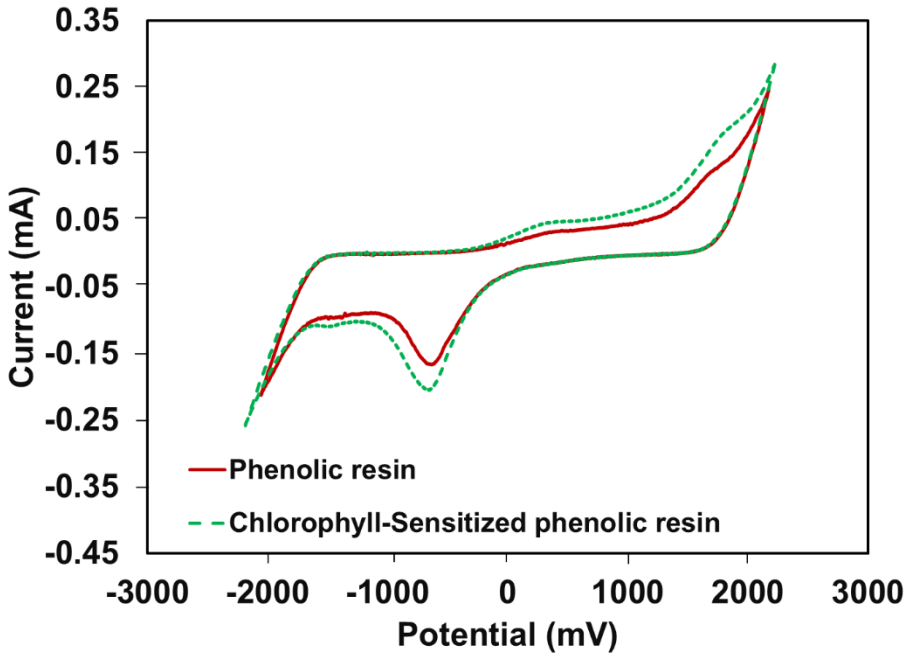


**Figure 17.** Current-potential measurement for phenolic resin and chlorophyll-sensitized phenolic resin.

This oxidation and reduction potential enhancement can be attributed to the chlorophyll molecules incorporated into the polymeric structure of phenolic resins. Even more, the higher current intensity of the sensitized resin indicates a minor resistance for interfacial electron transport as observed on photosystem II [104]. A similar behaviour was reported previously for other dye-sensitized materials [31]. As above-mentioned, the surface states energies were estimated following the equation (14), as well as the standard redox potential from the equation (164). The summarized results are present in Table 5.

**Table 5.** Redox potentials and reactive surface states of the studied semiconductors.

| *Semiconductor* | $E_{ox}$ (V) | $E_{red}$ (V) | $h_r^+$ (V) | $e_r^+$ (V) | $E°_{redox}$ (V) |
|---|---|---|---|---|---|
| ***Phenolic resin*** | 1.710 | -0.619 | 2.161 | -0.167 | 0.996 |
| ***Chlorophyll-sensitized phenolic resin*** | 1.830 | -0.629 | 2.261 | -0.213 | 1.023 |

Hole and electron trapping energies of chlorophyll sensitized phenolic resin increased about 5% compared to the unmodified phenolic resin. Likewise, hole trapping energy is high enough to generate hydrogen peroxide (E = 1.510 V). However, hydroxyl radical cannot be generated electrochemically after semiconductor photoactivation (E=2.500 V). On the other hand, electron trapping energy is suitable for a superoxide anion radical generation (0.080 V). Additionally, the optical energy gap of both synthesized materials was estimated by the Tauc plot (equation 148), from the absorption coefficient estimation described in section 2.4. As observed in Figure 18, phenolic resin showed a photon energy requirement of about 2.16 eV (570 nm), which is consistent with the reported on the literature [74–77]. Even more, chlorophyll-sensitized phenolic resin showed two energetic boundaries. The first one appears with a strong absorption of light at the same energy gap of phenolic resin. Likewise, the second limit slightly showed up at 1.75 eV (about 700 nm), attributed to the chlorophyll optical energy gap. This behaviour suggests that chlorophyll absorption sites are distributed along the polymeric structure of phenolic resin, thereby no change on the energetic requirement are observed to surpass the optical energy gap of the material.

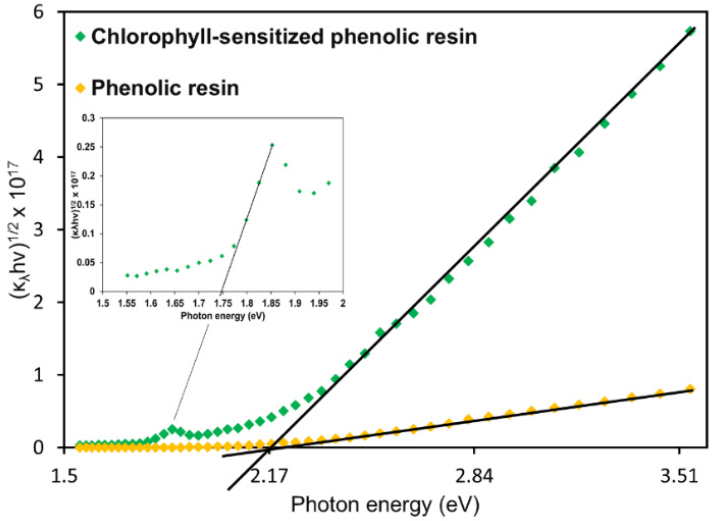


**Figure 18**. Energy gap determination for phenolic resin and chlorophyll-sensitized phenolic resin. Inset shows the photon energy region of the observed peak.

It is important to notice that the standard redox potential of methylene blue at pH 4.3 (E°= 0.212 V, estimated from reference [105]) is lower than the phenolic resin and both modified phenolic resin standard redox potential (Table 4 and 5). Therefore, a high photocatalytic degradation activity is expected for methylene blue decomposition. Nevertheless, the physical interaction between reactive media and the photocatalyst surface must be explored and analyzed for a better understanding of the photocatalytic process.

### 5.2.3. Point of zero charge

The pH of the solution can play a key role in the adsorption and the photocatalytic degradation of pollutants. The ionization state of the surface of the photocatalyst can be also protonated and deprotonated under acidic and alkaline conditions [12]. Therefore, the point of zero charges (pZc) was investigated for the synthesized materials, as well for zinc oxide, and the obtained results are presented in Figure 19.

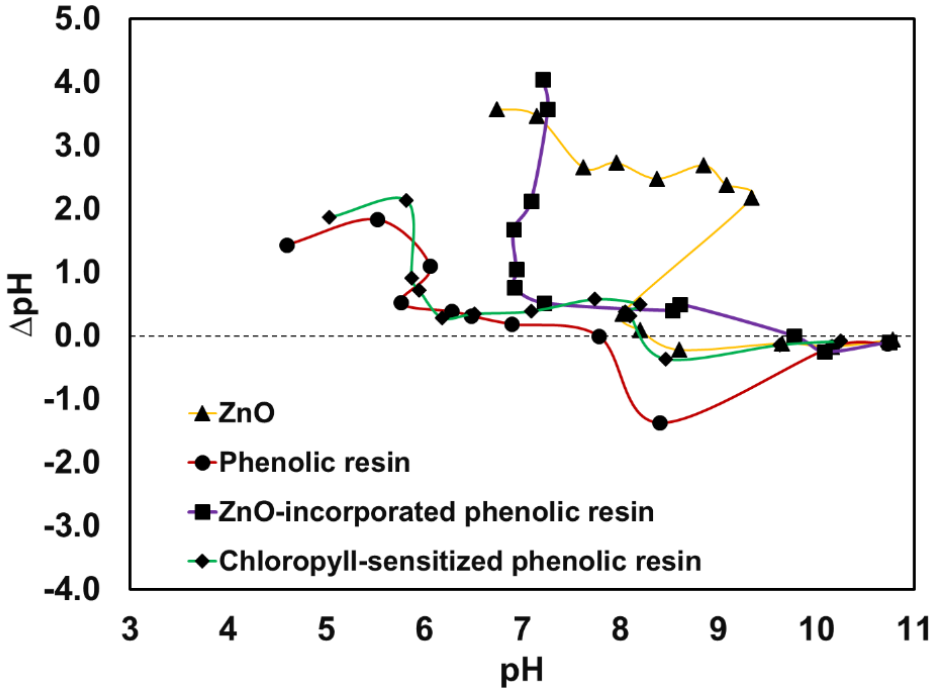


**Figure 19.** Point of zero charges of the studied semiconductors: phenolic resin (R), ZnO-incorporated phenolic resin (R-ZnO), chlorophyll-sensitized phenolic resin (R-C) and zinc oxide (ZnO).

Phenolic resin and chlorophyll-sensitized phenolic resin showed a similar behaviour for the surface charge distribution obtaining a pZc of 7.8 and 8.2, respectively. Under acidic conditions, the positive charge at the surface of the phenolic resin increases as the pH decreases. In contrast, at solution pH values higher than the pZc, the negative charge at the surface will prevail. For methylene blue assessment it is expected a major interaction at higher pH value due to the positively charged methylene blue and, therefore, electrostatic attraction is expected. On the other hand, for R-ZnO a higher pZc is observed in comparison with the unmodified phenolic resins and ZnO, being the pZc equal to 9.8 for R-ZnO and 8.2 for ZnO. This dissimilar result can be attributed to the occupied hydroxyl groups of phenolic resins that can be further ionized at higher pH value due to the phenolic groups. If the phenolic groups are occupied by the ZnO molecules, the surface charge distribution will be changed, avoiding the ionization until pH value higher than 9.8. This issue will decrease the interaction between R-ZnO and the methylene blue molecules. Nevertheless, the high absorption of light observed

before for this semiconductor could enhance the methylene blue degradation, even with poor physical interaction[106].

## *5.3. Adsorption isotherms*

Adsorption isotherms of methylene blue onto the synthesized phenolic resin, composite materials as well as zinc oxide particles, were obtained at different water matrices (Figure 20).

When the acidified tap water was used (Figure 20A), methylene blue adsorption capacity showed a similar behaviour with both modified phenolic resin, reaching about 3 mg/g of maximum adsorption capacity and about 1 mg/g when ZnO and phenolic resin are used. Moreover, a similar behaviour was observed for ZnO-incorporated phenolic resin with deionized water (Figure 20B). However, a clear decrease in the adsorption capacity was determined with the other three materials. Therefore, a non-significant adsorption contribution is expected for the photocatalytic degradation of methylene blue. Nevertheless, despite of the actual contribution of the adsorption process, a physical interaction between methylene blue and the synthesized semiconductors is needed to achieve a well-designed photocatalytic process [85]. Thereby, a low photocatalytic degradation of methylene blue is anticipated when zinc oxide and phenolic resins were employed.

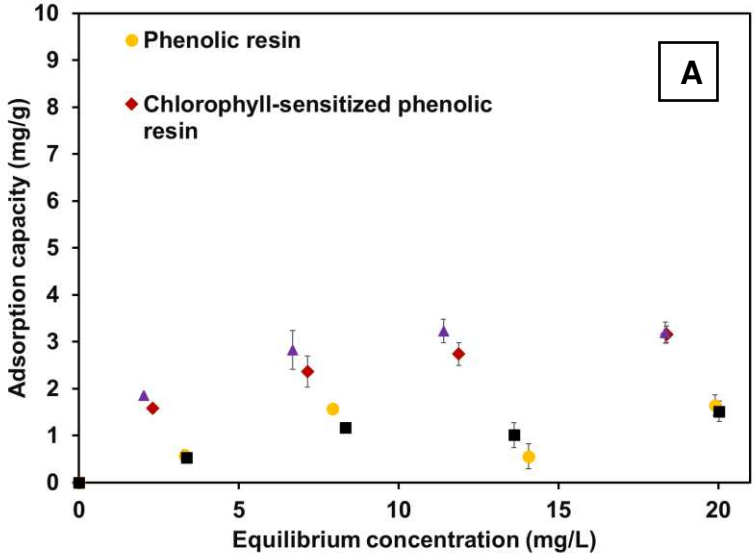

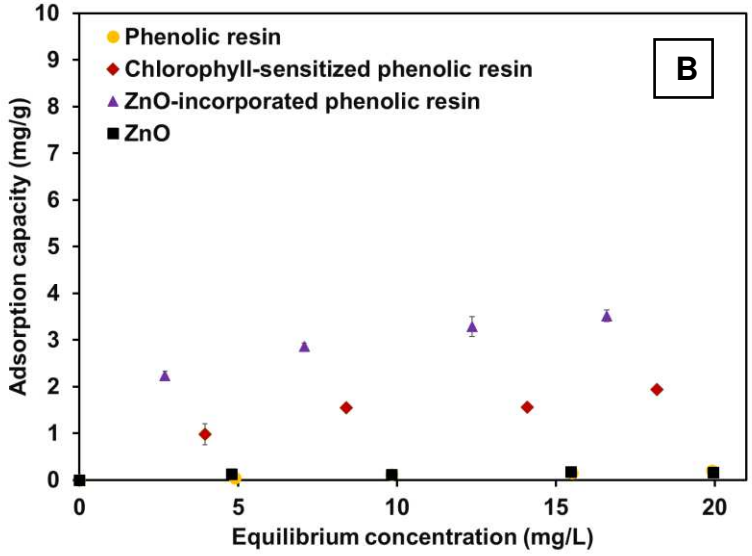
Phenolic resin
Chlorophyll-sensitized phenolic resin
ZnO-incorporated phenolic resin
ZnO
B
Adsorption capacity (mg/g)
Equilibrium concentration (mg/L)
0
1
2
3
4
5
6
7
8
9
10
0
5
10
15
20

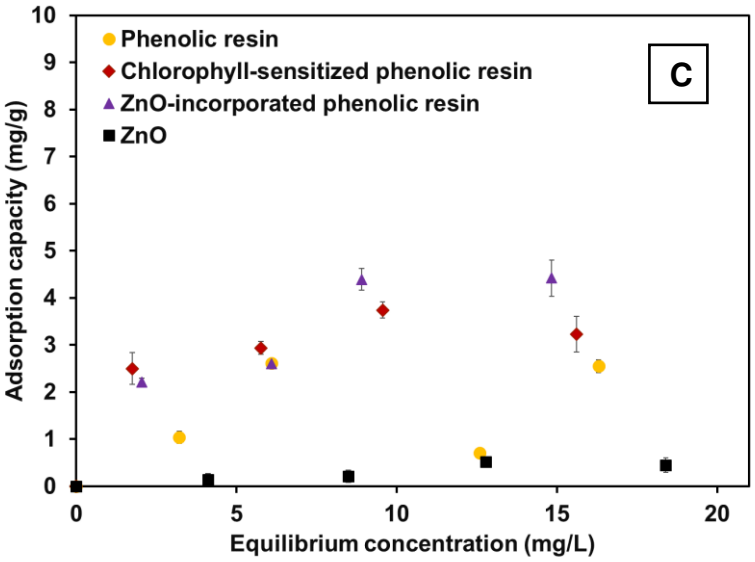
Phenolic resin
Chlorophyll-sensitized phenolic resin
ZnO-incorporated phenolic resin
ZnO
C
Adsorption capacity (mg/g)
Equilibrium concentration (mg/L)
0
1
2
3
4
5
6
7
8
9
10
0
5
10
15
20

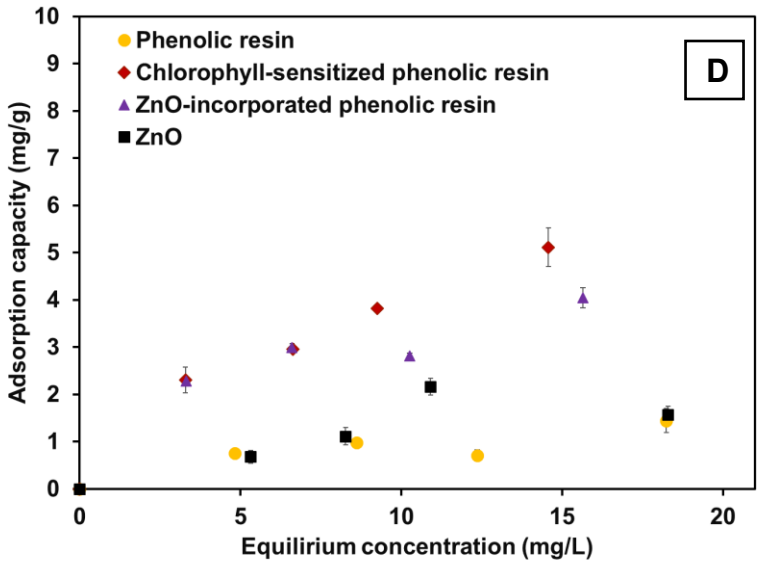


**Figure 20.** Adsorption isotherms of methylene blue onto ZnO and phenolic resins on (A) acidified tap water, (B) deionized water, (C) tap water and (D) alkaline water.

In contrast, an increasing adsorption capacity is achieved with the phenolic resin structures in tap water conditions, achieving about 2-4 mg/g of maximum adsorption capacity, in comparison with the low adsorption capacity obtained for zinc oxide (Figure 20C). According to the point of zero charge determinations (Figure 19), near to the pH of tap water conditions and higher pH (pH>7.7), the surface groups of the studied semiconductors will be ionized with a negative charge, so an increasing adsorption is expected due to the positively charged methylene blue molecules (pka = 3.80). This argument is further validated with the higher adsorption showed in Figure 20C-D. Likewise, the adsorption contribution for the kinetic experiments can be calculated with the equation (141). For instance, at 10 mg/L of initial concentration, the adsorption contribution is 0.1750, 0.2989 and 0.2936 for phenolic resin, ZnO-incorporated phenolic resin, and chlorophyll-sensitized phenolic resin. Furthermore, the adsorption contribution of zinc oxide is about 0.1, which is comparable to the titanium dioxide on similar conditions [22]. This information is also valuable for the photocatalytic process, due to the importance of the quantum yield calculation.

## *5.4. Photocatalytic activity tests*

To compare the photocatalytic activity of the studied semiconductors, kinetic experiments of decolorization were carried out at different operational conditions and the obtained results are shown in Figure 21. The rate of decolorization with the different photocatalyst as well as the photolysis control showed a similar behaviour on the four tested water matrices (Figure 21A). This result could be attributed to the low initial concentration (5 mg/L) employed in this case, because the sum of the adsorption contribution and the photolysis control did not show a clear evidence of a major activity of one of the tested semiconductors.

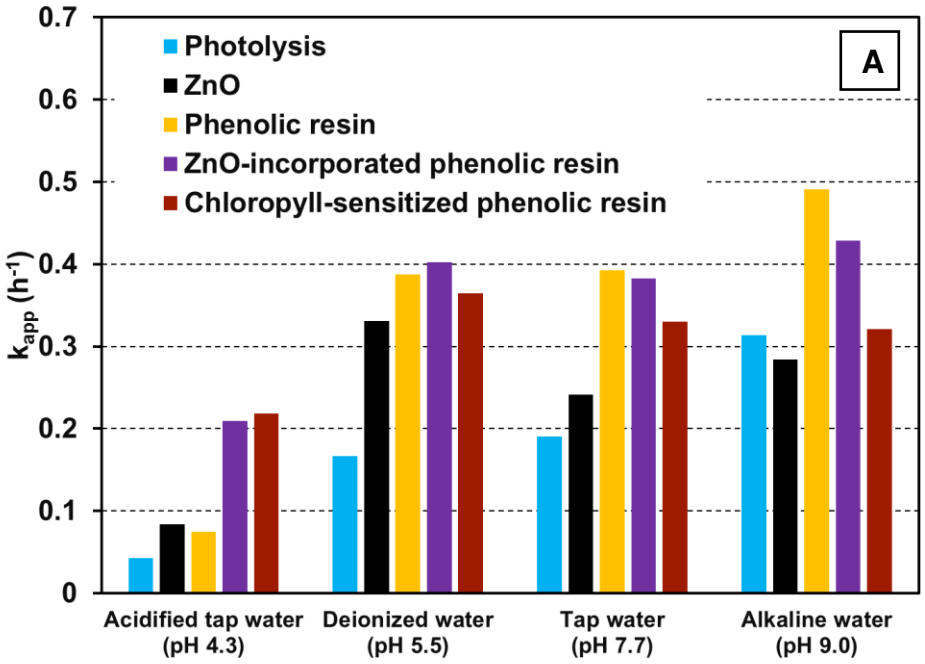

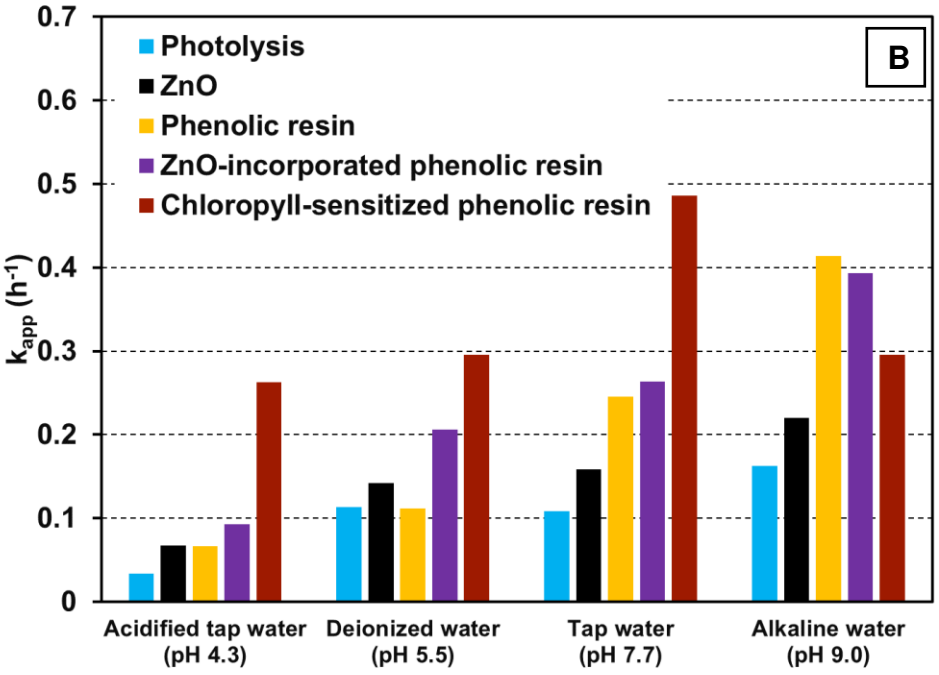
B
Photolysis
ZnO
Phenolic resin
ZnO-incorporated phenolic resin
Chloropyll-sensitized phenolic resin
$k_{app}$ ($h^{-1}$)
0.7
0.6
0.5
0.4
0.3
0.2
0.1
0
Acidified tap water (pH 4.3)
Deionized water (pH 5.5)
Tap water (pH 7.7)
Alkaline water (pH 9.0)

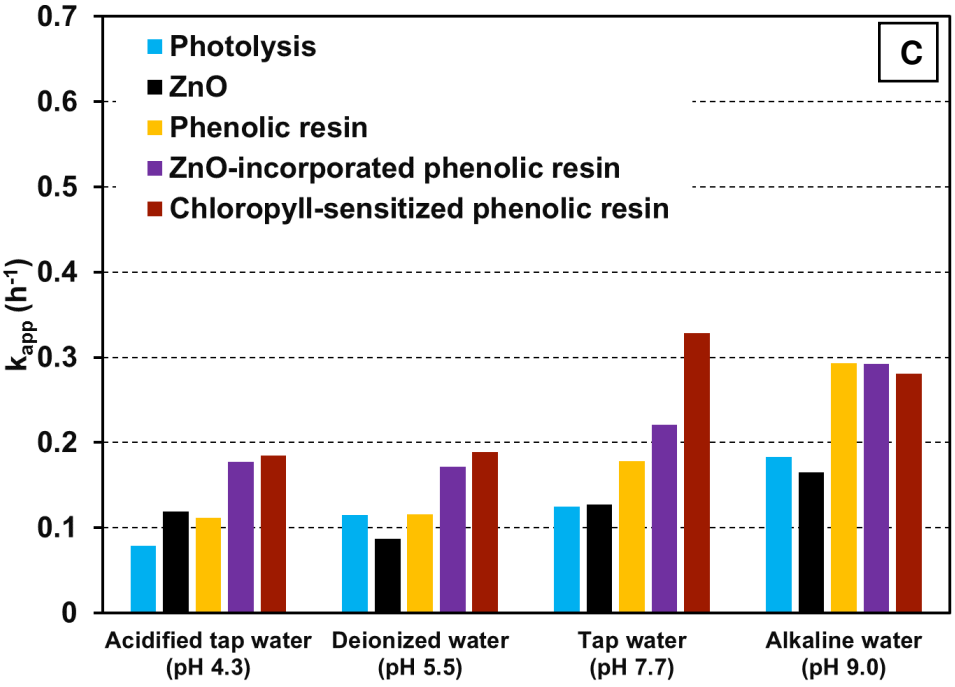
C
Photolysis
ZnO
Phenolic resin
ZnO-incorporated phenolic resin
Chloropyll-sensitized phenolic resin
$k_{app}$ ($h^{-1}$)
0.7
0.6
0.5
0.4
0.3
0.2
0.1
0
Acidified tap water (pH 4.3)
Deionized water (pH 5.5)
Tap water (pH 7.7)
Alkaline water (pH 9.0)

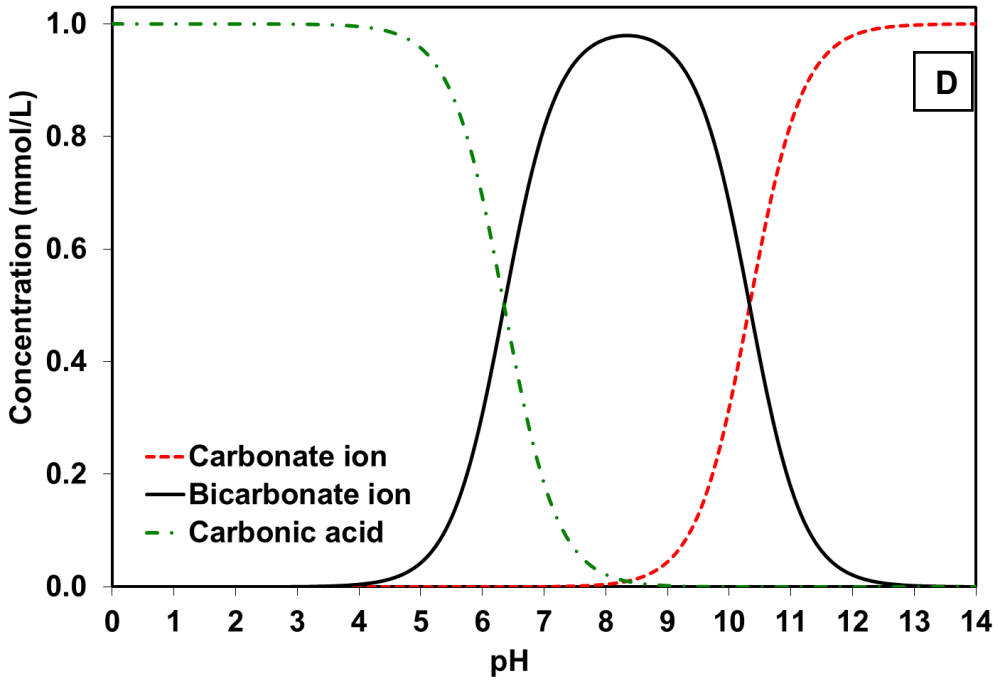


**Figure 21.** Pseudo-first orders kinetic constant of methylene blue decolorization under different water matrices with (A) 5 mg/L, (B) 10 mg/L and (C) 15 mg/L of initial concentration. (D) speciation diagram of carbonate, bicarbonate and carbonic acid species.

However, a notorious effect was observed at a higher initial concentration (Figure 21B-C), being the chlorophyll-sensitized phenolic resin that showed the highest reaction rate constant, followed by ZnO-incorporated phenolic resins, phenolic resin, and ZnO. This last material showed a similar behaviour with the photolysis control at 10 mg/L of initial concentration and a clear inhibition of the methylene blue decolorization at 15 mg/L. As previously discussed, it was expected that zinc oxide shows a low activity because it requires an UV-range photoactivation, compared to the phenolic structures. Besides of this study, decolorization of methylene blue solution was tried with resorcinol-formaldehyde resins (phenolic resin structure) and it demonstrated a good photocatalytic activity, reaching about 40% of decolorization, however the effect of alkalinity was not evaluated [76].

Additionally, phenolic resin and ZnO-incorporated phenolic resins showed an evident increase at alkaline pH values. As discussed in the section 5.1.3, this finding can be attributed to the generation of carbonate anion radical species that could further degrade methylene blue dye in aqueous solution. The higher the

concentration of bicarbonate species, higher the photocatalytic activity (Figure 21D). It is important to notice that the presence of zinc oxide on the phenolic resin enhances the photocatalytic activity of the composite for methylene blue decolorization, being acidified tap water conditions that show the major increase compared to the unmodified phenolic resin. Moreover, a comparable activity is observed in Figure 21B-C at alkaline water conditions. It is suggested that bicarbonate species block the active sites of the ZnO, inhibiting the electron transport through the semiconductor. Previous reports demonstrated the inhibiting effect of bicarbonate species on heterogeneous photocatalysis with metal oxides [28,29]. Therefore, the polymeric semiconductor is the only responsible for the photocatalytic activity at this alkaline condition.

For the decolorization kinetics with chlorophyll-sensitized phenolic resin, the higher photocatalytic activity was obtained with this material in the presence of low alkalinity (pH<7.8), in comparison with the two other phenolic resin structures. However, an important event is observed at pH=9 (moderate alkalinity) with the chlorophyll-sensitized phenolic resin, achieving a lower photocatalytic activity than the other two phenolic resin structures. Because the sensitization was carried out with chlorophyll molecules, the active site of the semiconductor is referred to the magnesium pyrrolic coordination [107]. Even more, carbonate anions could be interacting with the magnesium atoms due to high pH values, generating magnesium carbonate that could precipitate on the surface, blocking the active sites of the semiconductor that further inhibit the photocatalytic activity. Nonetheless, the sensitized photocatalyst showed the highest activity on the other conditions for the decolorization of methylene blue.

Likewise, COD and TOC analysis were carried out for the kinetic experiments at 10 mg/L of initial concentration, and the obtained results are showed in Figure 21. It is interesting that COD removal (Figure 22a) was higher in the presence of ions than in deionized water for the polymeric photocatalyst based on phenolic resins. Moreover, ZnO seems to inhibit the degradation process scavenging the incidence of light on the reaction volume. This behavior is further validated because photolysis control demonstrates a higher COD removal than ZnO experiments,

mainly attributed to the autocatalytic behavior of the methylene blue (as explained before). Furthermore, the ZnO-incorporated phenolic resin proved well-functionality at tap water and alkaline water conditions, reaching about 42% and 27% of COD removal, respectively. On the other hand, phenolic resin photocatalyst showed about 18% of COD removal at deionized water conditions, even higher than the modified phenolic resins. Nevertheless, the chlorophyll-sensitized phenolic resin demonstrated the best performance at alkaline, tap and acidified tap water, reaching about 30%, 60% and 39% of COD removal, respectively, arising as the polymeric semiconductor with the highest photocatalytic activity on the degradation of methylene blue, employed on this study.

Also, TOC analysis (Figure 22b) showed that about 64% of the mineralization of methylene blue was achieved employing the chlorophyll-sensitized phenolic resin at tap and acidified tap water conditions, and about 63% of TOC removal for the ZnO-incorporated phenolic resin at alkaline water conditions. The latter results seem to contradict the COD removal; however, TOC removal is based on the produced carbon dioxide due to mineralization of the organic contaminant and the COD removal is based on the oxygen need for the chemical degradation of the organic contaminant.

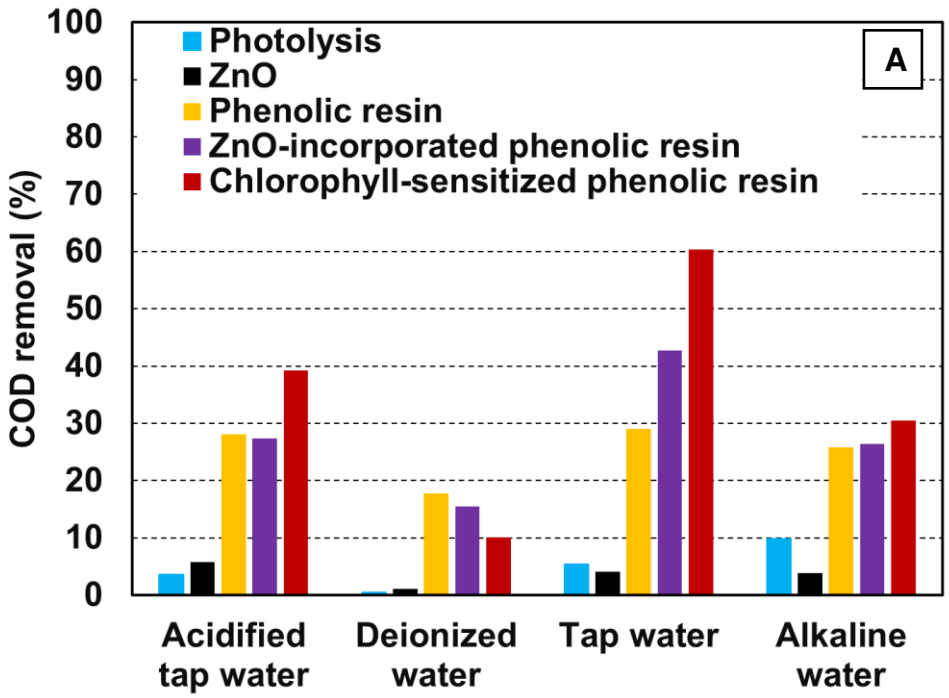

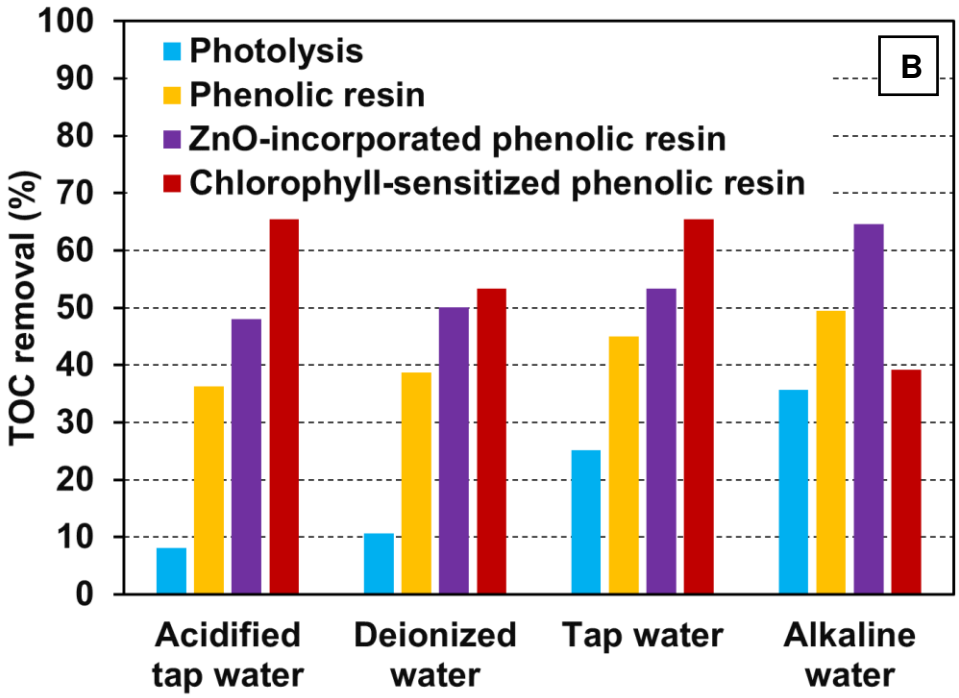


**Figure 22.** a) Chemical oxygen demand and b) Total organic carbon removal of methylene blue under different water matrices, with polymeric photocatalysts based on phenolic resins, ZnO photocatalyst and photolysis control.

Since both represent the degradation of the organic pollutant, the decrease in COD concentration describes the ease with which contaminants could be degraded, unlike the TOC analysis that represents the complete degradation of the organic pollutant. For the previously discussed reasons, the chlorophyll-sensitized phenolic resin appears as the most effective photocatalyst for the degradation of methylene blue, hence the potential usage, for the blue wastewater degradation.To the best of our knowledge, this study evaluates for the first time the photocatalytic activity of a sensitized polymeric semiconductor for the degradation of methylene blue.

## *5.5. Effective photocatalytic mechanism (EPM)*

As previously discussed, organic contaminants can be degraded or transformed by heterogeneous photocatalysis processes. Even more, electrochemical characterization of the synthesized phenolic resins confirmed the feasibility for reactive oxygen species generation via hole oxidation or electron reduction. This

issue is an important information for the application of the generalized kinetic models. As seen in section 3.2, the developed kinetic model based on the reactive oxygen species and electron-hole pair attack, a mechanistic pathway must be specified for a reasonable numerical solution. To assess the role of ROS, the EPM model was proposed and further validated on the different tested conditions, as well as the employed semiconductors. Therefore, taking into account the reactive ionic species due to alkalinity (bicarbonate and carbonate species), acidic conditions were established in order to minimize the presence of bicarbonate species, so the equation (9) can be rewritten as follows:

$$\varphi_{CO_3^{-\cdot}} = \left( \frac{k_{app,pH\,4.3}^{O_2}}{k_{app,control}^{O_2}} \right) \quad \ldots(165)$$

The EPM model results are summarized on Figure 22.

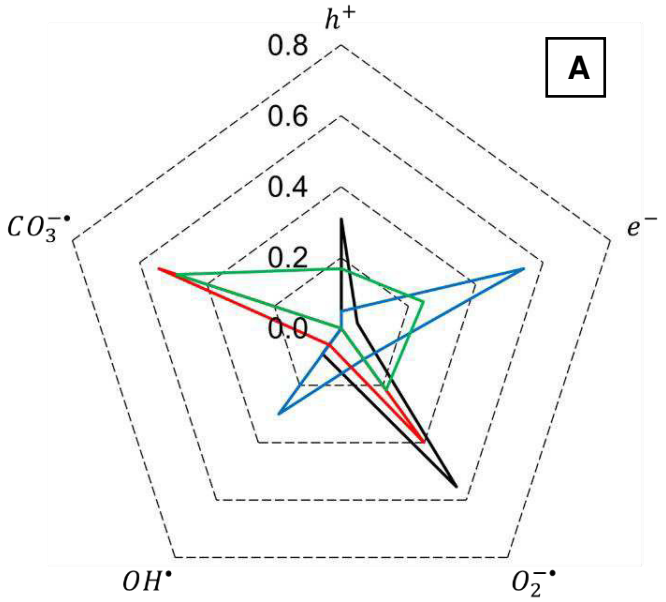

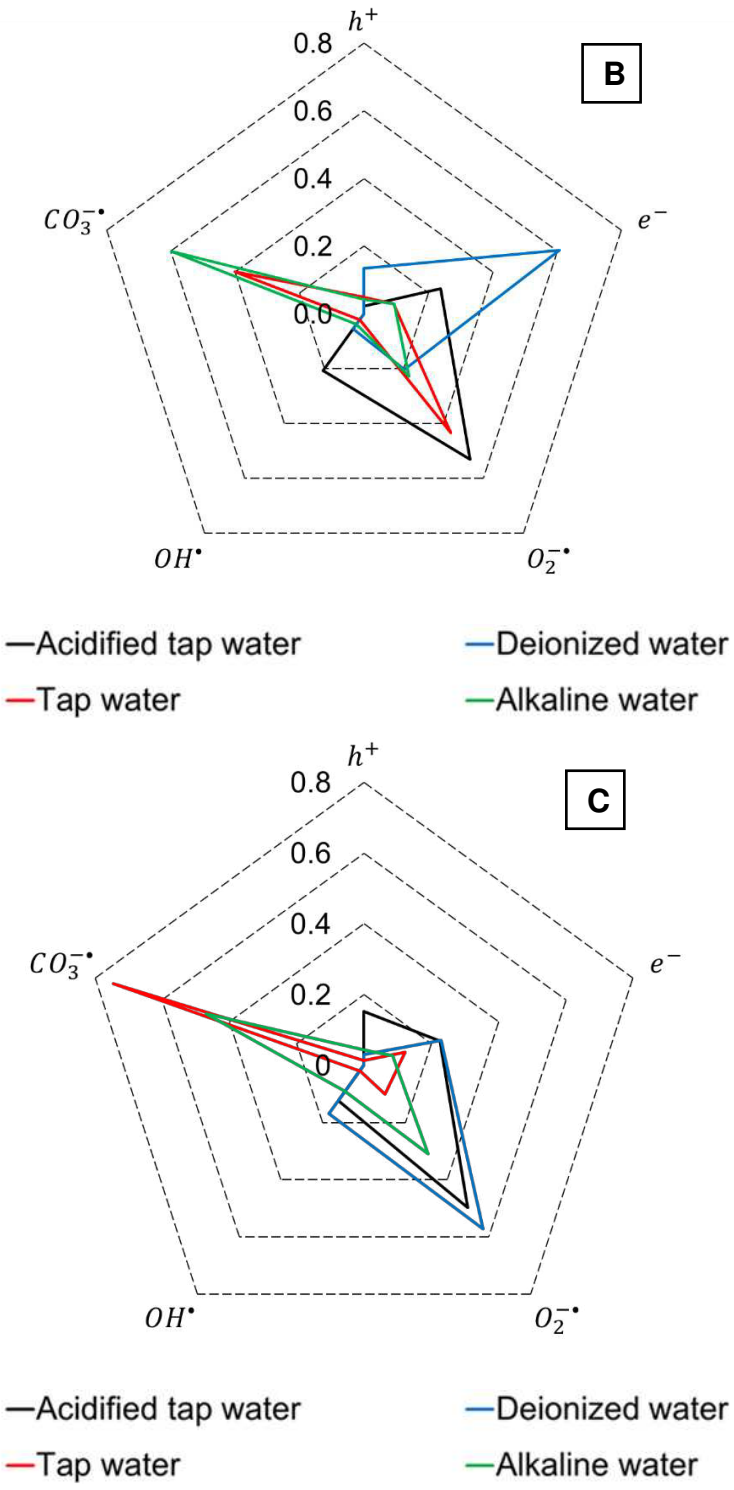


**Figure 23.** Effective photocatalytic mechanism of phenolic resin structures under different water matrices. A) phenolic resin, B) ZnO-incorporated phenolic resin and C) chlorophyll-sensitized phenolic resin.

Phenolic resin photocatalyst showed a dissimilar pathway depending on the water matrix (Figure 23A). Superoxide anion radical showed about 58% of the rate of methylene blue decolorization with the acidified tap water, followed by the direct hole oxidation (~35%) and the balance for the other reactive oxygen species. Moreover, in the lack of ionic species (deionized water), direct electron reduction shows the major contribution (~58%). This considerable change could be attributed to the oxygen usage to the generation of the other reactive oxygen species (*i.e.* hydroxyl radical, hydrogen peroxide). However, these materials cannot generate hydroxyl radical (Figure 7), so hydrogen peroxide selective production may take place (about 35%). On the other hand, and as previously discussed, under the presence of alkalinity, a major carbonate anion radical contribution was observed, being a higher contribution with tap water than alkaline water (58% and 50%, respectively). Even more, superoxide anion radical showed a high contribution at tap water conditions (~40%). This repeated pattern of the contribution of the pair reduction-oxidation process is observed in the previously discussed cases. It is suggested that the generation of oxidative and reductive species could enhance the photocatalytic activity due to inhibition of the recombination process because the electron-hole trapping attributed to the reactive oxygen species. This suggestion is further validated at alkaline water conditions, showing an equilibrated contribution of the oxidation (hole and carbonate anion radical) with the reduction (electron and superoxide anion radical) process. Once the incorporation of the ZnO onto the phenolic resin takes place, more selective mechanisms are observed on the different tested conditions (Figure 23B). It seems that the synthesized heterostructure favored the reduction processes. For instance, the reduction process contribution was equal to 80% of the total contribution in the experiments with acidified tap water and deionized water. This clear enhancement refers to the ligand to metal charge transfer (LMCT) mechanism, where zinc oxide is playing the electron trapping role, and the phenolic resin as the activation site of the photocatalytic process. It is important to mention that previous reports associate the polymeric-metal oxide heterostructures to the LMCT mechanism. However, in this study a lower percentage of metal oxide on the polymeric semiconductor is

used, which is contradictory with the previously proposed materials [37,74,77,102]. For this reason, it is suggested that the reduction process due to electron transport will be favored with heterostructure photocatalyst, despite to the metal-ligand proportion. Besides, the oxidation process selectively attacks methylene blue via carbonate anion radical at alkaline water conditions. As previously discussed, the alkalinity directly affects the photocatalytic process when metal oxides are used as a semiconductor, so carbonate species may be blocking the active site of the zinc oxide, inhibiting the electron transport through the semiconductor lattice, preferring the oxidation process for reactive oxygen species generation.

The sensitized photocatalyst (R-C) showed a similar mechanistic behaviour as the R-ZnO material (Figure 23). Contrary to the LMCT mechanism, dye sensitization depicts the mechanistic pathway in a reverse mode, where the active site for the absorption of light is due to the chlorophyll molecules, and the electron trapping is associated to the polymeric structure of the phenolic resin. It has been demonstrated the high potential of polymeric semiconductor for heterogeneous photocatalysis applications [36,39,76,108,109], related to the $Sp^2$ hybridization. The main characteristic observed on polymeric materials is the electron density around the surface that further interact with electron acceptor compounds. So, electron flow through polymeric lattice may be possible. Although, it seems that a better selectivity is obtained with the dye-sensitized materials (Figure 23C). However, as mention in the previous section, the high concentration of carbonate species inhibited the oxidation process, leading to a slight contribution of the superoxide anion radical mechanism. In summary, the three synthesized semiconductors showed a selective superoxide anion radical attack in acidified tap water and, in the presence of alkalinity, carbonate anion radical leads the attack for methylene blue decolorization.

To the best of our knowledge, this is the first mechanistic analysis conducted for evaluating the photocatalytic degradation process under several operational conditions and different polymeric semiconductors derived from the effective photocatalytic mechanism model, showing a well-functionality for the depiction of the mechanistic contribution.

## *5.6. Generalized kinetic model validation*

Once the mechanistic pathway has been established, a specific case of the proposed kinetic model can be solved. However, the rate of electron-hole pair generation ($R_g$) must be determined before model validation. Some authors have established that $R_g$ is the fraction of the volumetric rate of photon absorption used for the electron-hole pair generation, and this fraction is referred to as the quantum yield of the semiconductor [50,61,89]. Therefore, for the calculation of $R_g$, the volumetric rate of photon absorption and the quantum yield were calculated by the established model showed in section 3.3 and 3.4. In addition, for a better discussion on the modeling section, the summarized results of the characterization of the materials are shown in Table 6.

**Table 6.** Summarized properties of the studied semiconductors.

| Properties | *Semiconductor* | | | |
|---|---|---|---|---|
| | ZnO | R | R-ZnO | R-C |
| $h_r^+$ (V) | - | 2.161 | 2.187 | 2.261 |
| $e_r^-$ (V) | - | -0.167 | -0.351 | -0.231 |
| $E_{gap}$ (eV) | 3.2 | 2.16 | 2.16, 2.53 | 1.75, 2.16 |
| $\overline{\kappa}$ ($m^2/g$)[a] | 30.18 | 19.23 | 40.79 | 61.84 |
| $\overline{\sigma}$ ($m^2/g$)[a] | 229.06 | 36.78 | 80.94 | 123.41 |
| $\overline{\omega}$ ($m^2/g$)[a] | 0.883 | 0.656 | 0.664 | 0.666 |
| $pZc$ | 7.9 | 8.2 | 9.7 | 8.2 |
| $f\left(\mathrm{k}_{ads}\right)$ | 0.0345 | 0.0759 | 0.2989 | 0.2936 |
| $S_g$ ($m^2/g$)[b] | 8.117 | $a_s$ [c] | 1.690 | $a_s$ [c] |

[a] Average values of optical properties calculated from equation 110 to 113. [b] Data obtained by BET analysis. [c] BET analysis does not show a measurable value; R and R-C surface area were calculated as an sphere non-porous ($a_s = 4\pi r^2$) in order to compare to total specific surface area of the synthesized materials

### *5.6.1.Six flux model Henyey-Greenstein analysis (SFM-HG)*

To elucidate the radiative effects on the photocatalytic reaction, SFM-HG was employed taking as reference a tubular reactor as described in section 4.12. First, the incident radiation was calculated integrating the equation (153) along the reactor length, as follows:

$$\int_0^H I_{(\eta R),z}\,dz = \int_0^H \frac{r_1 I_w}{2\eta R}\left[\arctan\left(\frac{2z-H+L}{2\eta R}\right)-\arctan\left(\frac{2z-H-L}{2\eta R}\right)\right]dz \ldots(166)$$

The incident radiation was estimated with the actual reactor data summarized in Table 7. The average value (measured along the reactor length with the visible-light range radiometer) was about 40.63 ± 7.91 W/m$^2$. The calculated value from equation (165) result in an incident radiation equal to 44.89 W/m$^2$, is highly accurate with the measured value. The actual deviation can be attributed to the spatial distribution of light on the irradiation chamber over two tubular reactors, while mathematical model considers a uniform light distribution at one tubular reactor. Nevertheless, both values can be considered for the simulation of the radiant field in the reactor volume.

**Table 7.** Photoreactor specification used in this study.

| Reactor (dimension) | Tubular |
|---|---|
| Material reactor (Unitless) | Borosilicate glass |
| Internal diameter (m) | 0.0254 |
| Thickness (m) | 0.0020 |
| Length per tube* (m) | 1.0 |
| Reaction volume (m$^3$) | 0.001 |
| Total volume of liquid (m$^3$) | 0.007 |

*Two tubes were used in this research.

In a photocatalytic reaction system of the suspended semiconductor, the volumetric distribution of photon absorption in the reaction space is required to determine the overall conversion of the pollutant. Figure 24 shows the spatial distribution of the LVRPA on the tubular reactor calculated by the SFM-HG. As observed in Figure 24, phenolic resin showed a uniform distribution in the reaction space, reaching a maximum value about 1200 $W/m^3$ in the top of the reactor. Furthermore, zinc oxide achieved a rate of photon absorption higher than phenolic resins (about 3500 $W/m^3$). Despite of the high rate of photon absorption, the activation of ZnO can be carried out at UV range [66], thereby a poor generation of reactive oxygen species is expected. As previously discussed, ZnO presented the lowest activity compared to the other three tested semiconductors (Figure 21 and 22). Even more, in some operational conditions, phenolic resins showed a higher activity for the degradation of methylene blue compared to ZnO (Figure 21). To the best of our knowledge, this is the first evidence of a comparison of LVRPA distribution considering the photocatalytic activity, demonstrating that the rate of photon absorption does not directly affect the photocatalytic degradation process, but it plays a major role on the photon distribution inside the reactor (scattering phenomena)[54].

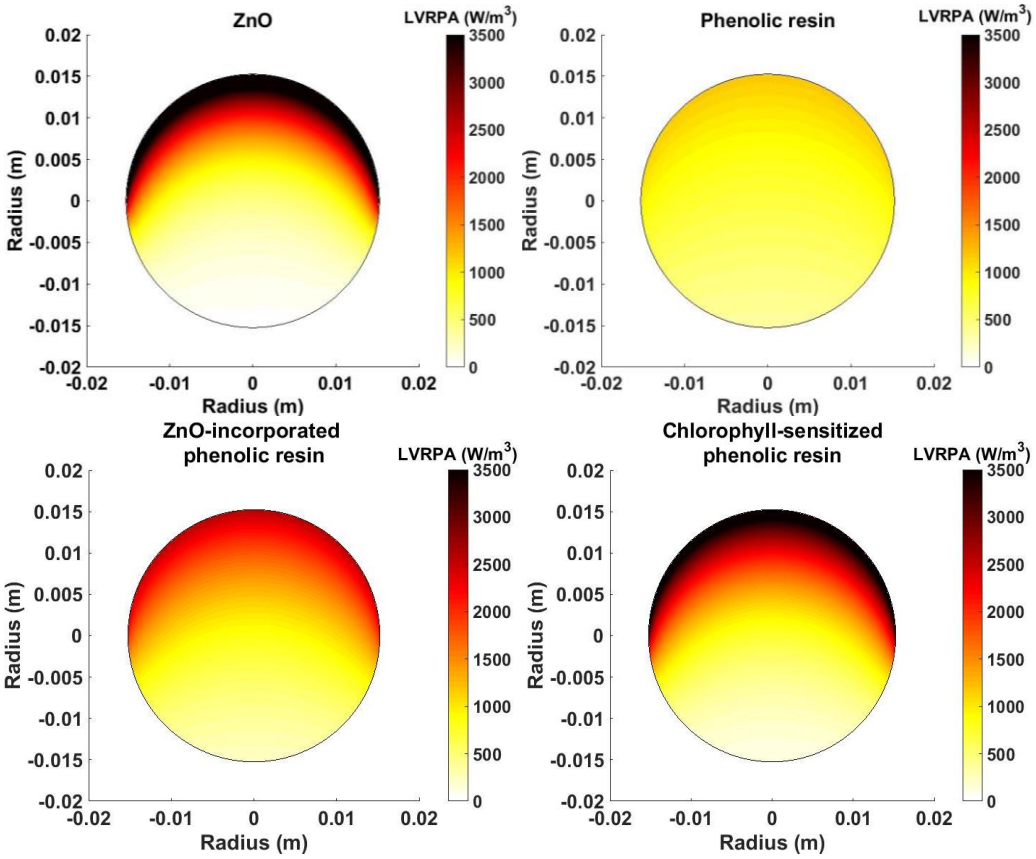


**Figure 24.** LVRPA distribution in a tubular reactor for ZnO and the phenolic resin structures with asymmetry factor, $g = 0$ and catalyst load, $C_{cat}$ = 1 g/L.

On the contrary, the modified phenolic resins showed higher LVRPA values than unmodified phenolic resin, as well as the good distribution of the radiation. The R-ZnO and R-C reach a maximum about 2500 W/m$^3$ and 3500 W/m$^3$, respectively. As above-mentioned, R-ZnO showed a better scattering of light inside the reactor, the R-C also showed a higher absorption that could be harnessed for the activation of the semiconductor due to the visible-light optical characteristics. It is important to notice that the rate of photon absorption is directly related to the absorption phenomena, and the distribution of light is related to the scattering phenomena. Nonetheless, the LVRPA estimation, as well as the OVRPA, can give valuable information related to the reactor geometry and the catalyst loading employed for the photocatalytic process. Likewise, the OVPRA ( $E_\lambda^a$ ) calculation was performed

in order to compare the rate of photon absorption between the studied semiconductors, and the obtained results are shown in Figure 25.

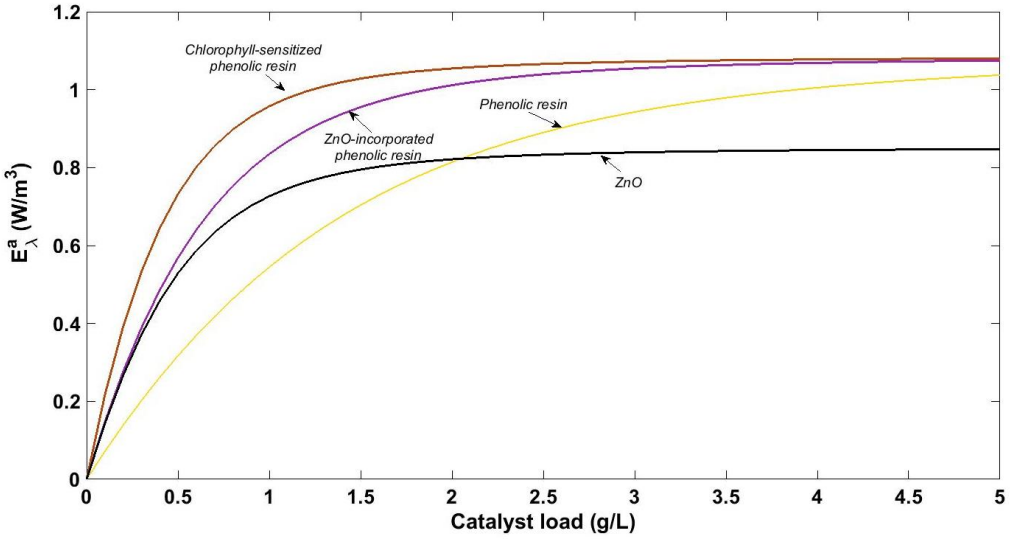


**Figure 25.** Effect of the catalyst loading on the overall volumetric rate of photon absorption ( $E_\lambda^a$ ) for ZnO and the phenolic resin structures.

As observed in Figure 25, ZnO showed a higher rate of photon absorption than phenolic resin in the range of 0-1.75 g/L of catalyst load, but after that value, phenolic resin kept increasing until 1 W/m$^3$. Moreover, an accelerate increasing by the ZnO-incorporated phenolic resin was observed, similar to the ZnO particles. ZnO-incorporated phenolic resin showed a higher rate of photon absorption at any catalyst load, opposite to the observed scattering phenomena (Figure 25). This behaviour suggests that the probability of absorption ($1-\omega$ ) has a higher relevance on the rate of photon absorption than the scattering phenomena. Even more, the chlorophyll-sensitized phenolic resin showed a slight increase in the rate of photon absorption, compared to the R-ZnO. Nevertheless, the photocatalytic activity of the sensitized material was higher than the observed slight increase of the rate of absorption of light. Hence, the quantum yield will dictate the photon energy harness for the activation of the semiconductor. Since the R-C semiconductor presented the best results for both the activity and absorption properties, the effective quantum yield calculations were only carried out for this material because of the high complexity for the evaluation of this parameter.

### *5.6.2. Effective quantum yield*

The quantum yield was estimated with the effective quantum yield model employing the LED 5000K cool white irradiation. The electromagnetic spectrum of the LED lamp emission was split out into four segments (Figure 26) in order to avoid that each spectral power distribution depends on several photon energy values.

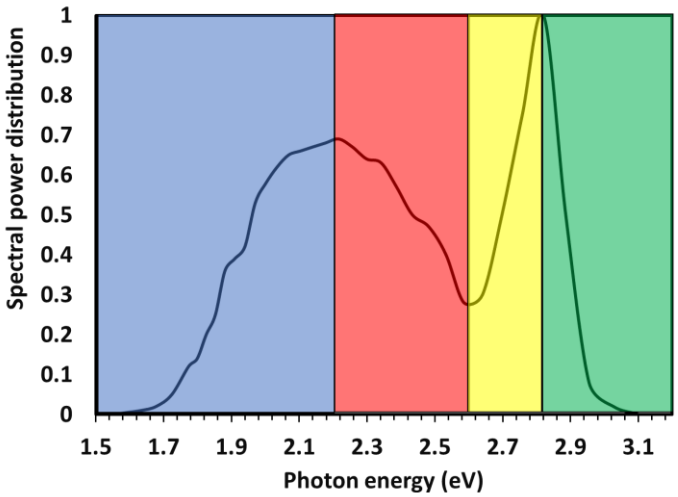


**Figure 26.** LED lamp emission spectral power distribution vs photon energy (colors were arbitrarily chosen to point out the four segments).

For each segment, a calculation of the effective quantum yield was carried out as established in section 3.4. Because the quantum yield estimation relates the photon energy usage of the semiconductor with the irradiation source, a proportional value of the harnessed energy can be defined, based on the probability of absorption. Then, the sum of each proportional contribution determines the effective quantum yield of the semiconductor on the studied emission wavelength. Figure 27 represents the quantum yield dependence of the catalyst load for the chlorophyll-sensitized phenolic resin. Two major increments are observed between 0 and 0.3 g/L. These increments could be attributed to the emission higher intense peaks of the LED lamp observed at 2.2 and 2.8 eV (Figure 27). As the quantum yield depicts the photon energy usage for the activation of the

semiconductor, the maximum peaks of the lamp emission will provoke an enhanced catalyst utilization. As seen in Figure 27, the behaviour of chlorophyll-sensitized phenolic resin showed a major slope between 0 and 0.3 g/L, associated to an equilibrated absorption-scattering mechanism. Likewise, after the increasing behaviour, a slightly decay at 0.1 g/L was observed, as well as a more significant decay at 0.3 g/L, following a similar pattern to the spectral power distribution of the LED lamp. It seems that the most adequate catalyst load for the activation of the semiconductor is about 0.3 g/L.

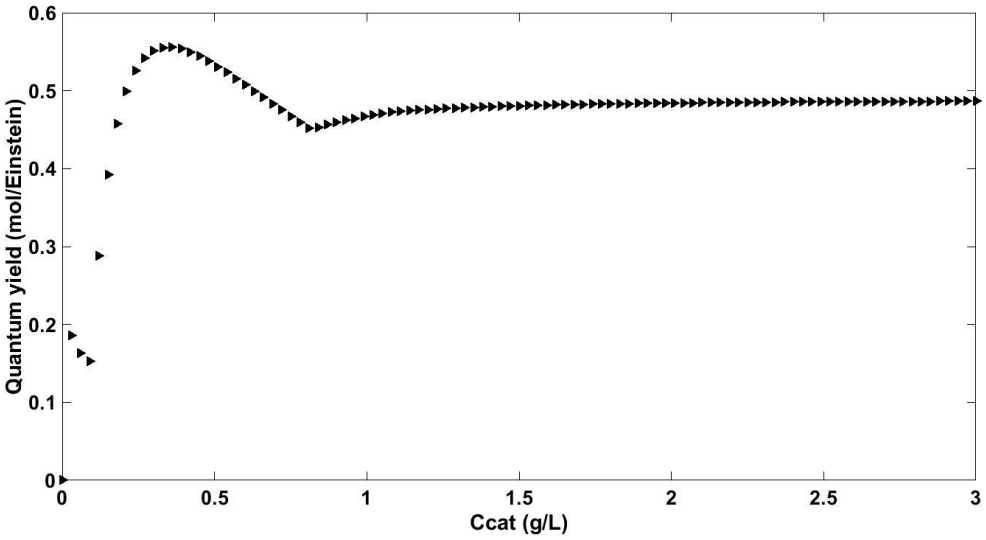


**Figure 27.** Quantum yield estimation for chlorophyll-sensitized phenolic resin on visible-LED irradiation as a function of the catalyst load.

However, the kinetic effects could play an important role due to the available active sites for the photocatalytic process. Even more, the quantum yield does not change for values higher than 1 g/L of the catalyst load, so the validation of the model could not be fairly accurate with those values. Therefore, the rate of electron-hole pair generation was estimated with the obtained results of Figure 26 and 27, in order to observe the rate of activation profile as a function of the catalyst load.

As observed in Figure 28, the rate of generation of electron-hole pair presents three main events. The first one takes into account the linear increase of both the quantum yield and the OVRPA for low catalyst loading (<0.1 g/L). This event

represents the activation step in the presence of low dosage of the photocatalyst where the absorption phenomenon is the main radiative effect. The second event shows an exponential increasing between 0.1 and 0.7 g/L, where the physical-chemical properties of the semiconductor allow the highest yield for its activation (Figure 28). Even more, the scattering phenomenon achieves the best distribution of light on the reactor volume. The final event shows another exponential behaviour, but it only depends on the rate of photon absorption since the quantum yield reached a constant value (~0.47). Finally, the stationary behaviour began to appear about 2 g/L, mainly attributed to the shielding effect that takes place due to the high particle concentration inside the reactor volume, affecting the distribution of light that further diminishes the photon energy usage for the activation of the semiconductor. To the best of our knowledge, this is the first study that shows the rate of generation of the electron-hole pair as a function of the catalyst load. This procedure can be employed for the estimation of the quantum yield, as well as the rate of electron-hole pair generation for any kind of semiconductor.

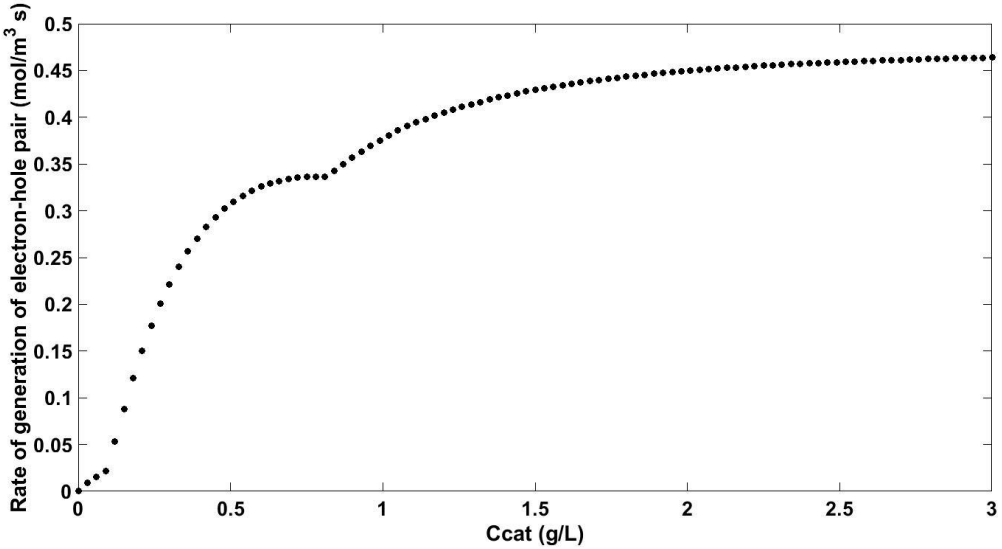


**Figure 28.** The rate of electron-hole pair generation for chlorophyll-sensitized phenolic resin on a tubular reactor under visible-LED irradiation, as a function of the catalyst load.

Once the rate of generation of electron-hole pair is calculated, an arbitrary value is chosen for the validation of the mechanistic pathway, as well as the rate of electron-hole pair can also be validated with the kinetic analysis at different catalyst load,

changing the estimated parameters, holding the kinetic parameters obtained from the numerical solution of the mathematical model. In the following sections, both studies were conducted in order to validate the generalized kinetic model.

### *5.6.3.Kinetic model analysis*

To predict the physicochemical behaviour of the photocatalytic degradation process, a novel kinetic model was developed and showed in section 3.2. This model presented an inherent dependence of the mechanism of the reactive oxygen species attack; however, five cases were established, and the selectivity of the degradation process differs according to the semiconductor and the operational conditions. In section 5.5, the contribution of the reactive species for the attack of an organic pollutant was discussed employing the effective photocatalytic mechanism to elucidate the change in the mechanism with the synthesized phenolic resins structures and its application at different water matrices. Likewise, the modified phenolic resins showed a selective behaviour that enhances the photocatalytic treatment of the methylene blue. Once the photocatalytic degradation was studied, the next step related to the scaling up on the pilot or industrial reactor can be achieved by the kinetic equations (99) and (121-124). However, to carry out a simulation of the operational conditions, the mathematical models must be validated with proper information on different conditions.

The first case of study (electron-hole attack) can be validated with the numerical value of the equilibrium constant of the interfacial charge transfer and the recombination process. In this case, it is expected that the interfacial charge transfer to be lesser than recombination because of the poor or null generation of reactive oxygen species ($\mathrm{K}_{IT}\left(T\right)<1$), signifying that the rate of recombination is high enough to avoid the interfacial charge transfer. According to the Figure 23, the methylene blue photocatalytic degradation with phenolic resins in deionized water matrix, as well as with ZnO-incorporated phenolic resin in deionized water,

showed electron attack as the major mechanistic contribution. Therefore, the validation of the electron attack was carried out with the equation (99) and the kinetic data of the mentioned cases, as well as the rate of electron-hole pair generation was selected arbitrarily from Figure 28 ($R_g = 0.4$) and the properties of the photocatalyst from Table 6. In Figure 29, the model depicts with a high degree of accuracy ($R^2 = 0.945$) of the kinetic data, validating the numerical solution in both cases. Moreover, the equilibrium constants are under unity, $\mathrm{K}_{IT}(T) = 1.4247 \times 10^{-5}$ for phenolic resin, and $\mathrm{K}_{IT}(T) = 1.4437 \times 10^{-5}$ for ZnO-incorporated phenolic resin, validating the previously discussed reasons for poor or null generation of reactive oxygen species.

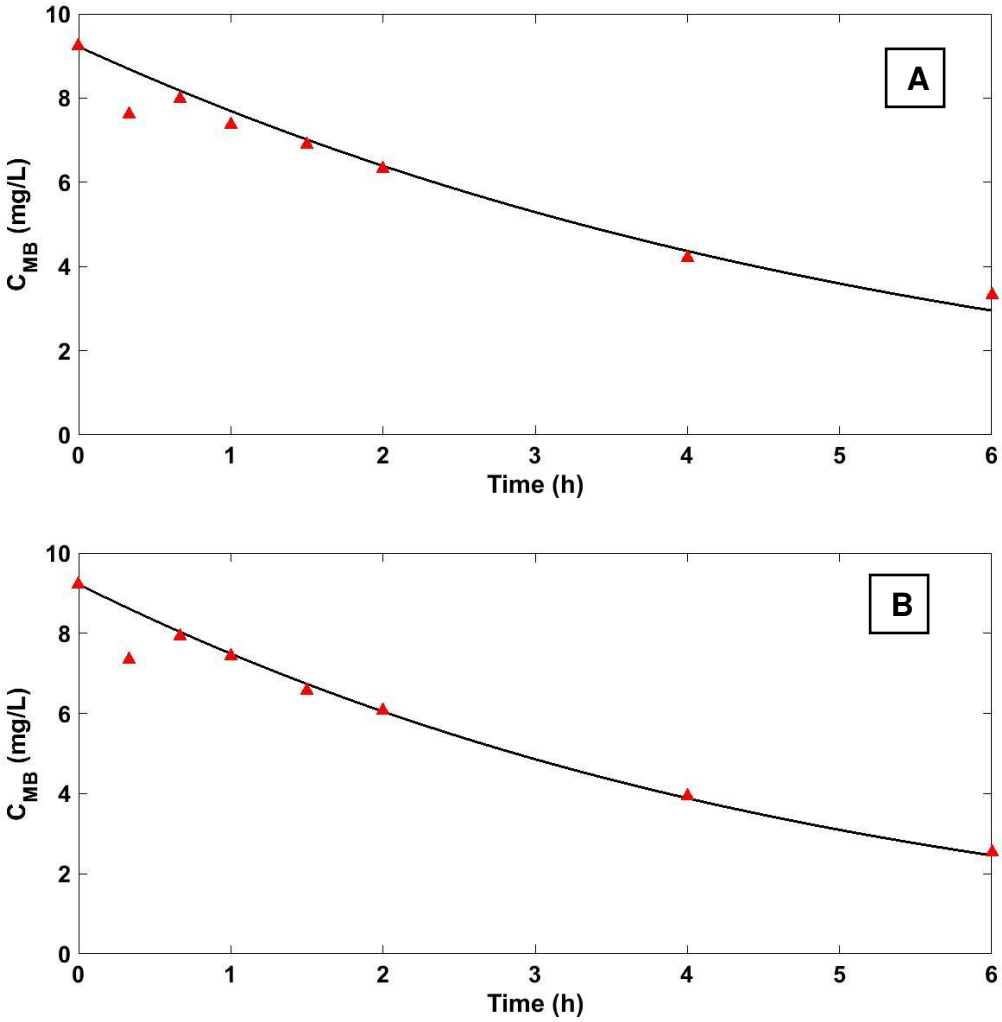

**Figure 29.** Experimental data of the kinetic decolorization of methylene blue in deionized water over time (red filled triangles), and the kinetic model prediction of electron attack (black line) with A) phenolic resin and B) ZnO-incorporated phenolic resin.

The second case of study is related to the reactive oxygen species attack, and contrary to the validation of the first case, it is expected that equilibrium constant value to be over the unity ($\mathrm{K}_{IT}(T)>1$). Likewise, for the equation (121-124) the numerical solution will give three constants values ($\mathrm{K}_{IT}(T)$, $\mathrm{k}_i$ and $\mathrm{k}_A$), so, for a better convergence, the adsorption equilibrium constant will be fixed around $10^{-1}$ to $10^{-3}$ values due to the resulting high degree of accuracy ($R^2>0.9$) with the experimental data. The validation of the anion radical species attack (carbonate and superoxide anion) was carried out with the three phenolic structures on tap water and acidified tap water, and the resulting constant values are presented on Table 8.

**Table 8.** Calculated constant values of the anion radical kinetic models in acidified tap water (ATW) and tap water (TW) for phenolic resin (R), ZnO-incorporated phenolic resin (R-ZnO) and chlorophyll-sensitized phenolic resin (R-C).

| Semiconductor | Water matrix | $\mathrm{K}_{IT}(T)$ | $\mathrm{k}_i$ | $\mathrm{k}_A$ |
|---|---|---|---|---|
| R | ATW | 0.0010 | $2.4318\times10^{-4}$ | 0.0328 |
| R | TW | 1.2379 | $0.27414\times10^{-4}$ | 0.0644 |
| R-ZnO | ATW | 1.2384 | $0.13519\times10^{-4}$ | 0.1288 |
| R-ZnO | TW | 1.2385 | $3.4390\times10^{-4}$ | 0.0013 |
| R-C | ATW | 1.2354 | $0.76114\times10^{-4}$ | 0.0129 |
| R-C | TW | 6.4497 | $1.9841\times10^{-4}$ | 0.0020 |

For phenolic resin, the equilibrium constant was lower than the unity, even though the superoxide anion radical was the main mechanism. However, the holes attack presented a high contribution in the same conditions. It is suggested that there is a competition between the oxidation mechanisms by holes and the reduction mechanism via superoxide radical; therefore, more information is needed for the

selection of the accurate kinetic model. On the other hand, the other calculated constant values validate the employed kinetic model, obtaining $\mathrm{K}_{IT}(T)$ values higher than the unity in all cases. Moreover, the adsorption effect is noticed on the $\mathrm{k}_{A}$, being the adsorption more favorable at lower values. This behaviour was also observed in Figure 20.

Since the model proved well functionality, the next step was to validate in the relation to the concentration of the reactant that further transforms into radical species, as observed on the equations (122-124). Then, controlled experiments were carried out, varying the alkalinity in the reactive media, adjusting the pH values at 5.8, 6.5 and 7.2, and the obtained results are shown in Figure 30. Because a positive effect on the presence of alkalinity (more specific to bicarbonate anions) was obtained, the increasing concentration of these species increased the activity of the methylene blue decolorization. Hence, for the validation of the kinetic model, the obtained results at pH 5.8 were employed for the adjustment of the kinetic parameters, fixing the rate of the electron-hole pair as the previous discussion, and the black line represents the model prediction with the obtained kinetic parameters. Next, the prediction to the higher alkalinity levels is observed as the red and blue line for pH 6.5 and 7.2, respectively. The model prediction represents the kinetic data with a high degree of accuracy ($R^2 = 0.989$), validating the ionic species kinetic model. This information can be employed for the selection of the optimal operating conditions for the selected pollutant with a high degree of accuracy, even for the time prediction for the treatment of specific contaminants (Figure 30). Similarly, the obtained reaction model can be used for the design of photocatalytic reactors.

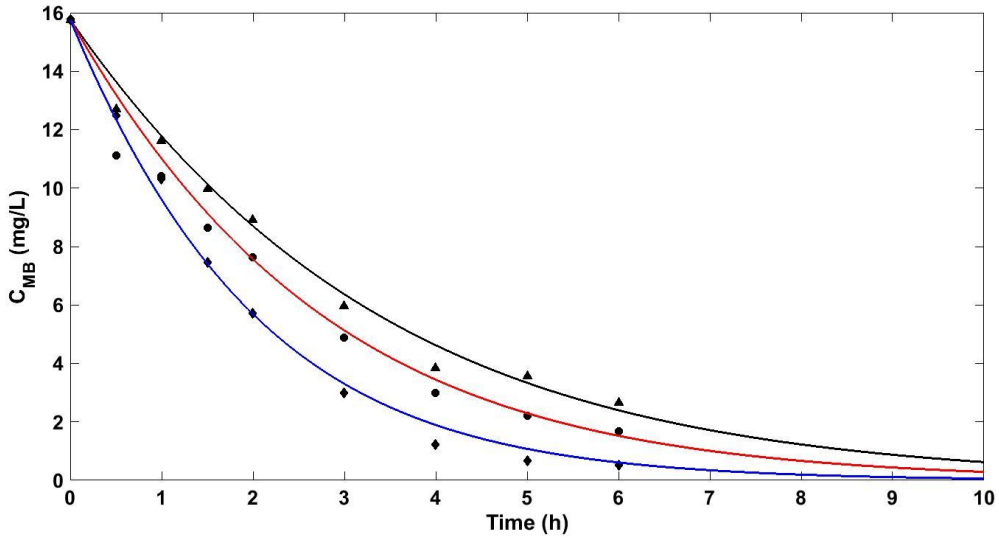


**Figure 30.** Kinetic degradation of methylene blue over time at pH 5.8 (black filled triangles), pH 6.5 (black filled circles) and pH 7.2 (black filled diamonds), as well as the kinetic model adjustment of carbonate anion radical attack at pH 5.8 (black line) and kinetic prediction at pH 6.5 and 5.8 (red and blue line, respectively) with phenolic resin as a semiconductor.

Because validation of the model was conducted for the mechanistic pathway and the concentration of the ionic species that further generates radicals, the last step is to evaluate the effect of the catalyst load and the robustness for complex wastewater. In the following section, decolorization of blue wastewater is discussed in detail employing the chlorophyll-sensitized phenolic resin under TW and ATW.

### *5.6.4. Blue wastewater decolorization*

The photocatalytic decolorization of blue wastewater was carried out following the proposed methodology of section 4.8. Figure 31 shows the photocatalytic decolorization of blue wastewater, measuring the methylene blue concentration over time under tap water conditions at different catalyst load. It is clear that an inhibiting effect is taking place for the decolorization of methylene blue. This could be attributed to the scavenging of the generated reactive species. Because the oxidation pathway is attributed to the carbonate anion radical attack, the blue wastewater components may scavenge the oxidation attack for the methylene blue decolorization. This behaviour prevailed even at high catalyst dosages. No

significant changes were observed, and, for this reason, the kinetic model did not predict the experimental data accurately.

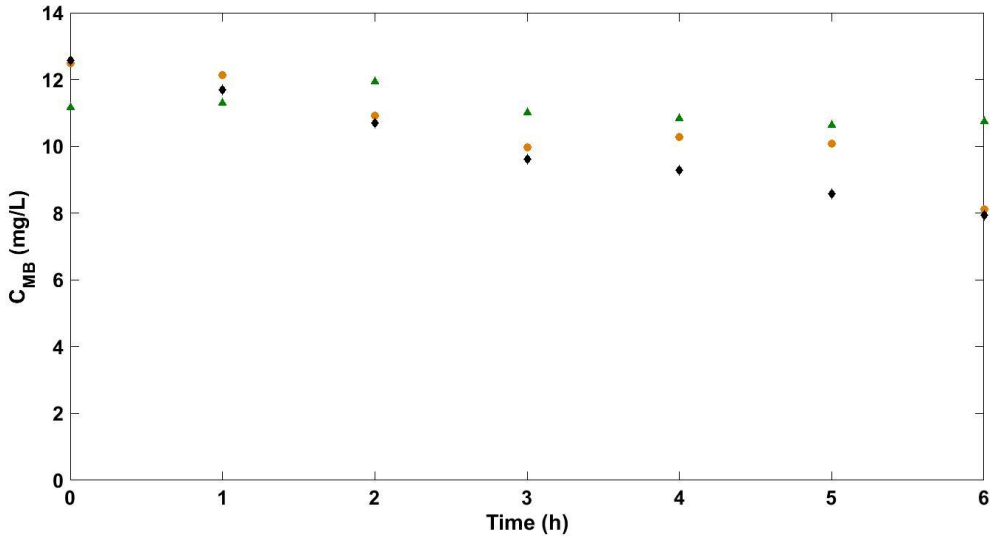


**Figure 31.** Decolorization kinetics of blue wastewater following the methylene blue concentration in tap water conditions with chlorophyll-sensitized phenolic resin dosages of 1 g/L (green filled triangles), 2 g/L (orange filled circles) and 3 g/L (black filled diamonds).

When decolorization kinetics were carried out in acidified tap water conditions, a significant effect in decolorization decay was obtained. As discussed in section 5.5, the mechanistic pathway of R-C presented a selective superoxide anion radical attack, so the prediction of the experimental data was made with the equation (123), and the obtained results are shown in Figure 32.

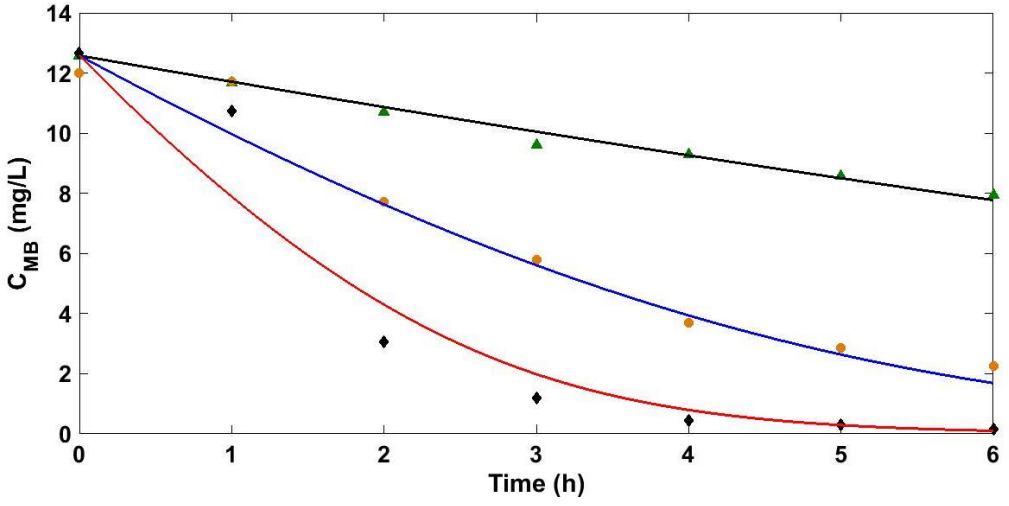

**Figure 32.** Decolorization kinetics of blue wastewater following the methylene blue concentration in acidified tap water conditions with chlorophyll-sensitized phenolic resin dosages of 1 g/L (green filled triangles), 2 g/L (orange filled circles) and 3 g/L (black filled diamonds). Continuous lines represent the kinetic model prediction for superoxide anion radical attack for photocatalyst dosages of 1 g/L (black line), 2 g/L (blue line) and 3 g/L (red line).

The photocatalytic decolorization of blue wastewater showed a remarkable increase with increasing the photocatalyst dosage. This contradictory behaviour of the oxidative and reductive pathway (Figure 31 and 32), suggests that the electron donor-acceptor nature of the pollutant played a major role on the photocatalytic decolorization process. Moreover, the validation of the kinetic model was conducted for the obtained results at 1 g/L of catalyst load, considering the rate of electron-hole pair generation values at the specified catalyst load ($R_g = 0.37$ for 1 g/L). The adjusted parameters showed a markedly increasing of the adsorption equilibrium ($\mathrm{k}_A = 0.1285$), signifying that the adsorption process slightly affects the photocatalytic process due to the complexity of the wastewater, compared to the activity tests of methylene blue. Moreover, an expected decrease of the kinetic constant value was obtained ($\mathrm{k}_i = 1.2271 \times 10^{-5}$), even with the reactive radical species as the main mechanism ($\mathrm{K}_{IT}(T) = 1.2346$). Next, for the prediction at 2 g/L ($R_g = 0.44$), the blue line represents with a high degree of accuracy ($R^2 = 0.961$) the experimental data (orange filled circles). In fact, the prediction at 3 g/L ($R_g = 0.46$) follows the same performance with a high degree of accuracy ($R^2 = 0.939$), validating the robustness of the model. The above-discussed analysis represents the full validation of the generalized kinetic model considering the radiative effects for the activation of the semiconductor, the mechanistic pathway of the reactive oxygen species attack and the classic heterogenous catalysis phenomena.

## 5.7. *Modeling and prediction of the visible-LED tubular reactor for blue wastewater treatment*

The photocatalytic performance of the visible-LED tubular reactor was evaluated under acidified tap water conditions with two borosilicate glass tube with 0.0254 m of internal diameter. The treatment volume was fixed on 7 L with an illuminated volume of 1 L, using a centrifugal pump of ½ hp with a volumetric flow about 27 L/min. The evaluated catalyst dosage was about 1 g/L and the obtained results, as well as the parameter optimization and further simulation is showed in Figure 33. A notorious loss of activity was observed on the decolorization of MB present on synthetic blue wastewater (Figure 33).

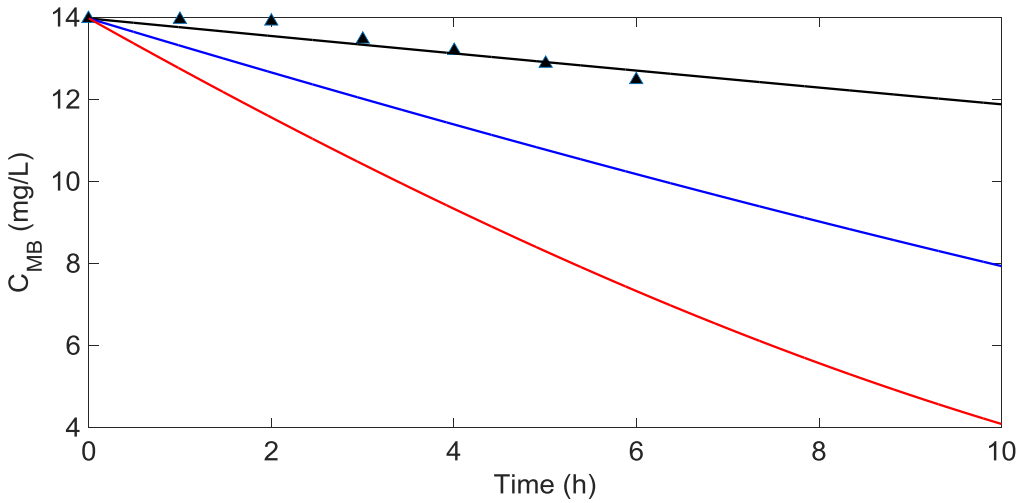


**Figure 33.** Decolorization kinetics of synthetic blue wastewater following the methylene blue concentration in acidified tap water conditions with chlorophyll-sensitized phenolic resin dosages of 1 g/L (orange filled circles) on a visible-LED irradiated tubular reactor with one pump array. Continuous lines represent the kinetic model prediction for superoxide anion radical attack for photocatalyst dosages of 1 g/L (black line), 2 g/L (blue line) and 3 g/L (red line).

The authors suggest that this behaviour could be attributed to the poor dispersion of the catalyst on the tubular reactor that further minimize the photon transport through the reactor volume. Nonetheless, the simulation of a higher catalyst dosage was conducted in order to predict the photocatalytic decolorization of MB. The parameter optimization gave an equilibrium constant above unity (

$K_{IT}(T) = 1.2350$), confirming the superoxide radical attack mechanism, as previously discussed in the section 5.6. However, the prediction at 2 and 3 g/L of catalyst dosage does not achieve a full decolorization, even after 10 h of treatment. Nevertheless, in order to enhance the photocatalytic treatment of synthetic blue wastewater, an array of two pumps in series were employed, increasing the dispersion of the catalyst on the reactor volume. A run of 3 g/L of catalyst dosage was used for the photocatalytic degradation of synthetic blue wastewater. Figure 34 show the kinetic behaviour of the one pump array with 1 g/L and the two pumps in series array with 3 g/L of the catalyst. The parameter optimization was performed for this condition, and a simulation at 1 and 2 g/L was carried out, observing a little increasing on the photocatalytic decolorization of MB compared to the experimental data of the one pump array.

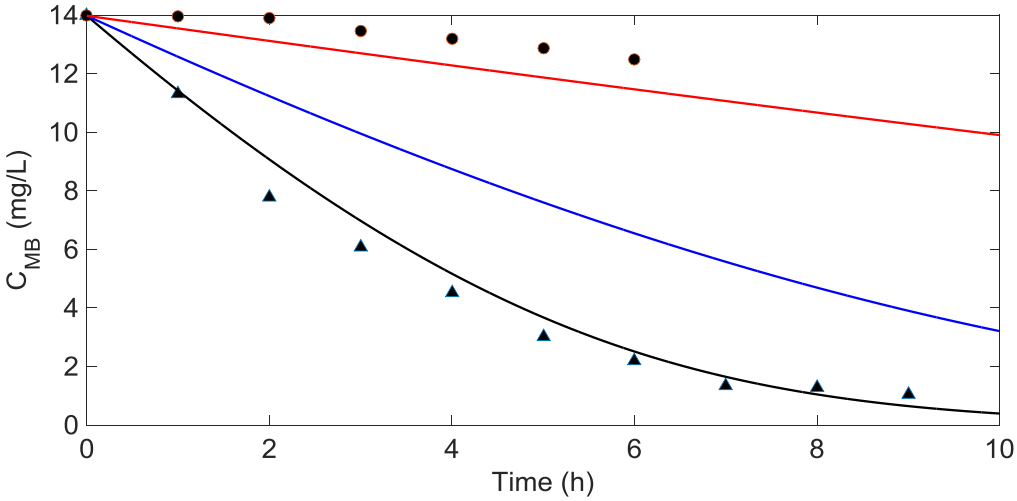


**Figure 34.** Decolorization kinetics of synthetic blue wastewater following the methylene blue concentration in acidified tap water conditions with chlorophyll-sensitized phenolic resin dosages of 1 g/L (orange filled circles) with one pump array and 3 g/L (blue filled triangles) with two pumps in series array on a visible-LED irradiated tubular reactor. Continuous lines represent the kinetic model prediction for superoxide anion radical attack for photocatalyst dosages of 3 g/L (black line), 2 g/L (blue line) and 1 g/L (red line).

An increased photocatalytic activity is observed, confirming the suggestion of the catalyst dispersion. As the flow rate does not change with the pumps in series array, the hydraulic load may be displacing the particles more easily. As the mass

balance considers fluid statics equation, fluid dynamic model must be stablished for the relation of the hydraulic load on the catalyst dispersion. The addition of the behaviour into the mass balance could improve the prediction of the generalized kinetic model.

The kinetic degradation of synthetic blue wastewater was followed for 9 h and the obtained results are shown in Figure 35. The photocatalytic decolorization of methylene blue reached about 92%, as well as the TOC analysis showed near of 40% of TOC removal, confirming a degradation mechanism on the photocatalytic treatment of synthetic blue wastewater.

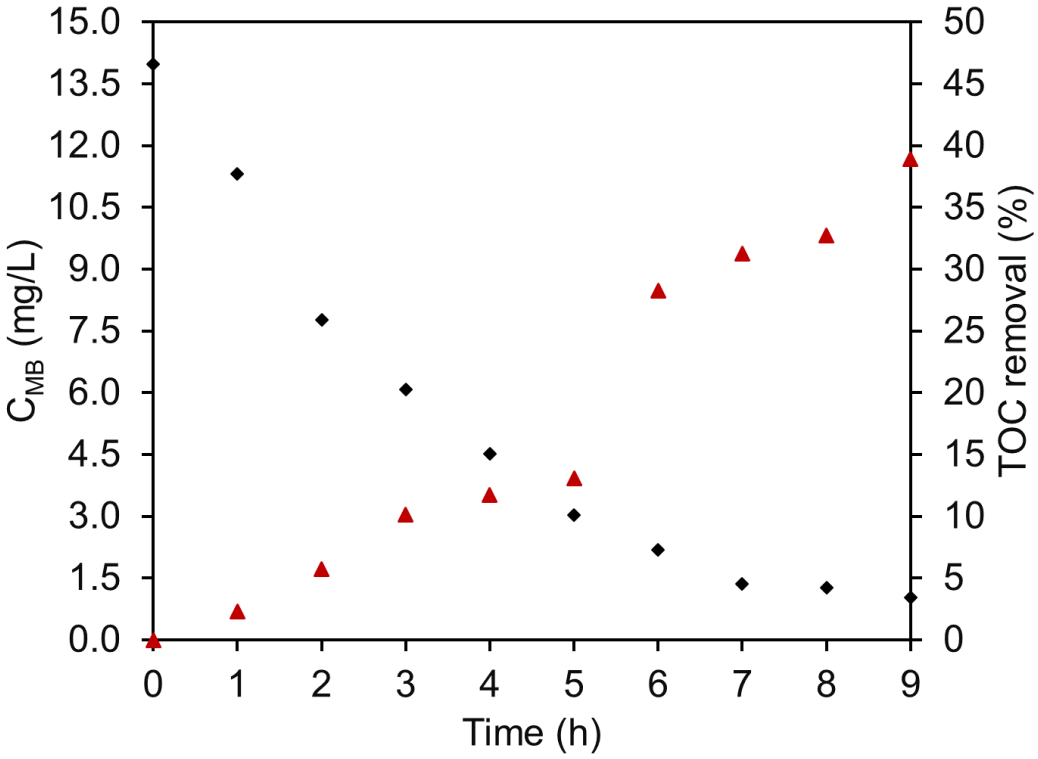


**Figure 35.** Photocatalytic treatment of synthetic blue wastewater with 3 g/L of chlorophyll-sensitized phenolic resin as a semiconductor on a visible-LED irradiated tubular reactor. Decolorization of methylene blue (black filled diamonds) and TOC removal (red filled triangles).

As the synthetic blue wastewater contains methylene blue and other sanitizing compounds, the TOC removal can be inhibited in comparison to the previous observed results (section 5.4), demonstrating its complexity for the wastewater treatment. Because the photocatalytic process did not achieve a complete

mineralization, it is recommended to apply another treatment in order to remediate the synthetic blue wastewater. This study showed a well approximation for the utilization of heterogenous photocatalysis as a pre-treatment of blue wastewater. Likewise, further experiments can be carried out to predict the actual behaviour of the blue wastewater degradation. This work also demonstrated for the first-time a possible pre-treatment for the blue wastewater. Additionally, the kinetic model showed well-functionality even with changes on the pressure drop on a visible-LED irradiated tubular reactor. Finally, it is important to mention that the kinetic model depends intrinsically on the radiation-absorption phenomenon and, for this reason, prediction with the developed model could be extended for solar photocatalysis as a sustainable proposal for the pre-treatment of blue wastewater. Nevertheless, the modeling and further experimentation for the validation of this affirmation are beyond the scope of this project.

# 6. Conclusions

Three novel materials based on phenolic resins were proposed for photocatalytic degradation process. The synthetized materials showed excellent electronic and optical properties, being able to be activated with visible-light. The chlorophyll-sensitized phenolic resins showed the highest photocatalytic activity for the degradation of methylene blue compared to the other phenolic resin structures. For the first time, a generalized kinetic model is proposed in this research and takes into account the generation of the electron-hole pair and the reactive oxygen species via redox reactions, as well as the attack of the reactive species to the pollutant. Furthermore, the photocatalytic degradation mechanism via reactive species was studied with the proposed effective photocatalytic model, showing the specific contribution of the generated reactive species, as well as a changing mechanism for phenolic resin photocatalyst at different operational conditions. Likewise, the phenolic resin structures achieve a satisfactory performance in the presence of the alkalinity, establishing it as the only kind of photocatalytic materials stable in alkaline conditions reported in the literature. In addition, the modified phenolic resin shows a selective attack via anion radical species with both oxidation and reduction pathway (carbonate and superoxide anion radical, respectively), giving an adequate information for the implementation of the proposed generalized kinetic model. Also, it is important to mention that this research also presents for the first time a wide discussion about the rate of photon absorption in comparison with the photocatalytic activity for polymeric semiconductors. The quantum yield calculation was carried out with a modification of a previously proposed model, considering any type of semiconductor and source of irradiation. This estimation allows elucidating the dependence of quantum yield, as well as the rate of electron-hole pair generation as a function of the catalyst load, being an important parameter for the well-designed photocatalytic reactors. The radiative transport, as well as the adsorption equilibria information, allows evaluating the proposed generalized kinetic model under several operational conditions, validating its robustness for photocatalytic reaction engineering.

The chlorophyll-sensitized phenolic resin showed the highest methylene blue decolorization (about 98% in 6 h) on the blue wastewater assessment under acidified tap water with a catalyst load of 3 g/L on a full irradiated stirred tank reactor. Moreover, the photocatalytic treatment on a visible-LED irradiated tubular reactor showed a direct dependency of the hydraulic load with the catalyst dispersion. Fluid dynamic modeling must be added in order to increase the accuracy of the generalized kinetic model. The two pumps in series array with 3 g/L of catalyst dosage showed the highest degradation of methylene blue on the tubular reactor, reaching about 92% of decolorization and near 40% of TOC removal. This study demonstrated that the photocatalytic process with visible-LED irradiation could be employed as a pre-treatment of blue wastewater. Finally, the generalized kinetic model arises as the key for the design of light-assisted reactors, but further implementation of other geometries and sources of irradiation needs to be studied in order to trustworthy the application of photocatalytic degradation process at scaled up systems.

# 7. References


[1] D.K. Yeruva, S. Jukuri, G. Velvizhi, A.N. Kumar, Y. V Swamy, S.V. Mohan, Integrating sequencing batch reactor with bio-electrochemical treatment for augmenting remediation efficiency of complex petrochemical wastewater, Bioresource Technology. 188 (2015) 33–42.

[2] I. Metcalf & Eddy, Wastewater engineering : treatment and reuse, Fourth edition / revised by George Tchobanoglous, Franklin L. Burton, H. David Stensel. Boston : McGraw-Hill, [2003] ©2003, n.d. https://search.library.wisc.edu/catalog/999935704402121.

[3] C. Ramos, M.E. Suárez-ojeda, J. Carrera, Biodegradation of a high-strength wastewater containing a mixture of ammonium, aromatic compounds, and salts with simultaneous nitritation in an aerobic granular reactor, Process Biochemistry. 51 (2016) 399–407.

[4] D. Olivo-Alanis, R.B. Garcia-Reyes, L.H. Alvarez, A. Garcia-Gonzalez, Mechanism of anaerobic bio-reduction of azo dye assisted with lawsone-immobilized activated carbon, Journal of Hazardous Materials. 347 (2018). doi:10.1016/j.jhazmat.2018.01.019.

[5] L.H. Alvarez, I.C. Arvizu, R.B. García-Reyes, C.M. Martinez, D. Olivo-Alanis, Y.A. Del Angel, Quinone-functionalized activated carbon improves the reduction of congo red coupled to the removal of p-cresol in a UASB reactor, Journal of Hazardous Materials. 338 (2017). doi:10.1016/j.jhazmat.2017.05.032.

[6] S.M. Amorim, M.T. Kato, L. Florencio, S. Gavazza, Influence of redox mediators and electron donors on the anaerobic removal of color and chemical oxygen demand from textile effluent, Clean - Soil, Air, Water. 41 (2013) 928–933. doi:10.1002/clen.201200070.

[7] G. Lofrano, S. Meriç, G. Emel, D. Orhon, Chemical and biological treatment technologies for leather tannery chemicals and wastewaters : A review, Science of the Total Environment. 462 (2013) 265–281.

[8] Applied Surface Science Energy and environmental photocatalytic materials,

391 (2017) 4332.

[9] X. Zhang, G. Li, Y. Wang, Microwave assisted photocatalytic degradation of high concentration azo dye Reactive Brilliant Red X-3B with microwave electrodeless lamp as light source, Dyes, and Pigments. 74 (2007) 536–544. doi:10.1016/j.dyepig.2006.03.012.

[10] D.S. Bhatkhande, V.G. Pangarkar, A. a C.M. Beenackers, Photocatalytic degradation of nitrobenzene using titanium dioxide and concentrated solar radiation: chemical effects and scaleup., Wat. Res. 37 (2003) 1223–1230. doi:10.1016/S0043-1354(02)00490-6.

[11] J. Colina-Márquez, F. Machuca-Martínez, G. Li Puma, Photocatalytic mineralization of commercial herbicides in a pilot-scale solar CPC reactor: Photoreactor modeling and reaction kinetics constants independent of the radiation field, Environmental Science and Technology. 43 (2009) 8953–8960. doi:10.1021/es902004b.

[12] S. Ahmed, M.G. Rasul, R. Brown, M.A. Hashib, Influence of parameters on the heterogeneous photocatalytic degradation of pesticides and phenolic contaminants in wastewater: a short review., Journal of Environmental Management. 92 (2011) 311–30. doi:10.1016/j.jenvman.2010.08.028.

[13] G.J. Lee, Y.C. Zheng, J.J. Wu, Fabrication of hierarchical bismuth oxyhalides (BiOX, X = Cl, Br, I) materials and application of photocatalytic hydrogen production from water splitting, Catalysis Today. 307 (2018) 197–204. doi:10.1016/j.cattod.2017.04.044.

[14] Y. Sun, X.F. Wang, G. Chen, C.H. Zhan, O. Kitao, H. Tamiaki, S. ichi Sasaki, Near-infrared absorption carboxylated chlorophyll-a derivatives for biocompatible dye-sensitized hydrogen evolution, International Journal of Hydrogen Energy. 42 (2017) 15731–15738. doi:10.1016/j.ijhydene.2017.04.265.

[15] N. Manfredi, M. Monai, T. Montini, F. Peri, F. De Angelis, P. Fornasiero, A. Abbotto, Dye-Sensitized Photocatalytic Hydrogen Generation: Efficiency Enhancement by Organic Photosensitizer-Coadsorbent Intermolecular Interaction, ACS Energy Letters. 3 (2018) 85–91.

doi:10.1021/acsenergylett.7b00896.

[16] G. Iervolino, V. Vaiano, D. Sannino, L. Rizzo, V. Palma, Enhanced photocatalytic hydrogen production from glucose aqueous matrices on Ru-doped LaFeO3, Applied Catalysis B: Environmental. 207 (2017) 182–194. doi:10.1016/J.APCATB.2017.02.008.

[17] P. Chowdhury, H. Gomaa, A.K. Ray, Sacrificial hydrogen generation from aqueous triethanolamine with Eosin Y-sensitized Pt/TiO2photocatalyst in UV, visible and solar light irradiation, Chemosphere. 121 (2015) 54–61. doi:10.1016/j.chemosphere.2014.10.076.

[18] M.A. Mueses, F. Machuca-Martinez, G. Li Puma, Effective quantum yield and reaction rate model for evaluation of photocatalytic degradation of water contaminants in heterogeneous pilot-scale solar photoreactors, Chemical Engineering Journal. 215–216 (2013) 937–947. doi:10.1016/j.cej.2012.11.076.

[19] Y. Ye, H. Bruning, D. Yntema, M. Mayer, H. Rijnaarts, Homogeneous photosensitized degradation of pharmaceuticals by using red light LED as light source and methylene blue as photosensitizer, Chemical Engineering Journal. 316 (2017) 872–881. doi:10.1016/j.cej.2017.02.053.

[20] A. Toumazatou, M.K. Arfanis, P.A. Pantazopoulos, A.G. Kontos, P. Falaras, N. Stefanou, V. Likodimos, Slow-photon enhancement of dye sensitized TiO2 photocatalysis, Materials Letters. 197 (2017) 123–126. doi:10.1016/j.matlet.2017.03.128.

[21] A.E. Cassano, C.A. Martin, R.J. Brandi, O.M. Alfano, Photoreactor Analysis and Design: Fundamentals and Applications, Industrial & Engineering Chemistry Research. 34 (1995) 2155–2201. doi:10.1021/ie00046a001.

[22] M.A. Mueses, F. Machuca-martínez, Molecular adsorption model for organic compounds over - P25 by protonic distribution affinity Modelo de adsorción molecular para compuestos orgánicos sobre TiO ^ - P25 mediante el método de afinidad protónica, 209 (2013) 201–209.

[23] S. Dong, J. Feng, M. Fan, Y. Pi, L. Hu, X. Han, M. Liu, J. Sun, J. Sun, Recent developments in heterogeneous photocatalytic water treatment using visible

light-responsive photocatalysts: a review, Royal Society of Chemistry Advances. 5 (2015) 14610–14630. doi:10.1039/C4RA13734E.

[24] H. Kisch, Semiconductor photocatalysis - Mechanistic and synthetic aspects, Angewandte Chemie - International Edition. 52 (2013) 812–847. doi:10.1002/anie.201201200.

[25] H. Park, H. Kim, G. Moon, W. Choi, Photoinduced charge transfer processes in solar photocatalysis based on modified TiO $_2$, Energy Environ. Sci. 9 (2016) 411–433. doi:10.1039/C5EE02575C.

[26] C.S. Turchi, D.F. Ollis, Photocatalytic Degradation of Organic-Water Contaminants - Mechanisms Involving Hydroxyl Radical Attack., Journal of Catalysis. 122 (1990) 178.

[27] T. Hirakawa, Y. Nosaka, Properties of O2.- and OH. Formed in TiO2 aqueous suspensions by the photocatalytic reaction and the influence of H2O2 and some ions, Langmuir. 18 (2002) 3247–3254. doi:10.1021/la015685a.

[28] G. Zhang, X. He, M.N. Nadagouda, K. E. O'Shea, D.D. Dionysiou, The effect of basic pH and carbonate ion on the mechanism of photocatalytic destruction of cylindrospermopsin, Water Research. 73 (2015) 353–361. doi:10.1016/j.watres.2015.01.011.

[29] N. Merayo, D. Hermosilla, B. Jefferson, Á. Blanco, Influence of Alkalinity on the Efficiency and Catalyst Behavior of Photo-Assisted Processes, Chemical Engineering and Technology. 39 (2016) 158–165. doi:10.1002/ceat.201400320.

[30] X. Van Doorslaer, J. Dewulf, J. De Maerschalk, H. Van Langenhove, K. Demeestere, Heterogeneous photocatalysis of moxifloxacin in hospital effluent: Effect of selected matrix constituents, Chemical Engineering Journal. 261 (2015) 9–16. doi:10.1016/j.cej.2014.06.079.

[31] S. Dong, J. Feng, M. Fan, Y. Pi, L. Hu, X. Han, M. Liu, J. Sun, J. Sun, Recent developments in heterogeneous photocatalytic water treatment using visible light-responsive photocatalysts: A review, RSC Advances. 5 (2015) 14610–14630. doi:10.1039/c4ra13734e.

[32] P. Wang, J. Wang, T. Ming, X. Wang, H. Yu, J. Yu, Y. Wang, M. Lei, Dye-Sensitization-Induced Visible-Light Reduction of Graphene Oxide for the Enhanced TiO 2 Photocatalytic Performance, ACS Applied Materials & Interfaces. 5 (2013) 2924–2929. doi:10.1021/am4008566.

[33] K. Natarajan, H.C. Bajaj, R.J. Tayade, Photocatalytic efficiency of bismuth oxyhalide (Br, Cl and I) nanoplates for RhB dye degradation under LED irradiation, Journal of Industrial and Engineering Chemistry. 34 (2016) 146–156. doi:10.1016/j.jiec.2015.11.003.

[34] S. Cao, J. Low, J. Yu, M. Jaroniec, Polymeric Photocatalysts Based on Graphitic Carbon Nitride, Advanced Materials. 27 (2015) 2150–2176. doi:10.1002/adma.201500033.

[35] X. Wang, K. Maeda, A. Thomas, K. Takanabe, G. Xin, J.M. Carlsson, K. Domen, M. Antonietti, A metal-free polymeric photocatalyst for hydrogen production from water under visible light, Nature Materials. 8 (2009) 76–80. doi:10.1038/nmat2317.

[36] S. Ghosh, N.A. Kouamé, L. Ramos, S. Remita, A. Dazzi, A. Deniset-Besseau, P. Beaunier, F. Goubard, P.-H. Aubert, H. Remita, Conducting polymer nanostructures for photocatalysis under visible light, Nature Materials. 14 (2015) 505–511. doi:10.1038/nmat4220.

[37] V.M. Ovando-Medina, R.G. López, B.E. Castillo-Reyes, P.A. Alonso-Dávila, H. Martínez-Gutiérrez, O. González-Ortega, L. Far??as-Cepeda, Composite of acicular rod-like ZnO nanoparticles and semiconducting polypyrrole photoactive under visible light irradiation for methylene blue dye photodegradation, Colloid and Polymer Science. 293 (2015) 3459–3469. doi:10.1007/s00396-015-3717-2.

[38] I. Nath, J. Chakraborty, P.M. Heynderickx, F. Verpoort, Engineered Synthesis of Hierarchical Porous Organic Polymers for Visible Light and Natural Sunlight Induced Rapid Degradation of Azo, Thiazine, and Fluorescein Based Dyes in a Unique Mechanistic Pathway, Applied Catalysis B: Environmental. 227 (2018) 102–113. doi:10.1016/j.apcatb.2018.01.032.

[39] X. Wang, K. Maeda, A. Thomas, K. Takanabe, G. Xin, J.M. Carlsson, K. Domen, M. Antonietti, A metal-free polymeric photocatalyst for hydrogen production from water under visible light, Nature Materials. 8 (2008) 76–80. doi:10.1038/nmat2317.

[40] W.Y. Teoh, J.A. Scott, R. Amal, Progress in heterogeneous photocatalysis: From classical radical chemistry to engineering nanomaterials and solar reactors, Journal of Physical Chemistry Letters. 3 (2012) 629–639. doi:10.1021/jz3000646.

[41] D. Spasiano, R. Marotta, S. Malato, P. Fernandez-Ibañez, I. Di Somma, Solar photocatalysis: Materials, reactors, some commercial, and pre-industrialized applications. A comprehensive approach, Applied Catalysis B: Environmental. 170–171 (2015) 90–123. doi:https://doi.org/10.1016/j.apcatb.2014.12.050.

[42] O. Tokode, R. Prabhu, L.A. Lawton, P.K.J. Robertson, UV LED Source for Heterogeneous Photocatalysis, in: D.W. Bahnemann, P.K.J. Robertson (Eds.), Environmental Photochemistry Part III, 1st ed., Springer Berlin Heidelberg, Berlin, Heidelberg, 2015: pp. 159–179. doi:10.1007/978-3-662-46795-4.

[43] R. Thiruvenkatachari, S. Vigneswaran, I.S. Moon, JOURNAL REVIEW A review on UV / TiO 2 photocatalytic oxidation process, 25 (2008) 64–65.

[44] J. Marugán, R. van Grieken, A.E. Cassano, O.M. Alfano, CHAPTER 15 Photocatalytic Reactor Design, in: Photocatalysis: Fundamentals and Perspectives, The Royal Society of Chemistry, 2016: pp. 367–387. doi:10.1039/9781782622338-00367.

[45] M.E. Borges, M. Sierra, P. Esparza, Solar photocatalysis at semi-pilot scale: wastewater decontamination in a packed-bed photocatalytic reactor system with a visible-solar-light-driven photocatalyst, Clean Technologies, and Environmental Policy. 19 (2017) 1239–1245. doi:10.1007/s10098-016-1312-y.

[46] P.J. Valadés-Pelayo, C.A. Arancibia-Bulnes, I. Salgado-Tránsito, H.I. Villafán-Vidales, M.I. Peña-Cruz, A.E. Jiménez-González, Effect of

photocatalyst film geometry on radiation absorption in a solar reactor, a multiscale approach, Chemical Engineering Science. 161 (2017) 24–35. doi:10.1016/j.ces.2016.11.046.

[47] G. Vella, G.E. Imoberdorf, A. Sclafani, A.E. Cassano, O.M. Alfano, L. Rizzuti, Modeling of a TiO2-coated quartz wool packed bed photocatalytic reactor, Applied Catalysis B: Environmental. 96 (2010) 399–407. doi:10.1016/j.apcatb.2010.02.037.

[48] G.E. Imoberdorf, F. Taghipour, M. Keshmiri, M. Mohseni, Predictive radiation field modeling for fluidized bed photocatalytic reactors, Chemical Engineering Science. 63 (2008) 4228–4238. doi:10.1016/j.ces.2008.05.022.

[49] A. Torkkeli, Droplet microfluidics on a planar surface, VTT Publications. 53 (2003) 3–194. doi:10.1002/aic.

[50] O.M. Alfano, M.I. Cabrera, A.E. Cassano, Photocatalytic Reactions Involving Hydroxyl Radical Attack, Journal of Catalysis. 172 (1997) 370–379. doi:10.1006/jcat.1997.1858.

[51] C.S. Zalazar, C.A. Martin, A.E. Cassano, Photocatalytic intrinsic reaction kinetics. II: Effects of oxygen concentration on the kinetics of the photocatalytic degradation of dichloroacetic acid, Chemical Engineering Science. 60 (2005) 4311–4322. doi:10.1016/j.ces.2004.10.050.

[52] M.M. De Los Ballari, O.O. Alfano, A.E. Cassano, Photocatalytic degradation of dichloroacetic acid. A kinetic study with a mechanistically based reaction model, Industrial, and Engineering Chemistry Research. 48 (2009) 1847–1858. doi:10.1021/ie801194f.

[53] M.A. Mueses, F. Machuca-Martinez, A. Hernández-Ramirez, G. Li Puma, Effective radiation field model to scattering – Absorption applied in heterogeneous photocatalytic reactors, Chemical Engineering Journal. 279 (2015) 442–451. doi:10.1016/j.cej.2015.05.056.

[54] R. Acosta-Herazo, J. Monterroza-Romero, M.Á. Mueses, F. Machuca-Martínez, G. Li Puma, Coupling the Six Flux Absorption-Scattering Model to the Henyey-Greenstein scattering phase function: Evaluation and optimization of radiation absorption in solar heterogeneous photoreactors,

Chemical Engineering Journal. 302 (2016) 86–96. doi:10.1016/j.cej.2016.04.127.

[55] M.A. Mueses, F. Machuca-Martinez, G. Li Puma, Effective quantum yield and reaction rate model for evaluation of photocatalytic degradation of water contaminants in heterogeneous pilot-scale solar photoreactors, Chemical Engineering Journal. 215–216 (2013) 937–947. doi:10.1016/j.cej.2012.11.076.

[56] J. Colina-Márquez, F. Machuca-Martínez, G. Li Puma, Modeling the Photocatalytic Mineralization in Water of Commercial Formulation of Estrogens 17- β Estradiol (E2) and Nomegestrol Acetate in Contraceptive Pills in a Solar Powered Compound Parabolic Collector, Molecules. (2015) 13354–13373. doi:10.3390/molecules200713354.

[57] I. Grčić, G. Li Puma, Six-flux absorption-scattering models for photocatalysis under wide-spectrum irradiation sources in annular and flat reactors using catalysts with different optical properties, Applied Catalysis B: Environmental. 211 (2017) 222–234. doi:10.1016/j.apcatb.2017.04.014.

[58] M. de los M. Ballari, R. Brandi, O. Alfano, A. Cassano, Mass transfer limitations in photocatalytic reactors employing titanium dioxide suspensions. II. External and internal particle constraints for the reaction, Chemical Engineering Journal. 136 (2008) 242–255. doi:10.1016/j.cej.2007.03.031.

[59] A. Brucato, A.E. Cassano, F. Grisafi, G. Montante, L. Rizzuti, G. Vella, Estimating radiant fields in flat heterogeneous photoreactors by the six-flux model, AIChE Journal. 52 (n.d.) 3882–3890. doi:10.1002/aic.10984.

[60] H.L. Otálvaro-Marín, M.A. Mueses, F. Machuca-Martínez, Boundary layer of photon absorption applied to heterogeneous photocatalytic solar flat plate reactor design, International Journal of Photoenergy. 2014 (2014). doi:10.1155/2014/930439.

[61] M.A. Mueses, F. Machuca-Martinez, G. Li Puma, Effective quantum yield and reaction rate model for evaluation of photocatalytic degradation of water contaminants in heterogeneous pilot-scale solar photoreactors, Chemical

Engineering Journal. 215–216 (2013) 937–947. doi:10.1016/j.cej.2012.11.076.

[62] J. Xu, J. Yang, N. Zhao, L. Sheng, Y. Zhao, Z. Tang, Evaluation of the efficiency of aircraft liquid waste treatment and identification of daily inspection indices: a case study in Changchun, China, Environmental Monitoring and Assessment. 185 (2013) 6063–6070. doi:10.1007/s10661-012-3006-1.

[63] Z. Liu, M. Qun, W. An, Z. Sun, An application of membrane bio-reactor process for the wastewater treatment of Qingdao International Airport, Desalination. 202 (2007) 144–149. doi:10.1016/j.desal.2005.12.050.

[64] I. Moreno-Andrade, G. Moreno, G. Kumar, G. Buitron, Biodegradation of toilet wastewaters generated in aircraft, Journal of the Chinese Chemical Society. 61 (2014) 814–818. doi:10.1002/jccs.201300648.

[65] C.S. Lima, K.A. Batista, A. Garcia Rodriguez, J.R. Souza, K.F. Fernandes, Photodecomposition and color removal of a real sample of textile wastewater using heterogeneous photocatalysis with polypyrrole, Solar Energy. 114 (2015) 105–113. doi:10.1016/j.solener.2015.01.038.

[66] K.M. Lee, C.W. Lai, K.S. Ngai, J.C. Juan, Recent Developments of Zinc Oxide Based Photocatalyst in Water Treatment Technology: A Review, Water Research. 88 (2015) 428–448. doi:10.1016/j.watres.2015.09.045.

[67] X. Zhang, T. Peng, S. Song, Recent advances in dye-sensitized semiconductor systems for photocatalytic hydrogen production, J. Mater. Chem. A. 4 (2016) 2365–2402. doi:10.1039/C5TA08939E.

[68] N. Lu, Y.P. Yeh, G.B. Wang, T.Y. Feng, Y. hsin Shih, D. Chen, Dye-sensitized TiO2-catalyzed photodegradation of sulfamethoxazole under the blue or yellow light, Environmental Science and Pollution Research. 24 (2017) 489–499. doi:10.1007/s11356-016-7815-6.

[69] C. Díaz-Uribe, W. Vallejo, K. Campos, W. Solano, J. Andrade, A. Muñoz-Acevedo, E. Schott, X. Zarate, Improvement of the photocatalytic activity of TiO2using Colombian Caribbean species (Syzygium cumini) as natural sensitizers: Experimental and theoretical studies, Dyes and Pigments. 150

(2018) 370–376. doi:10.1016/j.dyepig.2017.12.027.

[70] S. Benjamin, D. Vaya, P.B. Punjabi, S.C. Ameta, Enhancing photocatalytic activity of zinc oxide by coating with some natural pigments, Arabian Journal of Chemistry. 4 (2011) 205–209. doi:10.1016/j.arabjc.2010.06.038.

[71] M. Joshi, S.P. Kamble, N.K. Labhsetwar, D. V. Parwate, S.S. Rayalu, Chlorophyll-based photocatalysts and their evaluations for methyl orange photoreduction, Journal of Photochemistry and Photobiology A: Chemistry. 204 (2009) 83–89. doi:10.1016/j.jphotochem.2009.01.016.

[72] T. Phongamwong, W. Donphai, P. Prasitchoke, C. Rameshan, N. Barrabés, W. Klysubun, G. Rupprechter, M. Chareonpanich, Novel visible-light-sensitized Chl-Mg/P25 catalysts for photocatalytic degradation of rhodamine B, Applied Catalysis B: Environmental. 207 (2017) 326–334. doi:10.1016/j.apcatb.2017.02.042.

[73] Z. Zhao, Y. Sun, F. Dong, Graphitic carbon nitride based nanocomposites: A review, Nanoscale. 7 (2015) 15–37. doi:10.1039/c4nr03008g.

[74] G. Zhang, W. Choi, A low-cost sensitizer based on a phenolic resin for charge-transfer type photocatalysts working under visible light, Chemical Communications. 48 (2012) 10621. doi:10.1039/c2cc35751h.

[75] Y. Jiang, L. Meng, X. Mu, X. Li, H. Wang, X. Chen, X. Wang, W. Wang, F. Wu, X. Wang, Effective TiO2 hybrid heterostructure fabricated on nano mesoporous phenolic resol for visible-light photocatalysis, Journal of Materials Chemistry. 22 (2012) 23642. doi:10.1039/c2jm35042d.

[76] G. Zhang, C.S. Ni, L.J. Liu, G.X. Zhao, F. Fina, J.T.S. Irvine, Macro-mesoporous resorcinol-formaldehyde polymer resins as amorphous metal-free visible light photocatalysts, Journal of Materials Chemistry A. 3 (2015) 15413–15419. doi:10.1039/c5ta03628c.

[77] G. Zhang, C. Kim, W. Choi, Poly(4-vinylphenol) as a new stable and metal-free sensitizer of titania for visible light photocatalysis through ligand-to-metal charge transfer process, Catalysis Today. 281 (2017) 109–116. doi:10.1016/j.cattod.2016.06.048.

[78] J.J. Salazar-Rábago, M. Sánchez-Polo, J. Rivera-Utrilla, R. Leyva-Ramos,

R. Ocampo-Pérez, F. Carrasco-Marin, Organic xerogels doped with Tris(2,2′-bipyridine) ruthenium(II) as hydroxyl radical promoters: Synthesis, characterization, and photoactivity, Chemical Engineering Journal. 306 (2016) 289–297. doi:10.1016/j.cej.2016.07.053.

[79] P. Chowdhury, S. Athapaththu, A. Elkamel, A.K. Ray, Visible-solar-light-driven photo-reduction and removal of cadmium ion with Eosin Y-sensitized TiO2in aqueous solution of triethanolamine, Separation and Purification Technology. 174 (2017) 109–115. doi:10.1016/j.seppur.2016.10.011.

[80] J. Lv, Q. Hu, C. Cao, Y. Zhao, Modulation of valence band maximum edge and photocatalytic activity of BiOX by incorporation of halides, Chemosphere. 191 (2018) 427–437. doi:10.1016/j.chemosphere.2017.09.149.

[81] M.N. Rashed, Photocatalytic degradation of methyl orange in aqueous TiO 2 under different solar irradiation sources, International Journal. 2 (2007) 073–081.

[82] L.C. Ferreira, M.S. Lucas, J.R. Fernandes, P.B. Tavares, Photocatalytic oxidation of Reactive Black 5 with UV-A LEDs, Journal of Environmental Chemical Engineering. 4 (2016) 109–114. doi:10.1016/j.jece.2015.10.042.

[83] C.S. Zalazar, R.L. Romero, C.A. Martín, A.E. Cassano, Photocatalytic intrinsic reaction kinetics I: Mineralization of dichloroacetic acid, Chemical Engineering Science. 60 (2005) 5240–5254. doi:10.1016/j.ces.2005.04.050.

[84] B. Liu, X. Zhao, C. Terashima, A. Fujishima, K. Nakata, Thermodynamic and kinetic analysis of heterogeneous photocatalysis for semiconductor systems, Physical Chemistry Chemical Physics. 16 (2014) 8751. doi:10.1039/c3cp55317e.

[85] D. Monllor-Satoca, R. Gómez, M. González-Hidalgo, P. Salvador, The “Direct–Indirect” model: An alternative kinetic approach in heterogeneous photocatalysis based on the degree of interaction of dissolved pollutant species with the semiconductor surface, Catalysis Today. 129 (2007) 247–255. doi:10.1016/j.cattod.2007.08.002.

[86] I. Grčić, G. Li Puma, Photocatalytic degradation of water contaminants in

multiple photoreactors and evaluation of reaction kinetic constants independent of photon absorption, irradiance, reactor geometry, and hydrodynamics, Environmental Science and Technology. 47 (2013) 13702–13711. doi:10.1021/es403472e.

[87] S. Khan, X. He, J.A. Khan, H.M. Khan, D.L. Boccelli, D.D. Dionysiou, Kinetics and mechanism of sulfate radical- and hydroxyl radical-induced degradation of highly chlorinated pesticide lindane in UV/peroxymonosulfate system, Chemical Engineering Journal. 318 (2017) 135–142. doi:10.1016/j.cej.2016.05.150.

[88] Y. Liu, X. He, X. Duan, Y. Fu, D. Fatta-Kassinos, D.D. Dionysiou, Significant role of UV and carbonate radical on the degradation of oxytetracycline in UV-AOPs: Kinetics and mechanism, Water Research. 95 (2016) 195–204. doi:10.1016/j.watres.2016.03.011.

[89] C.S. Turchi, D.F. Ollis, Photocatalytic degradation of organic water contaminants: Mechanisms involving hydroxyl radical attack, Journal of Catalysis. 122 (1990) 178–192. doi:10.1016/0021-9517(90)90269-P.

[90] R. Saraswat, N. Talreja, D. Deva, N. Sankararamakrishnan, A. Sharma, N. Verma, Development of novel in situ nickel-doped, phenolic resin-based micro-nano-activated carbon adsorbents for the removal of vitamin B-12, Chemical Engineering Journal. 197 (2012) 250–260. doi:10.1016/j.cej.2012.05.046.

[91] J.B. Yang, L.C. Ling, L. Liu, F.Y. Kang, Z.H. Huang, H. Wu, Preparation and properties of phenolic resin-based activated carbon spheres with controlled pore size distribution, Carbon. 40 (2002) 911–916. doi:10.1016/S0008-6223(01)00222-6.

[92] M. Zhao, H. Song, Catalytic Graphitization of Phenolic Resin, Journal of Materials Science and Technology. 27 (2011) 266–270. doi:10.1016/S1005-0302(11)60060-1.

[93] M.I. Cabrera, O.M. Alfano, A.E. Cassano, Absorption and Scattering Coefficients of Titanium Dioxide Particulate Suspensions in Water, Journal of Physical Chemistry. 100 (1996) 20043–20050. doi:10.1021/jp962095q.

[94] A.P.H. Association, A.W.W. Association, Standard methods for the examination of water and wastewater: selected analytical methods approved and cited by the United States Environmental Protection Agency, American Public Health Association, 1981.

[95] Y. Wang, P. Zhang, Photocatalytic decomposition of perfluorooctanoic acid (PFOA) by TiO 2 in the presence of oxalic acid, Journal of Hazardous Materials. 192 (2011) 1869–1875. doi:10.1016/j.jhazmat.2011.07.026.

[96] L.H. Long, B. Halliwell, Artefacts in cell culture: Pyruvate as a scavenger of hydrogen peroxide generated by ascorbate or epigallocatechin gallate in cell culture media, Biochemical and Biophysical Research Communications. 388 (2009) 700–704. doi:10.1016/j.bbrc.2009.08.069.

[97] M.-Q. Yang, Y. Zhang, N. Zhang, Z.-R. Tang, Y.-J. Xu, Visible-Light-Driven Oxidation of Primary C–H Bonds over CdS with Dual Co-catalysts Graphene and TiO2, Scientific Reports. 3 (2013) 3314. doi:10.1038/srep03314.

[98] M. Krivec, R. Dillert, D.W. Bahnemann, a Mehle, J. Štrancar, G. Dražić, J. Strancar, G. Dražić, The nature of chlorine-inhibition of photocatalytic degradation of dichloroacetic acid in a TiO2-based microreactor., Physical Chemistry Chemical Physics : PCCP. 16 (2014) 14867–73. doi:10.1039/c4cp01043d.

[99] Ö. Yildiz, A.M. Soydan, E.F. Ipçizade, D. Akin, Ö. Uçak, Properties of ZnO nanopowders synthesized by glycine-nitrate gel combustion, Acta Physica Polonica A. 125 (2014) 664–666. doi:10.12693/APhysPolA.125.664.

[100] R.A. Spurr, E.H. Erath, H. Myers, Curing Process in Phenolic Resins X-Ray Diffraction Analysis, Industrial & Engineering Chemistry. 49 (1957) 1838–1839. doi:10.1021/ie50575a026.

[101] Z. Guo, Z. Liu, L. Ye, K. Ge, T. Zhao, The production of lignin-phenol-formaldehyde resin derived carbon fibers stabilized by BN preceramic polymer, Materials Letters. 142 (2015) 49–51. doi:10.1016/j.matlet.2014.11.068.

[102] Y. Jiang, L. Meng, X. Mu, X. Li, H. Wang, X. Chen, X. Wang, W. Wang, F. Wu, X. Wang, Effective TiO2 hybrid heterostructure fabricated on nano

mesoporous phenolic resol for visible-light photocatalysis, Journal of Materials Chemistry. 22 (2012) 23642. doi:10.1039/c2jm35042d.

[103] H. Chang, M. Kao, T. Chen, C. Chen, K. Cho, X. Lai, Characterization of Natural Dye Extracted from Wormwood and Purple Cabbage for Dye-Sensitized Solar Cells, 2013 (2013).

[104] G. Knör, Recent progress in homogeneous multielectron transfer photocatalysis and artificial photosynthetic solar energy conversion, Coordination Chemistry Reviews. 304–305 (2015) 102–108. doi:10.1016/j.ccr.2014.09.013.

[105] A. Mills, J. Wang, Photobleaching of methylene blue sensitised by TiO2: An ambiguous system?, Journal of Photochemistry and Photobiology A: Chemistry. 127 (1999) 123–134. doi:10.1016/S1010-6030(99)00143-4.

[106] D. Monllor-Satoca, R. G??mez, M. Gonz??lez-Hidalgo, P. Salvador, The “Direct-Indirect” model: An alternative kinetic approach in heterogeneous photocatalysis based on the degree of interaction of dissolved pollutant species with the semiconductor surface, Catalysis Today. 129 (2007) 247–255. doi:10.1016/j.cattod.2007.08.002.

[107] J.T. Guo, D.C. Yang, Z. Guan, Y.H. He, Chlorophyll-Catalyzed Visible-Light-Mediated Synthesis of Tetrahydroquinolines from N,N-Dimethylanilines and Maleimides, Journal of Organic Chemistry. 82 (2017) 1888–1894. doi:10.1021/acs.joc.6b03034.

[108] D. Zhang, R. Qiu, L. Song, B. Eric, Y. Mo, X. Huang, Role of oxygen active species in the photocatalytic degradation of phenol using polymer sensitized TiO2 under visible light irradiation, Journal of Hazardous Materials. 163 (2009) 843–847. doi:10.1016/j.jhazmat.2008.07.036.

[109] T. Ogoshi, K. Umeda, T. Yamagishi, Y. Nakamoto, Synthesis of Phenolic Polymer-Coated Gold Nanoparticles, Polymer Journal. 40 (2008) 942–943. doi:10.1295/polymj.PJ2008069.

# Supplementary material

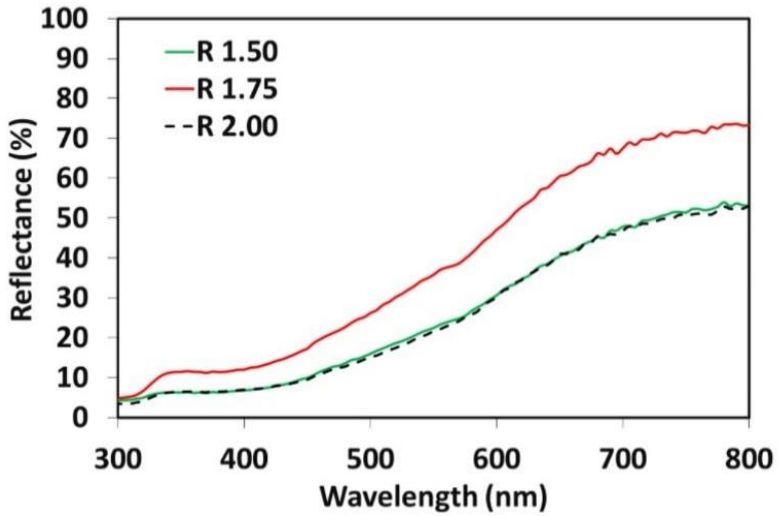


Figure S1. Reflectance spectra of synthesized phenolic resins.